6-15-2024

Spin and Charge Transport in Metallic Ferrimagnets and Disordered Magnetic Oxides

Leopoldo A. Hernandez

Spin and Charge Transport in Metallic Ferrimagnets and Disordered Magnetic Oxides

Abstract

Recent efforts have been exploring the use of thin film synthetic ferrimagnets and disordered magnetic oxides for applications in spintronic devices. Due to the antiferromagnetic exchange interaction, ferrimagnetic materials offer the ultrafast dynamics of the antiferromagnetic exchange, with a net magnetization that can be influenced externally. With two, or more, competing ferromagnet sublattices, interesting properties arise that depend on the final magnetic landscape after growth of the material and it's inherent magnetic anisotropy energies. Properties such as magnetic compensation temperatures, and perpendicular magnetic anisotropy are attractive for applications in spintronic memory and logic devices, some already being implemented in MRAM devices. Observation of increased spin diffusion and spin dephasing lengths at magnetic compensation temperatures has sparked a surge in ferrimagnet spintronics, with novel methods to influence magnetization being realized. With many parameters involved affecting the magnetic landscape it's imperative that more fundamental knowledge be obtained for ferrimagnetic and antiferromagnetic materials so that useful devices can be achieved. Understanding the magnetic and electrical properties as a function of temperature, and probing for spin transport can help build the essential phase map for these materials and determine how to tune certain properties.

In this dissertation, I begin with a description of the materials being investigated, and what methods are being used to interpret the preceding magnetic and electrical properties. Starting with nonlocal resistance measurements to probe spin transport in amorphous Yttrium Iron Oxide, measurements of nonlocal resistances in amorphous Yttrium Iron Oxide, a disordered antiferromagnetic insulator, are discussed. Inverse spin hall effect (ISHE) measurements in nonlocal geometry show that no spin transport is observed in amorphous Y-Fe-O using this method. In fact, experiments reveal that the material acts as a disordered antiferromagnetic semiconductor since the resistivity follows what you'd expect from Mott's variable range hopping, leading to a more difficult realization of spin transport across this material. Magnetometry measurements of the amorphous Y-Fe-O also confirm the antiferromagnetism of the material, leading to the conclusion that different methods to probe spin transport in this material are necessary. Next, I focus on the transition metal (TM) rare earth (RE) metallic ferrimagnets with perpendicular magnetic anisotropy. A temperature controlled anomalous Hall effect (AHE) memory device is demonstrated with such a material, utilizing the unique properties around the synthetic ferrimagnet's magnetic compensation temperature, with details and explanations on the mechanisms that govern it. A closer investigation into the magnetic properties of the TM-RE ferrimagnet Co/Gd then follows, with observations of frustrated interactions at low temperatures. The magnetic anisotropy energies of a couple Co/Gd bilayer samples are quantified, concluding that there is a shift in the bulk perpendicular magnetic anisotropy at low temperatures, confirmed through electrical and magnetic measurements. Finally, a non-local spin valve (NLSV) device is used to measure a pure spin current in Fe/Al, paving the way for implementing ferrimagnetic materials such as TM-RE Co/Gd in these lateral spin valves. Details of fabrication and measurement methods are discussed, with fabrication hurdles overcome to realize a working device that can be fabricated using a two step deposition method.

Document Type

Dissertation

Degree Name

Ph.D.

First Advisor
Barry L. Zink

Second Advisor
Xin Fan

Third Advisor
Pavel Salev

Keywords
Antiferromagnet, Charge, Ferrimagnet, Magnetism, Spin, Spintronics

Subject Categories
Condensed Matter Physics | Materials Science and Engineering | Other Materials Science and Engineering | Physical Sciences and Mathematics | Physics

SPIN AND CHARGE TRANSPORT IN METALLIC FERRIMAGNETS AND DISORDERED MAGNETIC OXIDES

A Dissertation

Presented to

the Faculty of the College of Natural Science and Mathematics

University of Denver

In Partial Fulfillment

of the Requirements for the Degree

Doctor of Philosophy

---

by

Leopoldo A. Hernandez

June 2024

Advisor: Barry L. Zink

Author: Leopoldo A. Hernandez
Title: Spin and Charge Transport in Metallic Ferrimagnets and Disordered Magnetic Oxides
Advisor: Barry L. Zink
Degree Date: June 2024

ABSTRACT

Recent efforts have been exploring the use of thin film synthetic ferrimagnets and disordered magnetic oxides for applications in spintronic devices. Due to the antiferromagnetic exchange interaction, ferrimagnetic materials offer the ultrafast dynamics of the antiferromagnetic exchange, with a net magnetization that can be influenced externally. With two, or more, competing ferromagnet sublattices, interesting properties arise that depend on the final magnetic landscape after growth of the material and it's inherent magnetic anisotropy energies. Properties such as magnetic compensation temperatures, and perpendicular magnetic anisotropy are attractive for applications in spintronic memory and logic devices, some already being implemented in MRAM devices. Observation of increased spin diffusion and spin dephasing lengths at magnetic compensation temperatures has sparked a surge in ferrimagnet spintronics, with novel methods to influence magnetization being realized. With many parameters involved affecting the magnetic landscape it's imperative that more fundamental knowledge be obtained for ferrimagnetic and antiferromagnetic materials so that useful devices can be achieved. Understanding the magnetic and electrical properties as a function of temperature, and probing for spin transport can help build the essential phase map for these materials and determine how to tune certain properties

In this dissertation, I begin with a description of the materials being investigated, and what methods are being used to interpret the preceding magnetic and electrical properties. Starting with nonlocal resistance measurements to probe spin

transport in amorphous Yttrium Iron Oxide, measurements of nonlocal resistances in amorphous Yttrium Iron Oxide, a disordered antiferromagnetic insulator, are discussed. Inverse spin hall effect (ISHE) measurements in nonlocal geometry show that no spin transport is observed in amorphous Y-Fe-O using this method. In fact, experiments reveal that the material acts as a disordered antiferromagnetic semiconductor since the resistivity follows what you'd expect from Mott's variable range hopping, leading to a more difficult realization of spin transport across this material. Magnetometry measurements of the amorphous Y-Fe-O also confirm the antiferromagnetism of the material, leading to the conclusion that different methods to probe spin transport in this material are necessary. Next, I focus on the transition metal (TM) rare earth (RE) metallic ferrimagnets with perpendicular magnetic anisotropy. A temperature controlled anomalous Hall effect (AHE) memory device is demonstrated with such a material, utilizing the unique properties around the synthetic ferrimagnet's magnetic compensation temperature, with details and explanations on the mechanisms that govern it. A closer investigation into the magnetic properties of the TM-RE ferrimagnet Co/Gd then follows, with observations of frustrated interactions at low temperatures. The magnetic anisotropy energies of a couple Co/Gd bilayer samples are quantified, concluding that there is a shift in the bulk perpendicular magnetic anisotropy at low temperatures, confirmed through electrical and magnetic measurements. Finally, a non-local spin valve (NLSV) device is used to measure a pure spin current in Fe/Al, paving the way for implementing ferrimagnetic materials such as TM-RE Co/Gd in these lateral spin valves. Details of fabrication and measurement methods are discussed, with fabrication hurdles overcome to realize a working device that can be fabricated using a two step deposition method.

ACKNOWLEDGEMENTS

In no particular order, I'd like to to acknowledge everyone who has made obtaining this PhD possible. Thank you Dr. Tak Gurung for spending extra time with me to teach me more than what my intro to physics classes required, and suggesting I pursue grad school. Thank you to all of my undergraduate mentors at The University of Texas at San Antonio for the guidance and knowledge you provided. I am grateful for the opportunity to work in Dr. Kathryn Mayer's biophysics lab, as well as Dr. Carlos Monton's lab where Jason Giuliani helped me discover the research path I wanted to pursue. Thank you to the Ronald E. McNair Scholar program at UTSA, especially Sonia Valencia and Darrell Balderrama for the graduate school prep and continued support. To all the professors at DU that guided me through the graduate school process: Jennifer Hoffman, Mark Siemens, Sofia Cisneros, Dinah Loerke, Kingshuk Ghosh, Pavel Salev, and many more. To my peers, Sam Bleser, Matt Natale, Eric Morris, Ian Ellis, Nick Boyd, Kyle Peterson and Mike Roos. Thank you for the support in the lab, and for being great friends. Thank you to Ryan Greening and Xin Fan for fabrication of the ferrimagnet samples, and lessons of the Xin Fan Lab equipment. To the past members of the Zink lab, Rachel Bennet and Alex Hojem, thank you, your notes greatly helped with sample fabrication and experiment setup. To my advisor, Barry Zink, I am extremely thankful for all your mentorship and patience. Even though we had a lot of hurdles with the asbestos cleaning and the pandemic, I have had the greatest learning experience thanks to you. Your knowledge and expertise that you have passed on to me has launched me into an exciting career, and I can't thank you enough for all of your understanding and support. Last but not least, I want to give thanks to my family and friends. Cris, I am indebted to you for all your sacrifice in pursuit of this degree. You have no idea how much everything you have done has meant to me. Your love and support through this process has kept me sane even in the hardest times.

TABLE OF CONTENTS

LIST OF FIGURES

CHAPTER 1:

INTRODUCTION

1.1. MOTIVATIONS

The investigation into novel materials for the field of spintronics has seen a boom in the last couple of decades [24, 87, 80, 37, 15]. Typically, in computational device architecture, the charge of the electron is responsible for the transfer of bits, or information, with the movement of the electron as the fundamental mechanism of information transfer. The charge of an electron is also the property that's utilized in semiconducting devices that create the transistors that are widely used in logic hardware. These devices have seen exponential growth in their speed, as well as density of their processes, since their creation[79]. As these devices shrink down to the atomic scale to meet the increasing demand for computational power, effects from the quantum realm begin to interfere with the processes. Effects such as electron tunneling create a fundamental limit on how small devices can get before they become inoperable and dramatically inefficient. Newer methods of architecture are being implemented using current CMOS logic and memory devices, by means of creative design into the $\vec{z}$ dimension of fabrication, or by fabricating the devices as small as physically possible with more efficient matierals. Besides electron tunneling interfering with device processes at the atomic scale, resistive heating is a major cause for concern with the increasing growth in the technologies that function on charge transport processes[48]. As electrons are moved from hardware component to hardware component, or through the logic devices themselves, the scattering events and friction they experience with the materials they are transported through cause Joule

heating. an effect that's dealt with through heat sinks and methods to cool computational hardware that themselves also require energy cost (fans and water circulation). In essence, a paradigm shift is underway to create more efficient memory and logic devices. Industry, as well as academic, research has pushed for a better developed understanding of the physics that limits the advancement of these particular devices. Inherently a multidisciplinary problem, there are many avenues being taken to solve the problems at hand. Spintronics is one subfield that is aimed at providing solutions.

Besides charge, an electron has an intrinsic property called spin, a quantization of an electron's angular momentum. An electron can have spin up, or spin down, and is already being implemented into a variety of computational devices that rely on the transport of the electron spin. Tunneling magnetoresistance and giant magnetoresistance are prime examples of magneto-transport effects that are implemented in read heads, random access memory, and magnetic sensors that have dramatically affected the magnetic storage device industry[25]. Spintronics, or spin electronics, uses the spin of electron to perform these processes. To achieve useful devices, one must create a spin accumulation, or spin current, and effectively transport it through materials. Typically, spin transfer torque (STT) and spin orbit torque (SOT) are two mechanisms in which this is realized. By passing a charge current through a FM material, the electrons can become spin polarized. When this spin polarized current is passed through another FM material, the angular momentum from the spins of the electrons is transferred to the magnetization of the FM by applying a torque. SOTs are a result of the spin orbit coupling (SOC) of a material, a property inherent to a material that can create a spin density in a region of space when electrons are flowed through that material. Depending on the mechanism chosen, these spin densities can be generated and detected depending on the geometry of the device. In the subsequent sections, the mechanisms that are used to study the spin and charge transport of antiferromagnetic (AFM) and FM materials are explained in more detail.

The chapters of this thesis present various measurements of charge and spin transport effects in materials that show promise of being applied efficiently in spintronics. With the various methods of generating spin densities and measuring them, this thesis will focus on using local and non-local electrical measurement techniques to detect spin and charge transport in various geometries, for various goals. Because spin is a fundamental property of an electron, unless serious care is taken in the device structure, measuring spin transport can be elusive and harder to interpret since charge signals are inevitable when spin densities are created through electrical means. The materials studied here will be outlined in more detail, but will focus on magnetic thin films and nanostructures. Amorphous Yttrium Iron Oxide showed indication of spin currents transported through magnons[77], like its structurally ordered counterpart Yttrium Iron Garnet, or YIG, but the measurements of this thesis tell a different story. YIG is known to be a ferrimagnet (FIM), in which the magnetic sublattices of the atoms are antiferromagnetically coupled, but there is still a net magnetization in the material, such as a FM. In its amorphous form, a-Y-Fe-O is measured to be a speromagnet, a material with AF magnetic coupling but no magnetic order, and is shown to exhibit semiconducting properties rather than insulating properties. This dramatically changes the landscape for the existence of spin transport, and is evaluated in detail using non-local measurement techniques.

Metallic magnetic materials are also investigated, with Chapter 3 outlining a novel memory device driven by temperature in the synthetic FIM Co-Gd and Chapter 5 outlining a pure spin current signal in Fe/Al nonlocal spin valve devices. By growing a bilayer thin film of Co-Gd (< 5 nm), a synthetic FIM can be achieved since the transition metal (TM) Co antiferromagnetically couples with rare earth (RE) Gd. This AF coupling can lead to ultrafast dynamics for spintronic devices, and other useful transport effects around it's compensation temperature, a temperature in which the magnetic sublattices are equal and opposite. Magnetometry and magnetotransport measurements of this FIM heterosctucture are further explored to present a funda-

mental understanding of the magnetic properties, and to provide the beginning of the framework for implementing FIM materials into non-local spin valve devices; a device useful for separating pure spin current from charge current. By establishing a spin transport signal in Fe/Al non-local spin valves, this device can become a control for future fabrications and measurements of non-local spin valves using FIM materials.

1.2. TRANSPORT AND EFFECTS

1.2.1. CHARGE AND SPIN TRANSPORT

As mentioned before, electrons exhibit fundamental properties such as charge, and spin. The charge of an electron is negative and its value is 1.60217663 x 10^{-19} C, while it can have two values for spin that we can refer to as spin up or spin down. For a material to contain charge transport, the negative electron charges in that material must be transported through it, known as a charge current I. This is usually driven by a voltage bias V, and, depending on the material, the electrons will experience what's known as resistance, R. These three values can be described by the relationship known as Ohm's Law which is $V = IR$. In order to create a charge current I, a voltage V must be applied with the type of material being transported through responsible for the resistance R. Similarly, a V can be obtained when a known I is passed through the material. Therefore, R is a measure of all the factors that influence the transport of the electrons. These factors include the geometry of the transport medium, but most importantly, the fundamental property known as resistivity, ρ (ρ is inversely related to the material's electrical conductivity σ). This relationship can be described by the equation $R = \rho L/A$ where L is the length and A the cross sectional area of the medium that the electrons are being transported through. In our case, the geometries used are typically nanowires with cross sectional areas as small as 2000 nm^2 and lengths as small as 500 nm. The spin of an electron can be transported in a similar fashion. Because there are two spin states an electron can occupy, the convention of spin up ($+\frac{1}{2}$) and spin down ($-\frac{1}{2}$) was established by

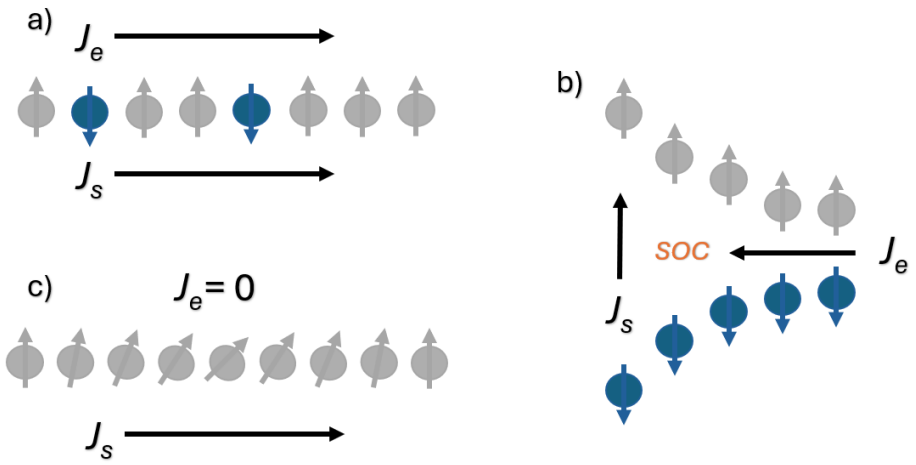

Figure 1.1: Examples of spin transport. **a)** A charge current with a majority of spin up or spin down electrons is known as a polarized charge current. Both charge J_e and spin J_s are transported. **b)** Example of SOC in a material giving rise to the SHE. As a charge current experiences the relativistic effects of SOC, a transverse, pure spin current J_s is generated. **c)** Typically in insulating materials where electrons are localized, spin transport can occur as the angular momentum of the electron is imparted on it's nearest neighbors and transmitted across some distance, otherwise referred to as a magnon.

the Stern-Gerlach experiment[63]. A spin of an electron can be conceptualized as a quanta of a magnetic moment, and when exposed to an external magnetic field, the spin up electrons will deflect oppositely to the spin down electrons, giving rise to two populations of spins separated in space. These spins can be transported in a few different ways to obtain a spin current. As what was established before, a charge current is when the electrons are physically transported across a medium. For this to become spin that's transported across the same medium, the charge current can be polarized as shown in Figure 1.1a.

When a charge current is polarized, its electrons have a majority of spin up, or spin down, giving rise to spin information being transmitted through the medium but at the same time that charge is transported. This is achieved by applying a charge current I through a FM material, so that the spin of the electrons aligns with the magnetization of the FM, polarizing the electrons. To obtain a pure spin

current, the spins of the electrons must be transported with a net charge transport of zero, Figure 1.1b-c. This is possible through the spin Hall effect (SHE), which will be explained in more detail later, and through magnons. Magnons are known as "spin waves", and occur when electrons remain stationary while spin information is transmitted through the transfer of spin angular momentum. While spin polarized currents are widely applied in spintronic devices, the inevitable Joule heating from the simultaneous charge transport can hinder the development of more efficient all spin, logic devices, making pure spin currents as the more attractive option.

1.2.2. SPIN HALL EFFECT (SHE) AND INVERSE SPIN HALL EFFECT (ISHE)

There can be various means of generating a spin current for transport that derive from electrical injection, optical injection, or even thermal injection. Generally, spin can be injected from a FM in the form of a polarized spin current when interfaced with a normal metal (NM). The spin will then diffuse into the NM which has it's own intrinsic diffusion length. When generated optically, known as spin pumping, spin can be injected through an interface when the ferromagnetic resonance (FMR) of a FM material is optically excited, driving magnons. One method used in this thesis is the spin Hall effect (SHE).

To introduce the SHE, we can remind ourselves of the Hall effect to construct the foundation of our understanding. In 1879 Edwin H. Hall observed that when a NM carrying a current is placed in an external magnetic field, the Lorentz force creates a transverse voltage that is normal to the current direction. Furthermore, when a FM material is used in place of a NM, Hall measured up to 10x in this transverse voltage referred to as the anomalous Hall effect (AHE), another transport effect utilized in this thesis and explained in more detail in a preceding section. The AHE, unlike the Hall effect, is understood to have it's roots in relativistic effects such as spin orbit coupling. The SHE is analogous to the AHE in this aspect, except the AHE correlates to the charge degrees of freedom while the SHE correlates to

the spin degree of freedom. When a current is passed through a NM, if there exists significant SOC, then a transverse pure spin current is generated that can act as an electrical generation of a pure spin current, Figure 1.1b. This effect is significant in heavy metals (HM) due to their intrinsically higher SOC. Through mechanisms of intrinsic deflection, side jump, and skew scattering [60, 51], the spin up and spin down electrons that comprise the charge current in a HM are transversely separated, leading to the spin current. This is useful for a fully electrical means of injecting a spin current into a spin transport medium, usually used in nonlocal devices such as the ones used in Chapter 2 to investigate the spin transport in amorphous Y-Fe-O. The magnitude of the transverse pure spin current density J_s can be described as a function of all the mechanisms' contributions to spin Hall conductivity, or more easily described by the current density J_e that is passed through the HM. This relationship can be described simply as $J_s = (\hbar/2e)\theta_{SH}J_e$, with θ_{SH} known as the spin Hall angle of the material, a constant describing the conversion efficiency[46].

With the SHE as a means of generating a pure spin current electrically, the inverse spin Hall effect is a method to measure pure spin current electrically. A direct inverse effect of the SHE, the ISHE is a conversion of a pure spin current into a charge current. This can be conceptualized when a pure spin current J_s is injected into a HM, and due to the same mechanisms as before, the J_s is converted into a measurable J_e and is described as $J_e = (2e/\hbar)\theta_{SH}J_s$, with θ_{SH} the same spin Hall angle as before[46]. This allows for the use of a HM, most commonly Pt, to act as a measuring device for pure spin transport when used in the correct geometries.

Depending on the spin transport medium, both the SHE and ISHE can be used to inject and detect spin currents across a medium when the right conditions are met. Because both of these methods are electrical, there are inherent charge transport signals associated with both effects if care is not taken to eliminate them. This means charge can "leak" across the transport medium if it is not insulating,

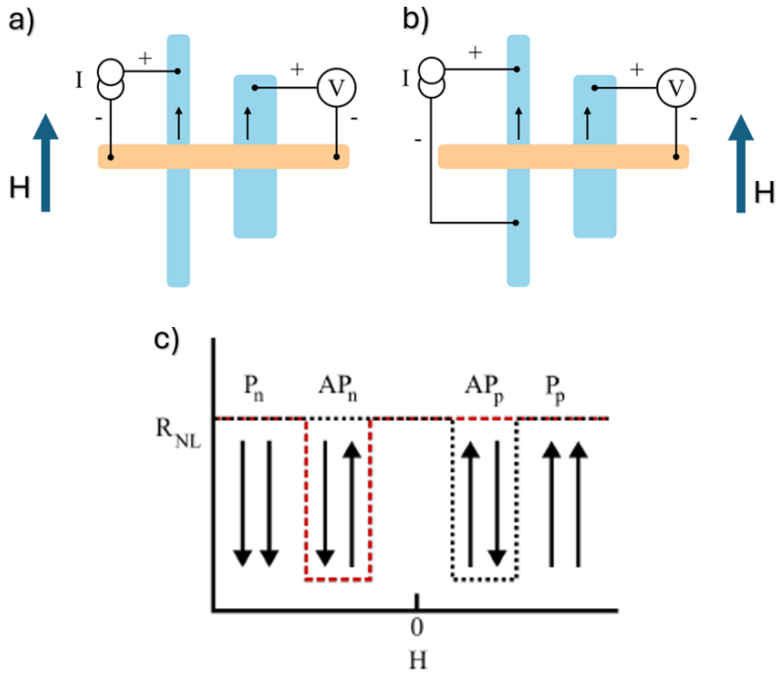

Figure 1.2: Cartoon depiction of NLSV schematic for measuring a nonlocal resistance R_{NL} **a)** shows the NLSV for the case of injecting a spin current electrically. A charge current passes through part of the NM channel but is shunted away, injecting spin through the NM channel electrically **b)** shows the NLSV for when injecting thermally. Current is never passed through NM channel, so that spin diffusion is injected thermally as the junction is heated, creating a thermal gradient in the NM channel and **c)** is an expected R_{NL} vs. H curve for a NLSV when the external field is swept along the axis of the FM wires magnetizations. The depiction of the 4 states for the NLSV measurement shows what happens to the spin signal when the FM wires have opposite magnetizations.

hindering the signal measured by the ISHE. Other artifacts that can effect this ISHE signal are explored in Chapter 2 when these spin generation and detection methods are used to detect spin transport across amorphous Y-Fe-O. These artifacts are a result of out-of-phase reactive components such as capacitance and inductance.

1.2.3. NONLOCAL SPIN VALVES

One method to separate charge current from spin current is through the use of nonlocal spin valves (NLSVs). As shown in Figure 1.2, a NLSV operates by using two ferromagnetic nanowire strips separated by a distance, but connected by a normal,

non-magnetic channel. Figure 1.2a-b show a NLSV schematic from a top view. By passing a current through one of the FM wires, called the FM_{inj}, a spin accumulation is generated at the FM_{inj}/NM interface. This spin accumulation then diffuses across the NM channel, with a characteristic diffusion length λ_{df} associated with the material used as the NM. Materials such as Cu and Al have relatively long diffusion lengths on the order of ~ 1 μm, making them ideal NM channels. Because the charge current is shunted away from the channel, the spin diffusion is a pure spin current that travels along the channel, as shown in Figure 1.2a. This is known as electrical spin injection and the signal can then be detected in the second FM known as the FM_{det}, since the spin accumulation on this FM_{det}/NM can give rise to a measurable voltage as shown in the example. The reason is that since the electrochemical potentials of the up and down spin states must remain continuous across this interface causing a gradient in the electrochemical potential to form. Since the FM is magnetized, a gradient in the electrical potential develops and is realized as a measured voltage difference $V = \mu_{ch} - eV$. Figure 1.2b shows the NLSV for a thermally injected spin current. Since there is no current passed through any part of the NM channel, and purely through the FM_{inj}, the spin accumulation can only be diffused through the thermal gradient created across the NM channel. This is why it's known as a nonlocal measurement since all charge current should be separated from the detection voltage taps. The black arrows within the FM wires depict the magnetization of them, which should be lying in the plane of the wire. Figure 1.2c shows what happens when you measure the R_{NL} signal as a function of external H swept along the axis of the FM wires, showing 4 different regions in the results. Because the FM wires are intentionally designed to have different widths, this causes them to have different coercivities. As a result, there is a region in the R_{NL} vs. H curve when the magnetizations of the FM wires are antiparallel (AP). When in saturated states P_p and P_n, the FM wires have magnetizations along the same direction, or parallel, and the R_{NL} measured as a result of spin transport is maximized. In the region where the magnetizations are AP

AP_p and AP_n, the R_{NL} is shunted due to the opposite spin accumulations in the FM wires. This region of the AP signal depends on the width of the coercivity difference between the two FM wires. It is important to note that the cartoon depicted is shown for an ideal case when the first order fits of the IV curves are taken since higher orders correspond to thermal effects, which have their own corresponding relationships vs. H, such as the anomalous Nernst effect (ANE).

1.3. MAGNETISM AND EFFECTS

The materials studied in this thesis are a variety of magnetic materials. Because spintronics relies on the spin of the electron to transfer information, magnetic materials play an important role as the magnetization of a material is a result of the spin landscape, along with other contributions. The type of magnetism the material displays will directly influence the charge and spin transport, and give rise to unique features attractive to the implementation in spintronic devices. Although there are various types of magnetism a material can display, this thesis will focus on ferromagnets (FM), antiferromagnets (AFM) and ferrimagnets (FIM), with measurements done by SQUID magnetometry to confirm the type of magnetism.

1.3.1. FERROMAGNETS, ANTIFERROMAGNETS AND FERRIMAGNETS

Macroscopically, magnetization can be thought of as the magnetic dipole density of a material, M and is related to an external magnetic field H by the equation

$$M = \chi_m H, \tag{1.1}$$

where χ_m is the magnetic susceptibility[54]. Magnetic dipoles in a solid material manifest from multiple contributions. These dipoles are typically referred to as atomic moments and denoted as μ_m. Atomic magnetic moments are a result of the complex electronic configuration of that particular material: Electron-electron interactions will determine how the electron spins are oriented with respect to each other, the chemical

bonding of atoms will determine the orbital contribution to μ_m from the electrons, and the spin orbit coupling that aligns the spin and orbital angular momentum.

The interaction between two electron spins is referred to as an exchange interaction with the energy written as

$$\boldsymbol{E_{exch} = -2J_{ij} \sum_{i<j} S_i \cdot S_j,} \tag{1.2}$$

where J_{ij} is the exchange integral for the two electron spins i and j and and S_i and S_j the spin operators.For the purposes of explaining the difference between ferromagnets, antiferromagnets and ferrimagnets we will focus on this interaction. When electronic configurations of electrons in atoms form, they must abide by the Aufbau principle, the Pauli exclusion principle, and Hund's rules. This can lead to interesting electronic configurations that result in unpaired electrons. In the example of transition metals, it is the 3d electrons that are unpaired and the number of unpaired electrons depends on it's location in the periodic table. For Fe, there are 4 unpaired 3d electrons, and due to the interatomic exchange interaction the spins will align depending on the value of the exchange constant J_{ij} with i and j being the two interacting electron spins. If $J_{ij} > 0$ the spins will align parallel to each other, resulting in a ferromagnet, like Fe. Since all the atomic moments will be in the same direction, a ferromagnet will display a net magnetization, $M_{net} > 0$. If a ferromagnetic material is heated to it's Curie temperature, T_c, it will lose it's spontaneous magnetization and become a paramagnet, a magnetic material/phase with no magnetic order and $M_{net} = 0$. As a FM material is cooled to absolute zero, its M_{net} approaches a maximum, since there is less thermal agitation of the magnetic moments. At absolute 0, all atomic moments are aligned perfectly parallel in an ideal FM. As previously talked about, when a current is passed through a conducting FM, the charge current can become spin polarized. This is the case for FMs such as Fe, or

Co, in which the 3d electron states are responsible for the spontaneous magnetization, and the charge carriers as they make up the conduction electron band.

If $J_{ij} < 0$ then the spins will align antiparallel, resulting in an antiferromagnet, or a ferrimagnet. An antiferromagnetic material favors antiparallel alignment of its spins, with a $M_{net} = 0$. Similar to FM materials, AFMs lose their magnetic order above a certain threshold temperature. In an antiferromagnet it is known as the Néel temperature, T_N. However, below T_N, the antiparallel coupling between spins leads to a magnetic ordering that has no spontaneous magnetization. This type of antiparallel coupling is also referred to as antiferromagnetic (AF) coupling. A term used to describe two or more spin, or magnetic, sublattices with $J_{ij} < 0$. For there to be a $M_{net} = 0$, the two, or more, magnetic sublattices must have complete compensation of the magnetic moments. Otherwise, there would exist a M_{net}. AFM are popular materials for spintronics since they resist perturbations from exernal fields well. Unlike FM, when the $M_{net} = 0$, an external field has a more difficult time affecting the magnetic sublattices. AFM are also known to exhibit large magneto-transport effects, and demonstrate ultrafast dynamics. The ultrafast dynamics are a key factor for applications in spintronics, since it was experimentally observed that AFM have larger resonant frequencies than that of FMs[31].

There can also be the case where $J_{ij} < 0$, but $M_{net} > 0$. This material is known as a ferrimagnet (FIM). Just like the case of the AFM, the magnetic sublattices are AF coupled, yet there exists a $M_{net} > 0$. Because of this, FIM materials can be mistaken for a FM, due to their spontaneous magnetization below their T_c, and have been applied commercially in the past through ferrite compounds, which were intially thought of to be FM[61]. Greatly depending on the magnetic coupling of the individual magnetic sublattices, a FIM can display typical FM behaviour in its magnetic phase, although there are times when they can display AFM behavior as well. In the simplest case of a two sublattice FIM with $M_1(T)$ and $M_2(T)$ as

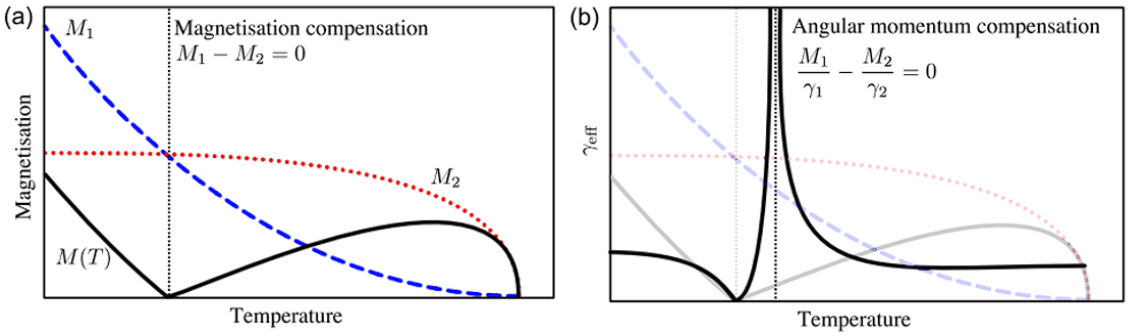

Figure 1.3: Figures from [3] **a)** Displays ferrimagnetic sublattice magnetizations and corresponding M_{net} as $M(T)$ **b)** A visual representation of the angular momentum compensation point when $\gamma_1 \neq \gamma_2$

the sublattice magnetizations, the phase diagram for M_{net} becomes dependent on the temperature dependence of each magnetic sublattice. This can give rise to a complicated temperature dependence of M_{net}, with special temperatures where the sublattice magnetizations can be completely compensated, or when the angular momentum of the sublattices can be completely compensated as shown in Figure 1.3a. These two temperatures are known as compensation temperatures[3]. When $M_1 = M_2$, the condition for magnetic compensation is met and $M_{net} = 0$, leading to a compensated ferrimagnet. If the gyromagnetic ratios γ_1 and γ_2 are different, then the FIM will have an angular momentum compensation temperature that is different than the magnetic compensation temperature, being at $M_1/\gamma_1 = M_2/\gamma_2$, Figure 1.3b. These compensation temperatures have sparked great interest in the field of spintronics so that the same attractive properties of an AFM can be extracted from a FIM in THz regimes for example[74]. The magnetic compensation temperature can also be used to create novel memory devices. Groups have explored the control of the magnetic compensation temperature through ionic migration, or voltage gating, in order to create memory devices. One example of such device is the basis of Chapter 3 and will be explained in more detail.

1.3.2. SQUID MAGNETOMETRY

To effectively understand a materials magnetic properties, SQUID magnetometry is employed in the measurement of the materials being studied to confirm it's magnetic nature, and extract important quantities. A SQUID, or superconducting quantum interference device, is an effective tool to measure the absolute magnetization that a sample is exhibiting through the use of superconducting coils. To obtain an accurate moment measurement, the sample being measured is moved through the superconducting coils and calculated through the induced current in the superconducting coils, creating a voltage that is dependent upon the sample location with respect to them. The SQUID uses an ideal dipole model to report the value of the magnetic moment in electromagnetic units, emu, and can apply an exciting field up to 7 T. This gives the option to obtain magnetic hysteresis measurements of a sample, as well as magnetization as a function of temperature measurements.

For a hysteresis measurement to take place, the sample must be mounted in an orientation chosen by the user to obtain the desired results. If the sample is polycrystalline and a thin film, this can be as simple as an out-of-plane measurement or an in-plane measurement. Measurements for these types of samples are explained in more detail in Chapter 4. If the sample is epitaxial, then more care must be taken to understand which direction the sample is mounted. Especially if different crystallographic axes and their respective magnetic properties are desired. In a magnetic material, there exist easy axis directions and hard axis directions. An easy axis is the axis a magnetic material is easily saturated, accompanied by a low anisotropic energy, while the hard axis is the axis the magnetic material is hard to become saturated, corresponding to a higher anisotropic energy.

For a hysteresis measurement to be obtained, once a temperature is chosen, the SQUID will conduct a pre-designed sequence to measure the long moment of the sample m (emu) as a function of external applied field H_{ext} (Oe). The SQUID

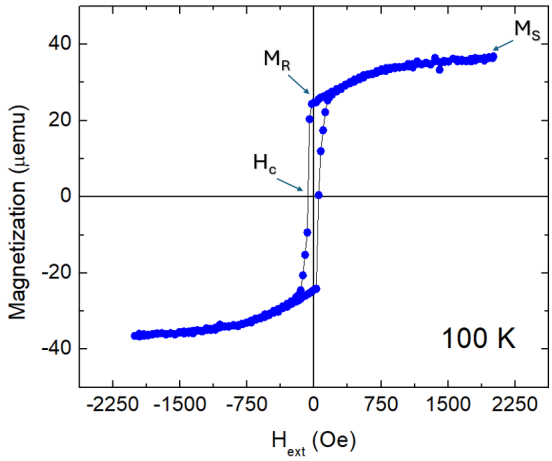

Figure 1.4: An example hysteresis of $Co_{42}Gd_{58}$ alloy at 100 K showing some of the values that can be extracted from a magnetic hysteresis measurement. M_S is known as the saturation magnetization. M_R is the magnetic remanence or the y-intercept. H_c is the coercivity or the x-intercept.

will apply a maximum external field, and measure the moment as it's swept from a positive maximum value, to a negative maximum value, back to the positive maximum value. The step size of the field is a user selected value, and when performing the sweep, the SQUID pauses to obtain an accurate dipole model fit to accurately output the moment measured for that field value. An example of a hysteresis curve for a FM/FIM along its easy axis is shown in Figure 1.4 to show the various characteristics of a hysteresis measurement. The reason it is called a "hysteresis" is because the curves are hysteretic in nature, and, in the case of a FM, lack inversion symmetry, leading to the ubiquitous nature of the magnetic hysteresis shown as an example in Figure. This hysteresis curve is a useful tool to extract certain magnetic properties of the material being measured. Because the output of the measurement is in emu, if the volume of the magnetic materials is known, then the unit emu/cc can be achieved to be converted to a magnetization M (emu/cc), which can be compared to other measurements more accurately. The values extracted from a magnetic hysteresis as shown in Figure 1.6 are the saturation magnetization M_S which is the value of magnetization when the sample is completely saturated. The remnant magnetization

or M_R is the y-intercept of the hysteresis curve. This value is a measure of how much magnetization remains in the sample when the field is returned to 0. The last value shown in the example is the coercivity or H_c, which is a measure of how much field is required to return the sample to a magnetization value of 0.

To further identify the type of magnetic material being measured, a magnetization vs. temperature curve could be taken with the SQUID. This is where the magnetic history of the sample is very important. The samples are usually loaded into the SQUID at 300 K (around room temperature), and to measure the magnetization vs. temperature, the sample has to be cooled to a desired temperature. If the magnetic material at hand has a T_c or T_N below 300 K, then during the loading procedure the sample would be in its paramagnetic phase. If the sample is cooled in a magnetic field, referred to as field cooling (FC), then the magnetic landscape that arises during ordering will be affected by the field it's cooled in. When the sample is cooled below it's ordering temperature at zero field, this is known as zero field cooling (ZFC). The distinction between the two when displaying data is important because the material can have dramatically different relationships as a function of temperature, giving more insight onto the mechanisms that contribute to the sample's magnetization. In future chapters, the distinction between the two becomes important to identify certain characteristics, such as glassy magnetism, or ordering temperatures such as T_c and T_N.

1.3.3. ANOMALOUS HALL EFFECT

The anomalous Hall effect (AHE), since it's discovery in 1881, has been one of the most fundamental transport properties of ferromagnetic materials. It was observed by Hall that when replacing a normal metal with a FM, the measured Hall effect was up to 10x larger in the case of Fe. The AHE is a relativistic effect on the electrons in a material with a net magnetization, creating an asymmetry in the charge carrier populations of the material. As the electrons are transported through the FM,

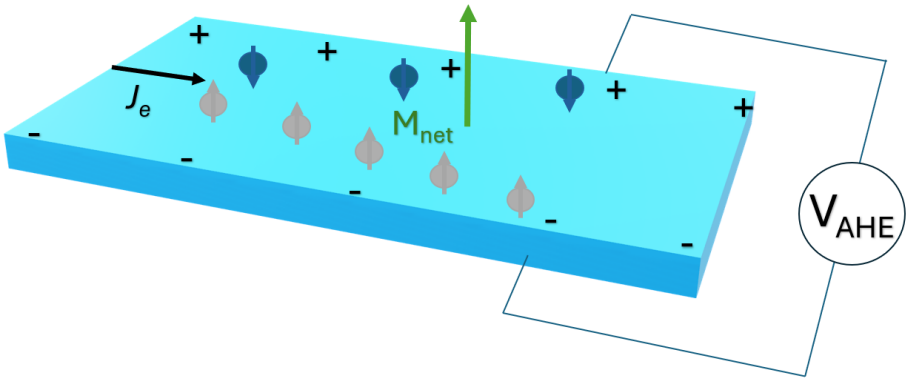

Figure 1.5: A Schematic of the AHE. As a charge current J_e is passed through a FM material with M_{net}, the charge carriers are deflected normal to the current direction through relativistic effects. The result is an asymmetry in the charge accumulation on the surfaces of the material. This gradient in the electric potential can be measured with voltage leads as depicted as V_{AHE}

three main contributions to the transverse voltage are from the intrinsic deflection, side jump, and skew scattering mechanisms. These relativistic effects are the same mechanisms that give rise to the SHE as discussed previously, excpet in this case they are creating an asymmetry in the charge populations. A schematic view of the AHE is displayed in Figure 1.5, with voltage taps displaying the transversely generated electric potential. In Chapters 3 and 4, the AHE is a unique tool to measure the magneto-transport of the FIM devices. By applying an external field in the same axis as the magnetization vector, a square hysteresis loop is measured in the V_{AHE} vs. H_{ext} as it's swept from a positive maximum, to a negative maximum, and back. Similar to a M vs. H_{ext} hysteresis when performing magnetometry, the AHE will display a square loop if it's measured along the easy axis of the magnet. Since the AHE is an electrical measurement, it's a probe of the conduction electrons in the material being measured. This means that in a typical 3d FM, the 3d electrons that are polarized due to the magnetization are the charge carriers that become deflected. In the case of a TM-RE ferrimagnet, it is a direct readout of the sublattice magnetization of the TM, since the magnetism in the RE is a result of the 4f electrons, which interact

inter-atomically with the conduction electrons through an exchange interaction. This means that in the case of a fully compensated FIM with $M_{net} = 0$ an AHE voltage can still be generated as a result of the deflection of the 3d magnetic sublattice. In future chapters, the AHE is used to confirm perpendicular magnetic anisotropy in FIM sample by measuring the V_{AHE} vs. H_{ext} making sure H is oriented perpendicular to the plane of the thin film. If a square loop is measured, then the material exhibits PMA.

CHAPTER 2:

NONLOCAL RESISTANCE IN MEASUREMENTS IN AMORPHOUS YTTRIUM IRON OXIDE

This chapter is a result of a co-authored paper. The contents presented are most relevant to understand the contributions I made, which are the electrical measurements done on the amorphous Yttrium Iron Oxide (a-Y-Fe-O). Magnetometry measurements were conducted by Mike Roos, and amorphous Germanium (a-Ge) electrical measurements were done by Sam Bleser.

2.1. INTRODUCTION

Understanding in which regimes spin information can be transmitted through insulating magnetic materials is currently a major area of study in spintronics. The focus is often on materials with predominantly antiferromagnetic exchange interaction, whether these result in a ferrimagnetic state such as in yttrium iron garnet ($Y_3Fe_5O_{12}$, or YIG), or in a bulk antiferromagnetic state such as nickel oxide (NiO), chromium dioxide (Cr_2O_3), or iron oxides such as hematite (Fe_2O_3)[1]. This spin transport is measured using a range of experimental techniques including spin pumping[75, 21, 88], the spin Seebeck effect,[44, 27] and non-local resistance measurements[27, 22, 85, 41, 45, 13, 81, 59, 58, 12, 16, 17, 68, 34] In these experiments, charge transport through the nominally insulating ferri- or antiferromagnetic films is assumed to be negligible, though some authors have demonstrated very clearly that in thin epitaxial YIG films the band gap is reduced from the bulk value $E_g = 2.8$ eV to near 2.0 eV[69]. This has important impact on non local voltage measurements, particularly when large currents are used to excite nonlinear effects.

In many of these experiments, disorder in the magnetic state plays an important role, and in the most dramatic cases researches have explored spin transport in amorphous systems including amorphous films prepared with the same ratio of Y, Fe, and O atoms as ordered YIG (often abbreviated a-YIG, though here we use a-Y-Fe-O, since the term "garnet" is a specific reference to a crystalline state)[76, 77, 18, 83]. Theoretical predictions of spin transport in disordered magnets have also been presented, though the conditions assumed for the disordered magnetic systems studied are not exactly mapped to the properties of a-Y-Fe-O[70, 53, 29, 35]. Spin Pumping[76] and spin Seebeck effect measurements with a-Y-Fe-O inserted between an epitaxial YIG spin source and Pt spin detector showed spin diffusion length in the amorphous component between 1 - 10 nm, while our group previously explored non-local resistance measurements where large signals persisted over distances of many microns[77]. More recently two groups have published non-local resistance results that put fairly stringent limits on the possibility of magnon-mediated spin transport in a-Y-Fe-O[18, 83]. Gomez-Perez, *et al.* compared non-local resistance using a combination of Pt and Cu strips, with separation of 10 μm. These experiments showed the same sign of voltage when both the Cu and the Pt were used as the detector, as well as clear increase in voltage as a function of temperature, indicating that the signals have an origin in charge flow[18]. Yang *et al.*, performed non-local and local (measuring transport in a vertical heterostructure), using Pt and permalloy electrodes. In both FMR-driven spin pumping and purely electrical experiments, these authors saw no evidence of long-distance spin transport, though they did report increased spin mixing conductance at the a-Y-Fe-O/permalloy interface[83] In all these experiments, but particularly in the non-local resistance measurements, contributions from charge transport through the amorphous system must be carefully considered. As epitaxial YIG films are often prepared from annealing of amorphous precursors, and since a range of nanolithographic processing steps could introduce disorder at the interfaces with YIG and other materials, the charge transport and magnetic properties of dis-

ordered a-Y-Fe-O could potentially impact a broader range of the many spintronic devices based on YIG.

Amorphous semiconductors, including recently explored amorphous oxide semiconductors[49], have been studied extensively and have a range of important applications for large-area electronic devices. The strong disorder in the system leads to Anderson localization of the electronic states near the band edges and the boundary in energy between these localized states and extended states in the mobility edge[42]. In addition, a high level of defect states often forms near the middle of the gap, and nominally undoped amorphous semiconductors show electronic transport through these localized states via Mott's variable-range hopping mechanism, which has a characteristic temperature dependence (in the absence of correlated electron effects) at low temperature (T) given by

$$\sigma = \sigma_0 e^{-(T_0/T)^{1/4}}, \tag{2.1}$$

where σ_0 and T_0 are constants.

We first present simple dc circuit models that clarify how dc leakage currents can generate non-local voltages in these experiments, and how they interact with various geometries of metal strips. We then present measurements of charge conductivity from 200 K - 300 K, magnetic susceptibility, photoluminescense and non-local resistance in a-Y-Fe-O. We compare the charge conductivity and non-local resistance measurements explicitly to amorphous germanium films. These results clearly show charge conductivity via the Mott variable-range hopping mechanism, indicating that both materials are best described as amorphous semiconductors. The non-local resistance measurements show clear correlations with the charge conductance in both a-Ge and a-Y-Fe-O. We also clarify the conditions for observation of spin transport in non-local resistance measurements in the presence of charge transport, and compare

non-local resistance measurements made using two common measurement techniques: quasi-dc current reversal, and lock-in detection with a known range of ac frequencies. In spin transport experiments where the magnetic order can be manipulated to clearly isolate spin effects, and when other potential complications can be controlled, these approaches have been previously shown to agree[19]. Data presented here shows that reactive components of the non-local measurement circuit can cause artifacts in the quasi-dc measurement that mimic the spin transport signal in certain geometries, causing serious challenges for studies of systems such as antiferromagnets and disordered spin systems where the magnetic order is not easily manipulated.

2.2. EQUIVALENT CIRCUIT MODEL OF CHARGE LEAKAGE

Figure 1 shows a schematic view of a non-local spin transport experiment where spin is injected and detected via the spin Hall effect (SHE). Two strips of a metal film that supports spin charge conversion (here characterized as a spin Hall effect, though any mechanism converting charge current to spin current could be employed), are in contact with a spin transport medium as shown in Fig. 1a. In the case of a purely insulating magnetic medium, the spin can excite magnons that flow to the distant contact, length L away, and be detected via the inverse spin Hall effect when the spin current flows into the metal strip. If the spin medium also allows charge to flow, this leakage current can flow across the spin transport medium to the (typically) much lower resistivity metal detector, eventually returning to the opposite charge terminal as shown in Fig. 1b. Here we show two of the many possible current paths as black lines. Note that since electrons have negative charge, the electron drift velocity direction is opposite to the arrows shown, which indicate the direction of current flow. The portion of the current flowing along path $i_{c,1}$ will generate spin current according to the SHE. The portion of the current that follows path $i_{c,2}$, and similar paths, can lead to significant current density, $\vec{J}$, present in the detector strip. According to Ohm's law, $\vec{E} = \rho\vec{J}$ where ρ is the charge resistivity, this current density must be accompanied by an electric field $\vec{E}$, which is parallel to the current as indicated by

the orange vector. This electric field leads to a voltage drop on the Pt wire, which is measured at the terminals, V_{nl} vs. I_{bias}. However, as shown in Fig. 1c, when the current flowing in the sense of path $i_{c,1}$ leads to a spin current that is injected downward into the transport medium, it flows through the medium and then upward into the detector. The inverse spin Hall effect (ISHE), assuming the detector has the same sign of the spin Hall angle as the injector, causes both spin up and spin down electrons to collect at the positive voltage measurement terminal when positive I_{bias} is applied, as indicated. In open circuit conditions for the voltage measurement on the detector strip, the electrons cause a charge accumulation that leads to an electric field. As indicated in the figure again with an orange vector, this electric field points in the opposite direction as the field in Fig. 1b, and leads to the opposite sense of the potential difference. A measurement of this voltage as a function of bias current when the experiment is dominated by spin flow in the medium will show a slope of the IV curve that is negative. This is often taken as a proof of spin transport, though we will show that certain purely electrical artifacts can also mimic this sign reversal.

The simple view of charge flow in a SHE-driven non-local transport experiment, shown in Fig. 2a, can be represented with the lumped-element circuit model shown in Fig. 2c. The requirement for the current to return to ground after any shunting by a nearby metallic strip means that, at an absolute maximum, the top half of the film is available to allow charge flow from the injector with resistance R_{inj} to the detector with resistance R_{det}, with the lower half returning the current to low potential. Thus the parallel charge conductance path is formed with effecte shunt resistors $R_{vb}/2$, where R_{vb} is the total resistance of the spin transport medium between the relevant contacts, determined in our case by measureming current flow in response to a voltage bias. This avoids thermal, thermoelectric, and other non-ideal effects in typically very high resistance measurements. Any charge that flows across the spin transport film travels through the metallic detector, producing the voltage drop measured as a non-local voltage, V_{nl}, before returning to ground. We calculate this voltage using

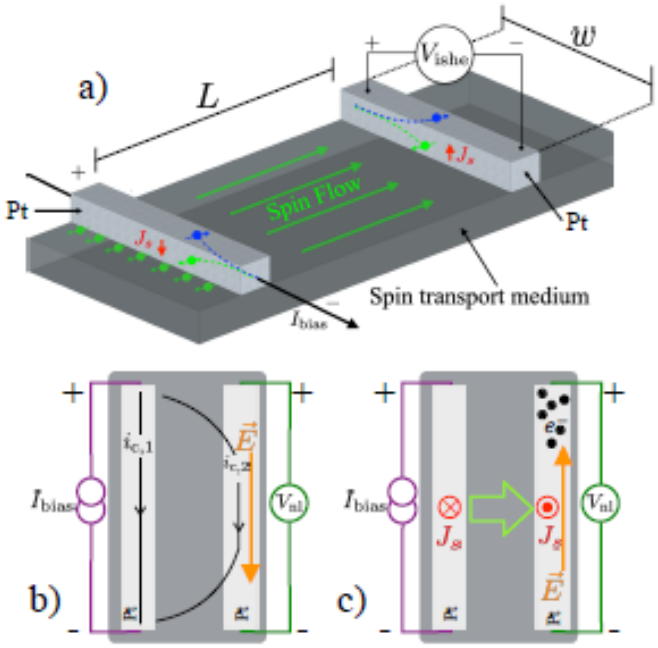

Figure 2.1: **a)** Schematic of SHE-driven non-local spin transport. Typically two Pt strips with length w along the charge flow direction, separated by a distance L, are placed in contact with a spin transport medium. A charge current, I_{bias}, driven into the injector strip (here shown at left) is converted to spin current via the SHE. This is injected into the spin transport medium, where it travels to the distant Pt strip. The resulting spin current absorbed into this Pt detector generates a charge coltage via the ISHE. **b)** A top-view schematic of a charge leakage contribution to a non-local voltage measurement. If the spin transport medium also allows charge flow, charge current can flow from the injector through the spin medium into the distant Pt strip. This travels down the typically much lower resistance Pt strip, generating a voltage with a positive sign with lead polarity chosen as shown by the + and - symbols. The charge then returns to ground by passing back through the spin medium. **c)** Schematic view of spin transport in the same geometry, clarifying the direction of spin flow. The opposite sense of the spin flow in the injector and detector leads to a non-local voltage with the opposite sign from charge leakage.

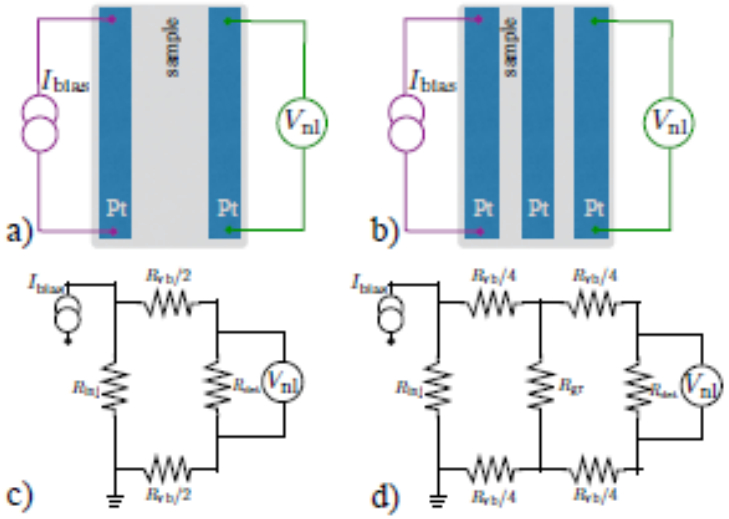

Figure 2.2: Schematic views and circuit models describing dc charge leakage in SHE-driven non-local spin transport experiments. **a)** A top-down schematic view of a typical lead arrangement where Pt strips are in contact with a sample spin transport medium. **b)** A similar view with a third metallic strip added between the spin injector and the detector. **c)** Simplified circuit model describing charge leakage in the standard two-strip geometry. When R_{vb} is large compared to R_{inj} and R_{det}, a small portion of the total injected bias current flows on the right current path and generates a non-local voltage V_{nl} via leakage. **d)** A modified circuit model demonstrates the possible reduction in V_{nl} in dc from the third metal strip.

$$V_{nl} = I_{bias} R_{det} f (1 - \frac{R_{vb} + R_{det}}{R_{vb} + R_{inj} + R_{det}}), \tag{2.2}$$

which represents the relevant current division with the addition of the factor f, which accounts for the difference between the actual charge flow paths and those used in this highly simplified lumped-element model. We expect f to be a small number, and the experiments below suggest is is on the order of 0.01 for our work. When $R_{inj}, R_{det} < R_{vb}$ Eq. 2.2 is simply:

$$V_{nl} \simeq I_{bias} R_{det} f (1 - \frac{R_{vb} + R_{det}}{R_{vb} + R_{inj} + R_{det}}), \tag{2.3}$$

and the term in parentheses is the expected non-local charge leakage resistance.

We observe that intermediate metal strips can potentially reduce the leakage current in dc, though also add capacitance and inductance to the circuit and make any ac or effectively ac measurements less clear to interpret. In dc we can model such an insertion of a "guard rail" as shown in Fig. 2b using the circuit shown in Fig. 2d. Here, the third metal strip, with resistance R_{gr} provides an additional low resistance region in the middle of the sample. The film resistance between the injector and detector at each step is approximately halved, so we take $R_{vb}/4$ to be the film resistance in each branch of the circuit. Again applying simple current division, we can write the guarded leakage voltage as:

$$V_{nl,gr} = I_{bias} R_{det} f f^* (\frac{R_{inj}}{R_{inj} + R_{eff}})(\frac{R_{gr}}{R_{gr} + R_{vb}/2 + R_{det}}), \tag{2.4}$$

where the effective resistance of all elements other than R_{inj} is

$$R_{eff} = \frac{R_{vb}}{2} + \frac{R_{gr}(R_{vb}/2 + R_{det})}{R_{gr} + R_{vb}/2 + R_{det}}, \tag{2.5}$$

and f^* takes into account the different effective geometry of charge flow from the guard rail to the detector strip from the idealized model. As before, when R_{vb} is the largest resistance, Eq. 2.4 is simply

$$V_{nl,gr} \simeq I_{bias}(f\frac{R_{inj}R_{det}}{R_{vb}})(f^*\frac{4R_{gr}}{R_{vb}}), \tag{2.6}$$

and the leakage resistance is reduced from the simple model of Eq. 3 by the factor $4f^*R_{gr}/R_{vb}$. Assuming that the charge conductivity of the sample medium is uniform, that $f^* \simeq f$, and with a value of R_{gr}/R_{vb} on the order of 10^{-2} or smaller, this factor could cause a reduction of leakage voltage by several orders of magnitude for purely dc measurements. This overly simple model makes a number of somewhat speculative assumptions. Two-dimensional finite element calculations, on both simple lead configurations and the more complicated geometries used in experiments, show similarly dramatic reductions in dc charge leakage, though these also rest on the assumption of a uniform conducting medium.

2.3. EXPERIMENT

We prepared amorphous Y-Fe-O films by ambient temperature RF sputtering from a $Y_3Fe_5O_{12}$ target onto amorphous Si-N coated silicon substrates. For a-Y-Fe-O we explored two methods for patterning metal leads to measure charge transport and test non-local spin transport. These were deposition of the sample film on Si-N/Si substrates with pre-patterned strips of 40 nm thick Pt with a 10 nm thick Cr sticking layer, and patterning of Pt and Cu strips on the top of the surface of the samples via e-beam lithography (EBL) and lift-off. For the EBL lead patterns, we also prepared the lead patterns on a highly insulating Si-N coated Si substrate with no other film

added. Fig. 3a is a scanning electron micrograph top-view of an example of the EBL-patterned leads. Fig. 3b shows a cross-sectional view of these lead patterns, which we produeced with three different injector-detector separations and, for one separation, with an additional Cu lead. To form these we used a PMMA layer (Microchem 950 PMMA A3) with Co-PMMA underlayer (MMA(8.5) MAA EL 6), each spun for 5 s at 500 rpm then for 45 s at 2000 rpm, and baked at 180°C. We sputtered platinum leads after reaching base pressure 4×10^{-8} Torr at 100 W in 3 mTorr of Ar, giving a growth rate of 0.125 nm/s. We evaporated the Cu leads after reaching base pressure 7×10^{-7} Torr, at a rate $\simeq$0.14 nm/s. Before the Cu deposition, the sample film surface was Ar plasma cleaned in a separate vacuum chamber for 1 min.

The pre-patterned Pt strips are shown in an optical micrograph in Fig. 3c and in a schematic cross-section in Fig. 3d. These strips are a section of the Pt leads on thermal isolation platforms our group developed and uses for thermal characterization of thin films,[64, 65, 2] as was the case for our initial spin transport studeies of a-Y-Fe-O.[77] The strips are 40 μm wide, with a 10 μm separation between adjacent conductors, and a total length of $\simeq$12 mm. Both the Cr and Pt were e-beam evaporated at similar base pressure and patterned via optical photolithographic lift-off.

For all transport measurements the substrates are mounted on the cold finger of a sample-in-vacuum cryostat using gold-coated OFHC copper sample mounts. Leads are ultrasonically wire-bonded and a radiation shield installed to ensure an isothermal sample environment. Transport measurements use standard computer-controlled source-meter equipment. Voltage-biased a-Y-Fe-O film resistance was measured with a Keithley 2400 sourcemeter. We compare two methods for measuring the non-local IV and R: the "quasi-dc" measurements using either the differential conducatance or "delta mode" measurement features of the Keithley 2182a/6221 nanovoltmeter and precision current source, and frequency-dependent ac measurements using a Stanford Research Systems 830 lock-in amplifier, using an external function generator and bias

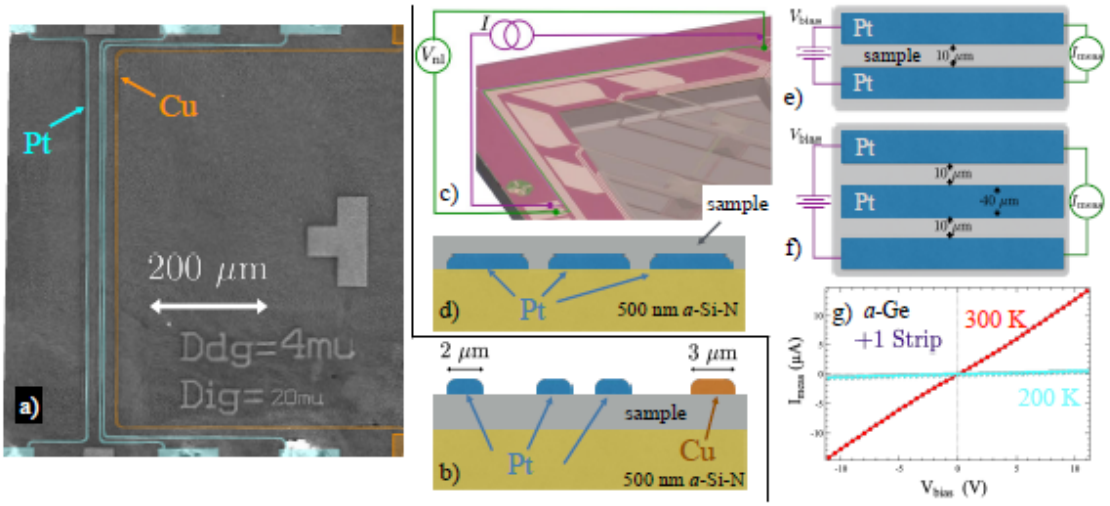

Figure 2.3: **a)** False-color scanning-electron micrograph of Pt and Cu leads patterned via EBL (here on a 75 nm thick a-Ge film, a 200 nm thick a-Y-Fe-O film was also used.) Leads shown in blue (orange) are 25 nm thick Pt (Cu). We produced three different patterns with varying Pt lead separations. **b)** Cross-sectional schematic of the EBL samples, with Pt and Cu lead width indicated. **c)** Optical micrograph of the pre-patterned Pt leads on a a-Si-N substrate, with connections indicated schematically. **d)** Cross-sectional schematic after deposition of a sample film. Scale is approximately correct for the case of the a-Ge film. **e-f)** Schematic views of the voltage biased setup used to measure the resistivity of the amorphous semiconducting samples (distances indicated relate to pre-patterned leads). Since the Pt has many of orders of magnitude higher conductivity than the sample films, the total length of the current path used to determine ρ is only the distance between the Pt strips, as indicated. **g)** I_{meas} vs. V_{bias} for the geometry shown in **e** for the a-Ge sample measured at 200 K and 300 K for pre-patterned Pt leads shows predominantly linear response.

resistor to apply the ac bias current. Most experiments were performed at relatively low bias current, and used a 90kΩ bias resistor that is much larger than the $\sim$ 1kΩ resistance of the injector strips. To apply the largest bias currents (up to 7mA), we used much smaller bias resistance (in some cases we used only the in-line lead resistance). Where this was done, we observed no qualitative change in the balance between in-phase and out-of phase components of the ac signal.

We performed photoluminescence measurements of a-Y-Fe-O by focusing the light from a 405 nm diode laser through a 0.40 NA objective onto the samples at a 30 degree angle from their surfaces to minimize back reflected excitation light in the measurement. The focused spot was roughly 5 μm in diameter and all measurements were taken at room temperature under vacuum. The signal was passed through a 410 nm long pass filter to remove any remaining back scattered excitation, coupled into a multimode optical fiber, and routed to a fiber coupled spectrometer with 1nm resolution. 100 spectra for each of the amorphous and polycrystalline samples were taken and averaged, with data points more than 2σ from the average excluded. A set of dark spectra were collected under the same conditions and subtracted from the signals and pixel noise was cmoothed with a moving average filter over 40 pixels.

We characterized the magnetic properties of the a-Y-Fe-O films using a commerical SQUID magnetometer, with automated temperature control from 2 K - 400 K using reciprocating sample methods to increase the signal-to-noise ratio. [56] We measured a matching Si-N coated Si substrate to determine the magnetic background, which was subtracted from the total signal measured from the a-Y-Fe-O/Si-N/Si samples. We mounted samples in a laminar flow hood using dedicated non-metallic tools and clean gloves to minimize contamination from dust and other potential sources of spurious magnetic contributions.

We conducted polarized neutron reflectometry (PNR) measurements using the Polarized Beam Reflectometer at the NIST Center for Neutron Research. An inci-

dent 0.475 nm neutron beam was polarized with magnetic moment parallel (+) or antiparallel (-) to a magnetic field, H, applied along the plane of the sample. We measured the spin analyzed non spin-flip specular reflectivities – and ++ as functions of wavevector transfer Q along the sample growth axis. PNR data was reduced with Reductus[47] and Refl1D.[39] Model fitting of specular PNR data allows us to infer the depth profile of the nuclear and magnetic scattering length densities, the latter of which is proportional to the in-plane sample magnetization, M. Temperature-dependent measurements were taken in a 3 T field at a temperature of 5 K, and then from 50 K - 300 K in 50 K steps. The 5 K measurements were taken over a broad Q-range, while those at higher temperatures were taken only over a range sufficient to characterize the lowerst Q spin asymmetry (difference in ++ and – divided by the sum) peak. The nuclear profile determined from the 5 K data was used for modeling of the higher temperature data.

2.4. RESULTS AND DISCUSSION

We begin by presenting magnetic characterization of the a-Y-Fe-O films. This material is perhaps most accurately described magnetically as a speromagnet, [11, 10, 9] where strong antiferromagnetic exchange interactions with randomized local anisotropy results in a magnetic state qualitatively similar to a spin glass. The central and most repeatable feature of this material, clearly seen in Fig. 4a and also observed in previous studies, [20, 7] is the splitting between the magnetic susceptibility, χ, vs. T measured when the material is cooled to low T in zero field (ZFC) and that measured when cooled in a field (FC). In the SQUID magnetometer data shown in red (ZFC) and black (FC) symbols in Fig. 4a, where both the measurement and cooling fields are 5000 Oe (0.5 Tesla), this splitting falls between 40 K and 50 K. This freezing temperature is in line with previous measurements, and we have observed this feature across all thicknesses and batches of films we have investigated. The blue symbols with error bars in Fig. 4a were measured via polarized neutron magnetometry in an applied field of 3 Tesla. These agree well with the SQUID data at nearly all measured

temperatures. The inset of Fig. 4a shows magnetization, M, vs. applied field, H, (plotted with units of emu/cc, 1 emu/cc = 1kA/m) for three temperatures, showing linear behavior at 300 K, with slight deviations at lower T on either side of the freezing temperature. As expected for a disordered material with strong antiferromagnetic exchange interactions, nearly any laboratory-scale magnetic field is insufficient to significantly magnetizr the material, and no approach to saturation is seen.

Figs. 2.4b and c compare inverse susceptibility, χ^{-1} vs. T for two a-Y-Fe-O films with 200 nm thickness, grown in two different sputtering runs (roughly one year apart). While both samples show the freezing as discussed above, the details of the susceptibility above the freezing temperature are significantly different. Sample 1 (Fig. 4b) shows to fairly distinct regimes of linear behavior, which one can view as two distinct exchange strengths, as indicated by two different Curie Weiss θ, as seen by the linear fits shown in blue and green. Both are large and negative, indicating antiferromagnetic exchange. Sample 2, shows a different overall magnitude, with a smaller χ (larger χ^{-1}), and is better characterized by the single θ with the lower value near 70 K. This suggests that despite the consistent observation of the freezing temperature, there is some degree of variability in the disordered magnetic landscape that can occur from sample-to-sample. Fig. 4d compares M vs. H at 300 K for a-Y-Fe-O (red symbols, on right y-axis) to the saturation magnetization value for bulk crystalline YIG (green dashed line, on left y-axis). Note that these axes represent very different ranges of M such that the maximum value observed for a-Y-Fe-O is $< 1\%$ of the YIG saturation magnetization, again as expected due to the disorder, strong antiferromagnetic exchange interactions, and resulting high degree of frustration.

Figure 7a) plots charge resistivity, ρ, vs. temperature, T, for 200 nm thick a-Y-Fe-O film and a 78 nm thick a-Ge film, determined from current measurements under voltage bias as shown in the inset schematic. Both materials have large ρ in this T range spanning room temperature, but are significantly lower than values

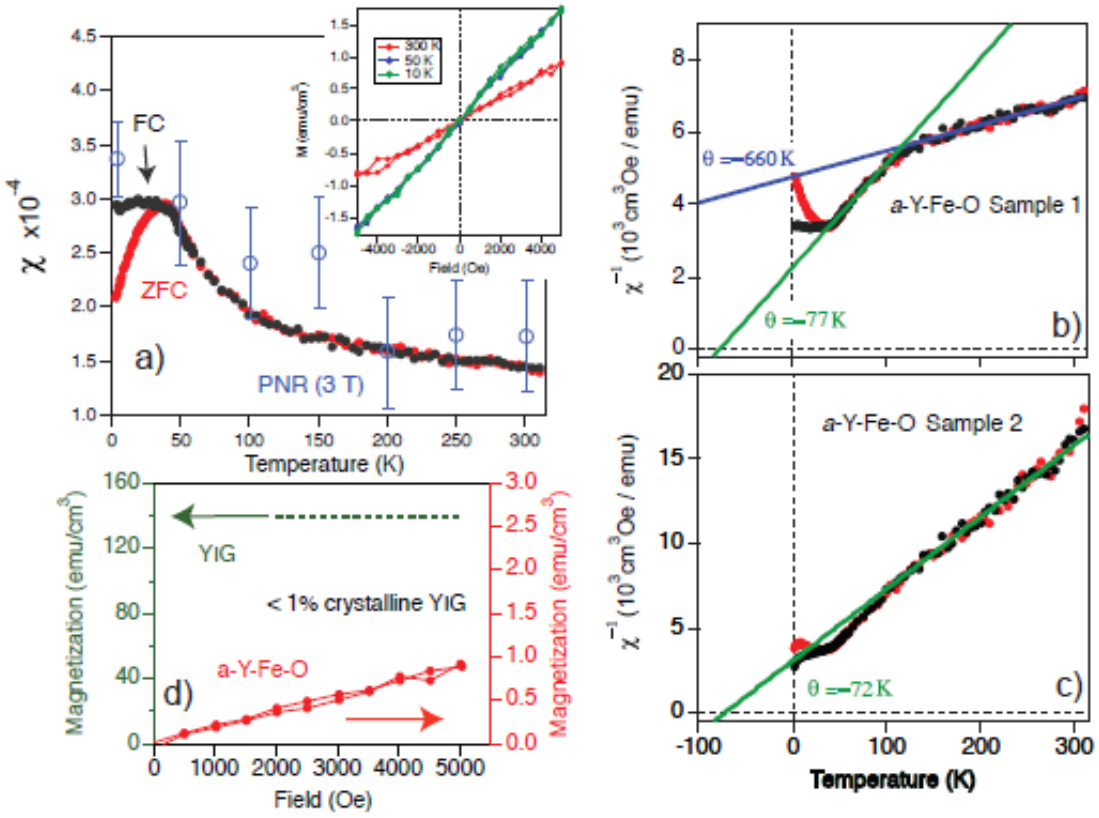

Figure 2.4: Magnetic characterization of a-Y-Fe-O with panels ordered clockwise from top left.**a)** χ vs. T for 200 nm thick a-Y-Fe-O measured via SQUID magnetometry at 5000 Oe in field cooled (black symbols) and zero field cooled (red symbols) states. The splitting between 40 - 50 K indicates a spin freezing associated with the disordered magnetism in a-Y-Fe-O. Blue symbols with error bars were measured at 30,000 Oe via polarized neutron reflectivity. *Inset:* M vs. H at three temperatures shows predominantly linear behavior at modest fields. **b)** Inverse susceptibility, χ^{-1} vs. T for one a-Y-Fe-O sample shows two regions with different effective Curie-Weiss parameter, θ. **c)** χ^{-1} vs. T for a second sample grown via the same techniques at a later date shows different magnitude, with only the lower value of θ though with approximately the same spin freeizing temperature. **d)** Comparison of M vs. H for a-Y-Fe-O (red symbols and right axis) with the saturation magnetization of bulk crystalline YIG (green dashed line and left axis) at 300 K. Even at large laboratory-scale applied field, the disordered system gains a tiny fracton of the moment seen in the ordered material.

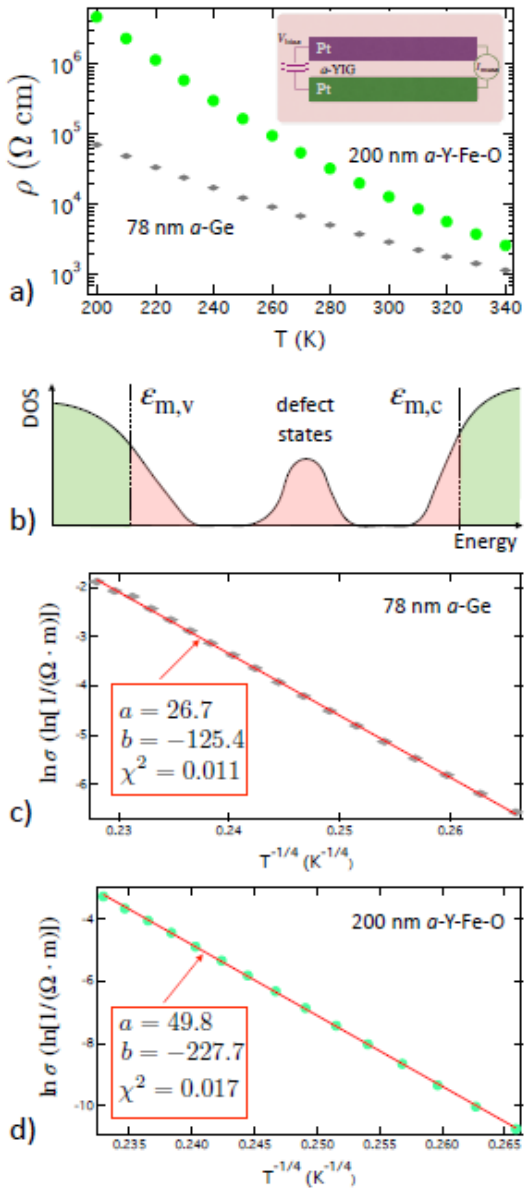

Figure 2.5: **a)** Charge resistivity ρ vs. T from 200 - 340 K for both 200 nm thick a-Y-Fe-O and 78 nm thick a-Ge. *Inset:* Schematic view of the voltage biased measurements used to determine the large values of R which were converted to ρ. **b)** DOS vs. energy for an amorphous semiconductor showing extended states in green, the mobility edges $\epsilon_{m,v}$ and $\epsilon_{m,c}$ and localized states in red, which include a large density of defect states near the center of the gap. **c-d)** lnσ vs. $T^{-1/4}$ for a-Ge (panel c) and a-Y-Fe-O (panel d) show linear behavior lnσ= $a + b(T^{-1/4})$, indicating charge transport via variable range hopping. Linear fit parameters and χ^2 are indicated for each fit.

reported for both bulk YIG and epitaxial thin film YIG, which have $\rho > 10^7 \Omega$ cm at 300 K. [69] As discussed above, this reduced ρ or increased electrical conductivity, σ is often a consequence of the formation of defect states in the gap as shown in the schematic density of states vs. energy diagram shown in Fig 7b. Here we also indicate the mobility edges, $\epsilon_{m,c}$ and $\epsilon_{m,v}$, that divide localized from extended states in the conduction and valence band edges, respectively. Electrical conductivity in a-Ge is dominated by variable range hopping in these localized states for temperatures near and below room temperature.[50, 40, 8] Figs. 7c-d demonstrate charge conduction dominated by variable range hopping via these localized states in both the a-Ge and a-Y-Fe-O films. These plots show $\ln\sigma$ vs. $T^{-1/4}$, with linear least-squares fit lines showing excellent agreement with variable range hopping (Eq. 1) over the 200 K $> T >$ 340 K temperature range. Fit parameters and resulting χ^2 values are indicated in each plot. We also attempted fits to a simple thermal activation model, where $\ln\sigma$ would be proportional to $1/T$. These resulted in poor agreement, with χ^2 an order of magnitude or more larger than the hopping fits. It is possible to achieve better agreement if one assumes two regimes form in T, with different activation energies. Such a view is not out of the question for disordered conductors of various sorts, [4, 78] and a definitive determination of the transport mechanisms, electrical conductivity in the a-Y-Fe-O at levels that can affect non-local transport is clear.

Before detailing the consequences of this hopping conductivity on non-local transport experiments, we first clarify the effective ac nature of the "delta mode" and differential conductance measurements performed with the Keithley nanovoltmeter (NVM) and current source. In Fig. 8 we compare a series of electrical measurements on Pt strips formed via EBL on a highly insulating 500 nm Si-N layer deposited on a Si substrate. These strips, with geometry shown schematically in the inset to Fig. 8a, have the same layout as the device shown in Fig. 3a, with a "guard rail" Pt strip placed between the injector and detector strips, and the charge resistance between the Pt strips is unmeasurably large at all T described here. In Fig. 8a we present the

non-local voltage determined by numerical integration of the differential conductance voltage measured with the Keithley NVM in response to a series of excitation currents, I_{bias}, sourced by the linked Keithley current source. In both this measurement mode and the related "delta mode," the timing between voltage measurements is affected by a parameter termed "delay time" by the manufacturer. Fig. 8a plots curves acquired for 4 different choices of this parameter, ranging from 2 ms (the shortest possible value), to 20 ms. Strikingly the non-local VI curve has the negative slope often associated with spin transport in experiments with a spin conductive media (obsiously absent here). The slope of the curve also clearly depends on the choice of the value of the delay time. High values of this parameter (not shown) begin to display an apparent oscillatory response, though the overall negative slope vanishes.

Measurement of the same exact Si-N device in the same cryostat with controlled ac excitation of $I_{rms} \simeq 75$ μA and detection of V_{nl} with a lock-in amplifier indicates that the apparent negative VI slope measured by the "quasi dc" method is an artifact arising from a large reactive component of the effective circuit. Fig. 8b shows measured ac voltage response, $V_{nl,ac}$, to a well-defined ac bias current, including the in-phase component, X, the out-of-phase component, Y, and the total magnitude, $R = \sqrt{X^2 + Y^2}$ for two different base temperatures, 298 K and 78 K. Despite a relatively low f, the out-of-phase component dominates the response at all f and T shown here. This is seen clearly by R and susequently Y having much larger values than the in-phase response X. Note that measurements of a resistive load (for example when both excitation current and voltage detection are attached to a single Pt stip), are dominated by the in-phase component, as expected. This large out-of-phase component of the response is perhaps not surprising when neither charge nore spin can flow from injector to detector, leaving capacitive and inductive coupling as the only mechanisms for modifiying the detected voltage. However, the large reactive component presents a special challenge for the "quasi dc" measurement.

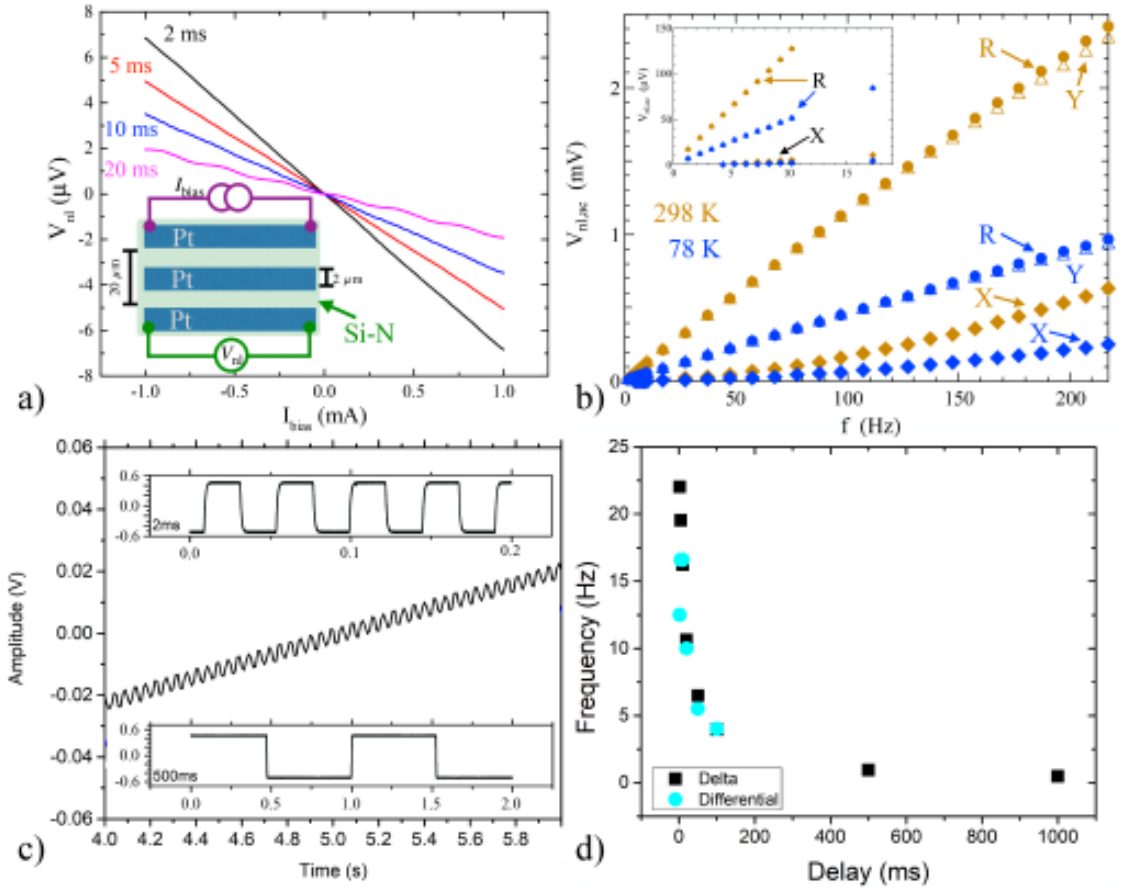

Figure 2.6: Comparison of "quasi-dc" and ac lock-in measurements of non-local voltage on a device with Pt strips patterned directly on Si-N, with no spin or charge conducting medium. **a)** V_{nl} vs. I_{bias} determined from the "quasi-dc" differential conductance method with four different choice of the delay time parameter, starting with the 2 ms value that is the default for this instrument. All show a spurious negative slope. *Inset:* Schematic view of the non-local leads with current bias and voltage measurement connections indicated. **b)** $V_{nl,ac}$ vs. f measured with a lock-in amplifier, where I_{bias} is a sine wave with frequency f and the V_{nl} is connected to the lock-in input. At both 298 K (orange symbols) and 78 K (blue symbols), the response is dominated across this frequency range by the out-of-phase response. *Inset:* Closer examination of the $f < 17$ Hz range. **c** Measurement of the time dependent voltage across the injector strip under "quasi-dc" excitation plotted vs. time. The main panel shows the excitation pattern during a differential conductance measurement, and the upper and lower insets show the excitation during the "delta mode" measurements for two choices of delay time, as indicated in the insets. **d)** Effective frequency of the "quasi-dc" measurements determined from the time dependent measurements plotted vs. the delay time parameter.

Fig. 8c plots the current excitation from the Keithley current source during the "delta mode" or differential conductance vs. time. The main plot shows the current ramp used during a differential conductance measurement, while the top and bottom insets show the current excitation used in "delta mode" for two different choices of the "delay time" parameter discussed above. All o f these signals are better understood as low-frequency ac excitations. We explicitly measure the period of these signals for a rnage of the "delay time" parameter, and plot the resulting ac frequency vs. the delay time in Fig. 8d. This shows that the default, short delay time used in these measurements in the functional equivalent of exciting a device with a square wave with f between 5 and 22 Hz. As we show in Fig. 8b, and is typical in non-local measurements of spin transport through nominally insulating systems,[12] at these frequencies the Si-N device is dominated by out-of-phase response. This explains the apparent sign inversion of the resistance as determined either from the VI curves measured with the Keithley differential conductance mode or the resistance reported by the "delta mode." Here the dc NVM is sampling an effective ac response at a time where the ac voltage has swung out-of-phase. Such a signal can therefore not be taken as strong evidence of spin transport without additional verification from magnetic field dependence or other control experiments.

Figure 9 compares non-local voltage measurements made with quasi-dc and ac lock-in techniques when an amorphous germainum film is placed beneath the metal strips. The quasi-dc measurements, measured at a delay time of 2 ms, compare four different strip geometries, shown schematically in the insets in Figs. 9a-b. Fig. 9a compares two "unguarded" geometries with strips separated by distance $L \simeq 20$ μm. The grey line presents results with both Pt injector and detector, where the copper-colored line was measured with Pt Injector and a copper detector. Both curves have a positive slop at $I_{bias} = 0$, which could be interepreted as arising from charge leakage through the Ge. The values of these slopes, determined from the linear term of a polynomial fit to the curves, define the first-order non-local resistance, $R_{1,nl}$

and are given for each curve in the figures. The lower voltage and smaller slope for the Cu detector, seen in the values from linear fits that are indicated in the figure, could arise from the lower resistance of the Cu detector strip, as suggested in Eq. 3. The deviation of the IV curve for the Pt strip apparent here seems to match expectations for Joule heating, though we caution that the presence of the electrical artifacts related to the quasi-dc measurement complicate such an interpretation. Fig. 9b shows similar data but with the additional Pt strip plaved between the injector and detector, while somewhat increasing the overall distance between injector and detector at $L \simeq 30$ μm. Here both quasi-dc VI curves invert sign, though the Cu detector again shows much smaller values than the Pt. Without confirmation from the ac lock-in measurements, this pattern could be interpreted as evidence of spin transport, clarifying the importance of the more controlled frequency-dependent non-local voltage measurements shown at right.

Fig. 9c-d presents $V_{ac,nl}$ vs. f measured with a lock-in amplifier again on the same device with the same Pt strips and the same cryostat wiring. As with the control experiment on Si-N, the ac voltage is dominated by a large out-of-phase component, with $X < R$ even at frequencies beloq 10 Hz. This is true for both the case with no third Pt strip (panel c) and when the "guard rail" is inserted (panel d). Note the larger $V_{ac,nl}$ range in d), indicating as the Si-N case that one major consequence of the additional Pt strip is to increase the reactive components of the overall circuit, leading to a larger out-of-phase component. The inset shows a closer view of the low f region, again clarifying that the in-phase portion of the response is always less than the reactive, out-of-phase component. With the third Pt strip in place, at the $\simeq 17$ Hz effective frequency of the quasi-dc IV measurement, the out-of-phase component is 10x greater than the in-phase response. Without the third Pt strip, the out-of-phase response still dominates, but R is roughly half of the three-strip value. This significant shift in the reactive impedance drives the false inversion of sign between the experimental conditions of Fig. 9a and Fig. 9b.

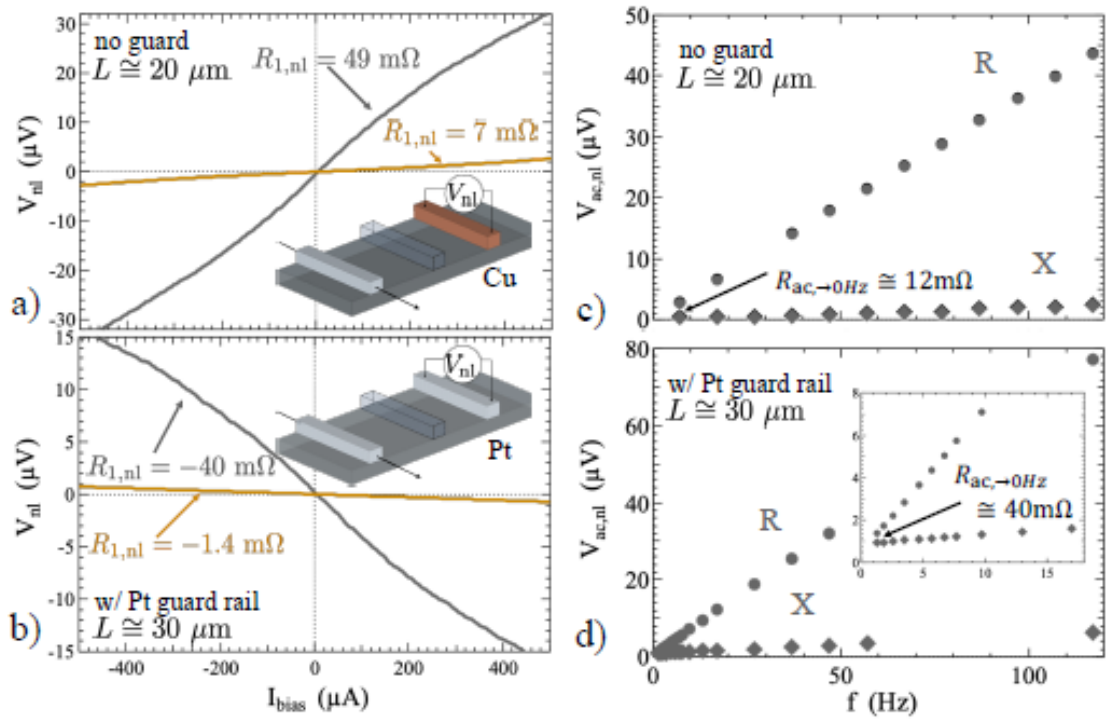

Figure 2.7: Non-local voltage measurements on 75 nm thick a-Ge. **a)** V_{nl} vs. I_{bias} using the "quasi-dc" measurement with Pt injector and Pt detector strips with $L \simeq 20$ μm (grey line) and using a Pt injector and Cu detector (orange line). *Inset:* Schematic view of the non-local setup with a Cu detector, with the possible third "guard rail" strip shown in outline. **b)** Similar V_{nl} vs. I_{bias} measured with "quasi-dc" approach with the additional third stirp in place. An apparent inversion of the sign of the non-local resistance occurs. **c)** Lock-in amplifier measurements of the same device with Pt strips and no "guard rail," $V_{ac,nl}$ vs. f with ac excitation $I_{rms} \simeq 5$ μA (similar behavior occurs for larger excitations). As seen on Si-N, the signal is dominated by an out-of-phase component is significantly increase. No negative values of non-local resistance are observed. *Inset:* Closer view of the $f < 17$ Hz range shows the in-phase component always remains below the total signal magnitude.

In Fig. 9c-d we also indicate the value of the non-local resistance determined from the in-phase ac voltage component for the two-strip "no guard" and three strip "w/Pt guard rail" cases, extrapolated to zero f based only on the lowest frequency data points. If the Pt strip between injector and detector was actually acting to shield the detector from charge leakage, one would expect this value to be dramitcally lower in the "guard rail" case. The experimental values provide no evidence of this, as $R_{ac,\rightarrow 0Hz}$ instead increases by a factor of 2 - 4x when the third Pt strip is added, and the overall distance between injector and detector increases. Though we caution that determining the true dc resistance accurately is difficult when such large reactive components of the circuit are present, the pattern shown here provides no clear evidence of the "guard rail" effect. The increase in $R_{ac,\rightarrow 0Hz}$ upon adding a strip and increasing L does not have a simple interpretation as charge leakage in a uniform conducting medium.

We now use the same two measurement techniques to examine non-local voltage measurements on a-Y-Fe-O films. Fig. 10 presents VI curves measured on "no guard" (panel a) and "w/Pt guard rail" geometries (panel b), tken with the quasi-dc technique with delay time of 2 ms (an effective ac excitation with $f \simeq 17$ Hz). As with our original work [77], these a-Y-Fe-O films were deposited on top of a pattern of wider and longer Pt strips, as shown in Fig. 3c-d. As in the case of the a-Ge, the two Pt strip "no guard" geometry shows a positive slope, but the additional strip inverts the sign of the apparent non-local resistance. Similar patterns with different overall magnitude (not shown) occur in a device with 100 nm thick a-Y-Fe-O. However, as with the a-Ge, the sign inversion cannot be interpreted as evidence of spin transport before closer examination of the frequency dependence.

Figure 11a-b compares the total ac lock-in voltage response, R (panel a), and in-phase component X (panel b), vs. f for three strip geometries patterned via EBL on top of a 200 nm thick a-Y-Fe-O with the layout shown in Fig. 3a. As seen in both

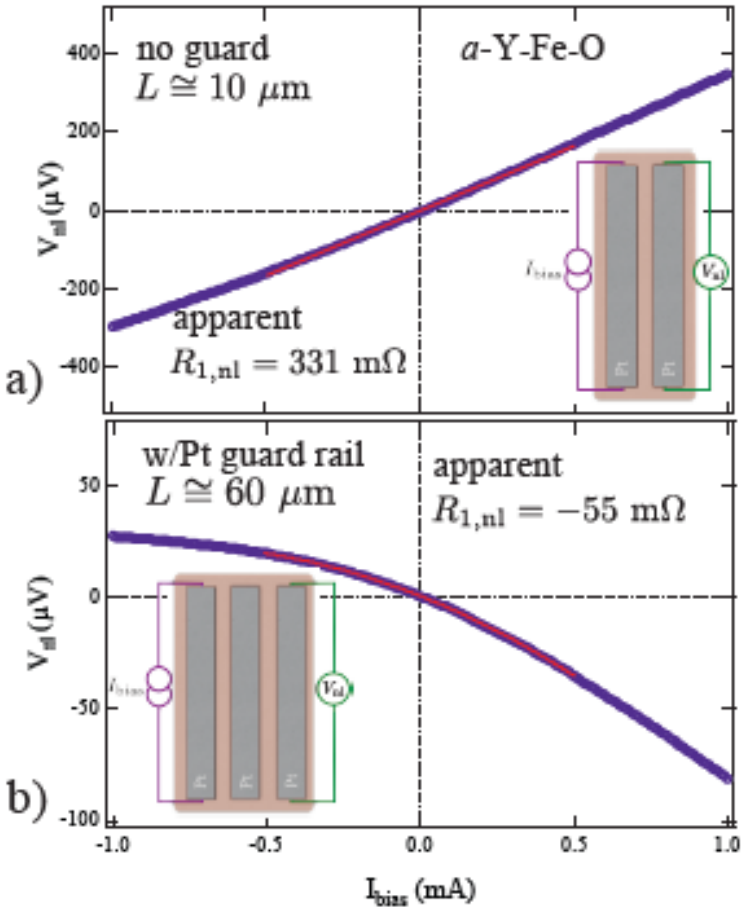

Figure 2.8: Non local voltage V_{nl} vs. I_{bias} measured using the "quasi-dc" approach on a-Y-Fe-O, using **a)** only two Pt strips, and **b)** with the addition of a third Pt "guard rail." As seen in the a-Ge case, an apparent inversion of the non-local resistance occurs. Red lines in both panels show the polynomial fit used to extract the linear component, $R_{1,nl}$. For both cases, the fit was performed from -0.5 to 0.5 mA. *Insets:* Schematic views of the lead geometries used in each panel.

Si-N and a-Ge, large out-of-phase components of the signal dominate a much smaller in-phase response, with X approaching zero as f drops. For a-Y-Fe-O, the in-phase response also has a clear component $\propto f^2$. This is also true for the corresponding Si-N and a-Ge, though less obvious in Figss 8 and 9. This f^2 dependence could be explained by a second leakage path into the detector strip, through a parallel capacitance.

Simple attempts to model this effect suggest fairly large capacitances, well in excess of the value we calculate based on the geometry of the conducting strips alone. This could indicate that interfacial capacitances from Schottky barrier effects between the metal strips and the samples play an important role. Additional work is required to confirm this speculation. Importantly, the pattern of R in panel a) shows that adding the third Pt strip increases the reactive impedance, as seen with a-Ge, which again will introduce artifical sign change in the effective 17 Hz measurement of Fig. 10. The lower resistance of the Cu detector drops both the in-phase and out-of-phase component of the signal, though the dominant component remains the out-of-phase reactive load.

In Figure 11c-d we plot R and X at $f = 1.7$ Hz vs. ac bias current I_{rms} for the same three strip geometries. While the reactive components increase roughly linearly with increasing current, the in-phase component stays essentially zero as a function of I_{rms}. The only appearance of negative in-phase voltage, the true condition for observation of non-local resistance consistent with spin transport, comes at higher I_{rms} but for the Cu detector strip, where the small spin Hall angle suggests spin transport should not generate a voltage. Not also that the additional Pt "guard rail" could be seen as somewhat reducing the in-phase signal from charge leakage, though the main effect is to increase the noise and there is still not strong evidence of the effectiveness of this approach, at least for the lead geometries we implemented here.

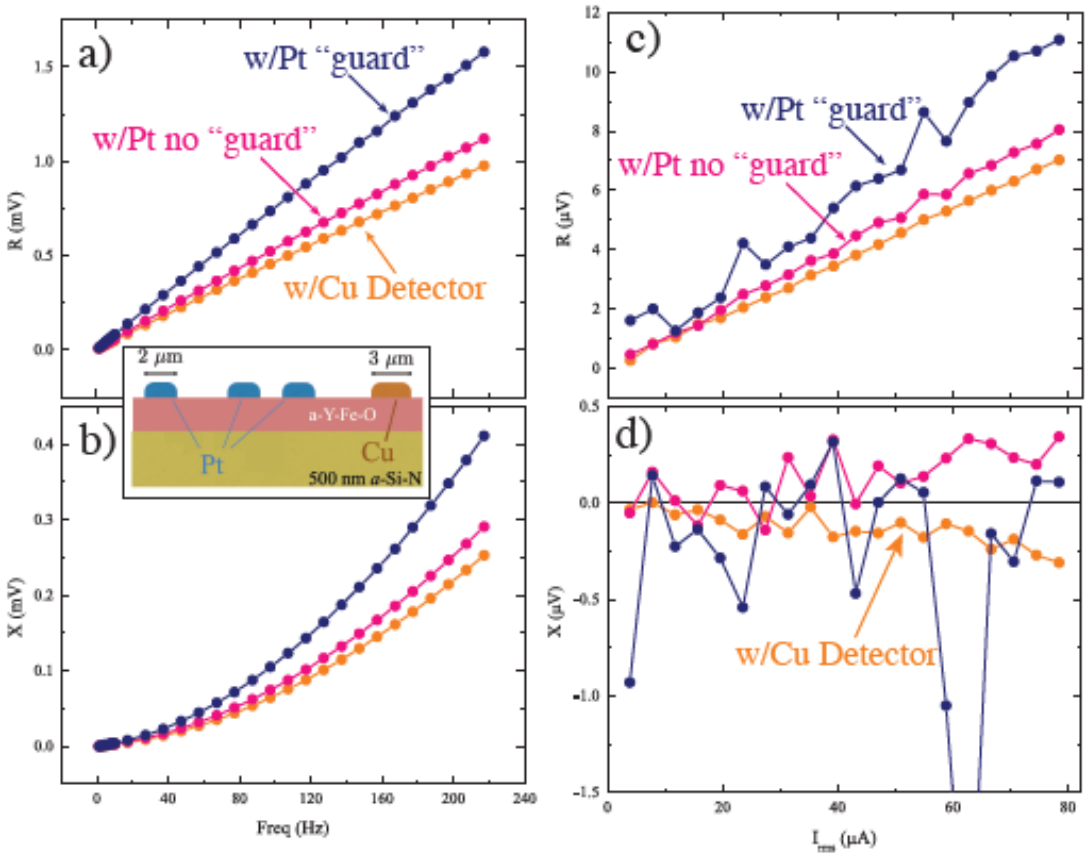

Figure 2.9: Lock-in measurements of non-local voltage on Pt and Cu strips patterned on a-Y-Fe-O. **a)** Total signal magnitude R and **b)** in-phase component X vs. f for three devices, Pt strips with no "guard" (pink symbols), using a Pt injector and Cu detector (orange symbols), and Pt strips with an additional Pt "guard" (dark blue symbols). As with the Si-N and a-Ge devices, out-of-phase components dominate the response. **c)** R and **d)** X measured at $f = 1.7$ Hz vs. applied ac bias current, I_{rms}.

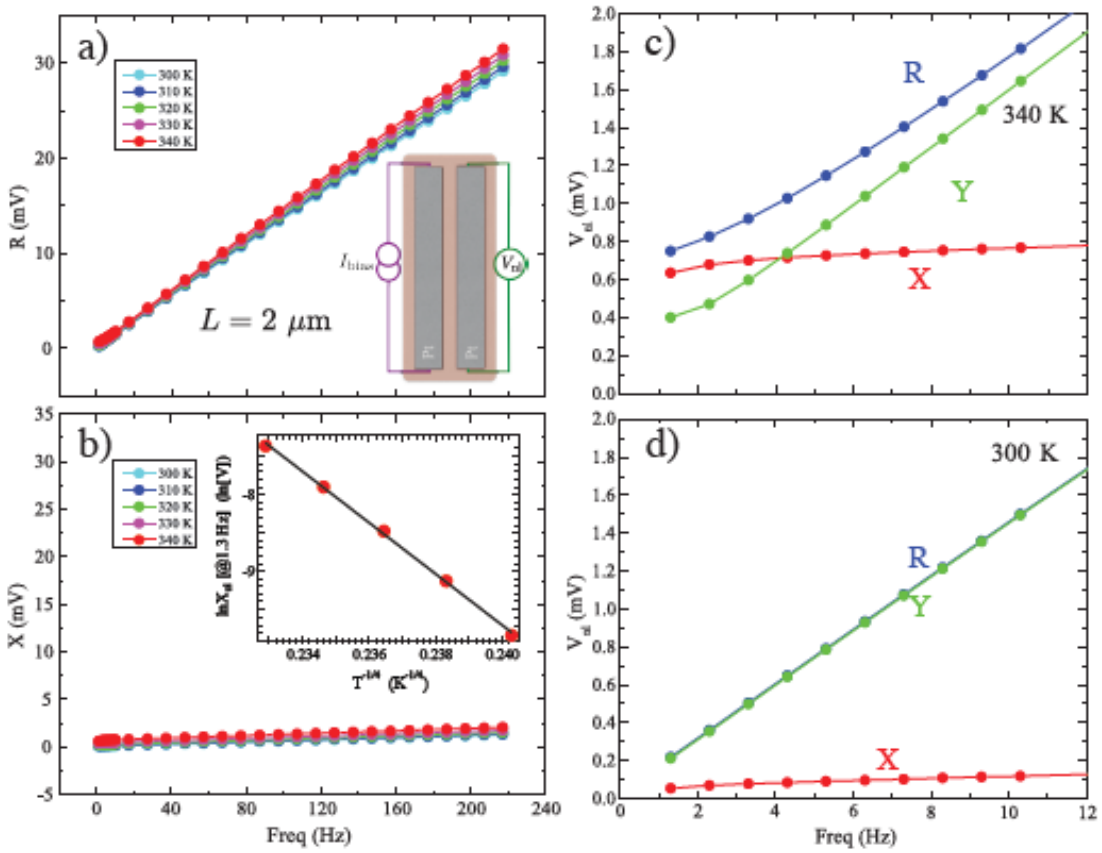

Figure 2.10: Lock-in measurements of non-local voltage on a two Pt strip device on a-Y-Fe-O with separation $L = 2\ \mu$m with a fairly large $I_{bias} = 7$ mA for five temperatures between 300 and 340 K. As in all previous devices, **a)** R is large compared to **b)** X for all $f > 5$ Hz. We separately compare R, X and Y at **c)** 340 K and **d)** 300 K. X is only larger than Y for the highest T data, but remains positive, indicating that charge leakage generates this non-local voltage. *Inset to b)*: $\ln X_{nl,ac}$ measured at $f = 1.7$ Hz vs. $T^{-1/4}$ is linear, indicating this non-local voltage has the same temperature dependence as σ, likely also driven by variable range hopping. Though this is a fairly small T range, the fit to the VRH dependence is a better match to the data than a simple exponential dependence.

Fig. 12 presents ac lock-in measurements on the simplest two-strip geometry with the smallest L we examined, at 2 μm, measured for five T, at a larger bias current $I_{rms} \sim 7$ mA. Figs. 12a and b show again that the reactive components of the circuit dominate the in-phase resistive components at all but the very lowest f, and certainly at the $\simeq 17$ Hz effective excitation frequency of the default Keithley delta-mode and differential conductance measurements. Figs. 12c and d plot X, Y, and R at low f for two temperatures, 340 K (panel c) and 300 K (panel d). We see that only at elevated T, where the charge conductivity of the a-Y-Fe-O has increased significantly, and for $f < 5$ Hz does the in-phase response exceed the out-of-phase response in the lock-in measurement. This is similar to the case for measurements of non-local spin transport in epitaxial YIG[12] though in a-Y-Fe-O, the positive sign here indicates charge leakage, and is not consistent with spin transport. Finally, in the inset of Fig. 12b we plot $\ln(X)$ measured at $f = 1.7$ Hz vs $T^{-1/4}$. Across this somewhat limited range of T, these points are well-explained by a straight line, indicating that the temperature dependence of the resistive response of the device is the same as for variable range hopping, Eq. 1, providing additional confirmation that charge leakage is the physical origin of the only reliable resistive response measured in these non-local experiments.

Contrary to our original work,[77] and in-line with later investigations of non-local voltage measurements in a-Y-Fe-O by other groups,[18, 83] this more complete and detailed investigation shows no evidence consistent with spin transport in this speromagnetic disordered semiconductor over micron length-scales. Furthermore, the charge transport we have clearly identified should be considered in experiments that claimed spin transport across much thinner a-Ye-Fe-O layers.[76]

CHAPTER 3:

TEMPERATURE CONTROLLED ANOMALOUS HALL EFFECT SWITCHING OF SYNTHETIC BILAYER FERRIMAGNET Co/Gd

3.1. INTRODUCTION

Recent work in spintronics has shown that transition metal (TM) rare earth metal (RE) ferrimagnetic (FIM) materials show great potential for creating memory and logic spintronic devices[15, 38]. In spintronics, the main goal is to use the spin degree of freedom of the electrons to carry out logic processes, or act as a means of information transport that can be more energy efficient than analogous processes with the charge of an electron. Typically, ferromagnets (FM) are used in such components because of their inherent net magnetization vector. This net magnetization causes a charge current to be spin polarized as the current passes through the material and, when in contact with a normal metal (NM), the spin polarized charge current will diffuse from the ferromagnet to the normal metal with spin diffusion lengths varying depending on the normal metal used. Ferromagnetic materials are also important for the use in Hall effect devices. Due to the spontaneous magnetization, the ferromagnet gives rise to an anomalous Hall effect. As a charge current is passed through the material perpendicular to the magnetization, a transverse voltage is generated, historically much greater than the transverse voltages generated by the normal Hall effect in a normal metal. Because the magnetization of the ferromagnet can be easily manipulated with an external field, this transverse voltage displays a square hysteresis when the external field is swept from positive saturation to negative saturation, then back to positive saturation. The magnetic coercive field associated with the FM along the

same direction of applied field will determine the coercivity of the anomalous Hall effect voltage measured as a function of external field. This is a result of the FM breaking time reversal symmetry, something a ferrimagnet material does as well. A ferrimagnet on the otherhand is different from a ferromagnet in that the ferrimagnet is a system that is antiferromagnetically exchange coupled, like an antiferromagnet (AFM) which is known to have a net zero magnetization.

Recent efforts to understand antiferromagnetic materials for their use in spintronic devices is rooted in the ultrafast dynamics that are a result of the antiferromagnetically exchanged coupled sublattices[84]. Antiferromagnetically exchange coupled systems exhibit magnetization dynamics at a ps time scale compared to ferromagnets with ns time scales[5, 73, 36]. This makes ferrimagnetic materials useful candidates for spintronic applications because their net magnetization vector can be influenced by an external field, and at the magnetic compensation temperature T_{comp}, there have been reports of increased spin dephasing length λ_{dp}[43]. In a ferrimagnetic material, the magnetic ordering arises from two or more spin sublattices that are antiferromagnetically exchange coupled. In the case of a ferrimagnet made of a bilayer stack of Co/Gd, the TM and RE are the two sublattices of atoms that are negatively exchange coupled, with unequal spin species so that there exists a net magnetic magnetization[6, 67]. This can be achieved easily in a thin film system, in which perpendicular magnetic anisotropy (PMA) is promoted so that the sublattices are antiferromagnetically coupled normal to the plane of the thin film[62]. This can be accomplished by growing a seed layer of Pt to promote this perpendicular anisotropy, along with very thin layers of Co and Gd, $<$ 3nm[52, 86]. One can take a thin film ferro/ferrimagnet with perpendicular magnetic anisotropy and measure the anomalous Hall effect using the Van Der Pauw method since it is straightforward in applying an external field that is perpendicular to the current. What makes the metallic ferrimagnet unique is that they have a compensation temperature T_{comp} associated with their magnetization versus temperature curve where the T_{comp} is the

temperature in which the net magnetization of the material is equal to 0. When the sublattices of the ferrimagnet are completely equal and opposite. In this chapter, we show how a thin film ferrimagnet that is perpendicularly magnetized can be used to create a deterministic magnetic switching device with non-volatile memory switched purely by controlling the temperature whilst measuring the anomalous Hall effect. This is only possible due to the existence of an observable T_{comp} for the ferrimagnetic thin film.

3.2. DEVICE CONCEPTS

The sublattices in a ferrimagnet can lead to unique magnetization versus temperature curves for ferrimagnets. For simplicity, assuming the mean-field behaviour of M, each ferromagnetic sublattice has it's own, bulk magnetization versus temperature relationship shown in Fig. 1a for Co and for Gd. It's important to note that the magnetization from the TM Co arises from the 3d electrons and for RE Gd it is the 4f electrons, with the 3d electrons dominating the transport properties. When these sublattices are antiferromagnetically coupled, the resultant net magnetization versus temperature can take on a unique relationship with multiple compensation temperatures. One compensation temperature is when the magnetization of both sublattices $M_1(T)$ and $M_2(T)$ are equal, $M_1(T_{comp}) = M_2(T_{comp})$. If the two sublattices have different gyromagnetic ratios, γ_1 and γ_2, then there will be a temperature where the net angular momentum is 0, and this can be at a different temperature than T_{comp}. This occurs when when $M_1(T_A)/\gamma_1 = M_2(T_A)/\gamma_2$[3]. Because a measurement like the anomalous Hall effect is a magneto-transport measurement, it is dependent on the 3d electrons of the system. This means that even in a compensated ferrimagnet with net zero magnetization, the anomalous Hall effect provides a stable electrical readout, something essential to a memory device.

Using a simple model of the the magnetization of the two separate bulk materials that are antiferromagnetically exchange coupled, we can realize a temperature driven

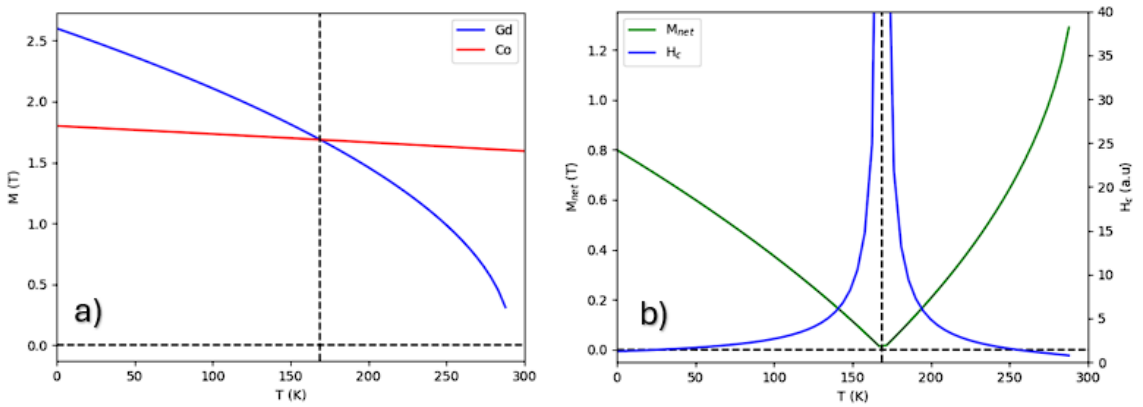

Figure 3.1: **a)** Magnetization versus Temperature for bulk Co and bulk Gd using simple model from equation 3.1 **b)** A plot showing $\vec{m}_{tot}(T)$ as the green curve from equation 3.2, and $H_c(T)$ as the blue curve. The dashed lines depict the estimated T_{comp} from where $\vec{m}_{tot} = 0$ and H_c diverges.

deterministic switching of the anomalous Hall effect state. In this model, we use a Co/Gd thin film bilayer to create a synthetic metallic ferrimagnet through the interfacial antiferromagnetic exchange coupling. Assuming mean field behavior we can construct the magnetization for each layer by the relationship

$$M(T) = M(0)\sqrt{1 - T/T_c}, \tag{3.1}$$

with T_c being the Curie temperature. A temperature when the spontaneous magnetization of a ferromagnet vanishes and becomes paramagnetic. We can assume bulk values for the parameters to model the $M(T)$ of the two ferromagnetic layers, with $M(0)$ as the magnetization at $T = 0K$. for Co, $M(0) = 1.8T$ and $T_c = 1388K$, and for Gd, $M(0) = 2.6T$ and $T_c = 292K$. The resultant $M(T)$ curves are plotted in Fig. 1a as an example of this model. In the graph there is a point in which the $M_{Co} = M_{Gd}$ known as T_{comp}. Assuming each layer is magnetized in the out of plane direction and coupled antiferromagnetically, we can construct the total magnetic moment of the

bilayer per unit area as

$$\vec{m}_{tot}(T) = |M_{Co}(T)d_{Co} - M_{Gd}(T)d_{Gd}|, \tag{3.2}$$

where M_{Co} and M_{Gd} are the saturation magnetizations of the respective layers, and d_{Co} and d_{Gd} the thicknesses. The green curve in Fig. 1b displays this result when using equal thicknesses for simplicity. The temperature associated with the crossing in Fig. 1a is easily identified as the T_{comp} in Fig. 1b when $M_{net} = 0$. Here $T_{comp} = 170K$. Below T_{comp} the Gd sublattice magnetization dominates and above T_{comp} the Co sublattice dominates. If we assume the direction of net magnetization to be positive and out of plane, above T_{comp} when the Co sublattice is dominant, the 3d electrons are in the same direction as the net magnetization, and below T_{comp} the 3d electrons are magnetized antiparallel to the net magnetization since Gd is the dominant sublattice. This is the reason the anomalous Hall effect state can be influenced through temperature, giving rise to two separate anomalous Hall effect states above and below T_c. In order to realize the switching of the AHE state, the coercivity H_c of the ferrimagnet needs to be known. The H_c for a ferro/ferrimagnet is the external field required to make the magnetization of a previously saturated magnet 0, before it is saturated in the opposite direction. In this model the coercivity, which likely arises from the interface anisotropy of Pt/Co, can be assumed to scale inversely to the magnetization m_{tot} as $H_c \propto 1/m_{tot}$, which is plotted in Fig. 1b as the blue graph, showing a divergence at T_{comp} when approaching from both sides. The high coercivity region around T_{comp} means that the saturated AHE state cannot be switched unless the external field is greater than H_c, with coercivities $> 1T$ being measured in some cases close to T_{comp}.

With the ferrimagnet perpendicularly magnetized, the anomalous Hall effect measured using a Hall bar, or the Van Der Pauw method, with the current density orthogonal to the magnetization will result in a square hysteresis. The positive and

negative saturation values of the AHE are the states in which the 3d electrons of the cobalt layer are parallel or antiparallel to the external field during saturation. For the purposes of this chapter, we can understand the AHE voltage versus external field hysteresis loops as having a positive polarity when the positively saturated voltage of the AHE voltage is greater than the negatively saturated voltage. In theory, this polarity will be opposite or, negative, when the AHE voltage versus external field hysteresis loop has a positively saturated voltage that is less than the negatively saturated one. This would be in the Gd dominated state, below T_{comp} when the Co layer is antiparallel to the external field. To realize an anomalous Hall effect memory device that is controlled through temperature, a constant external field is required in the out of plane direction. If the coercivity versus temperature relationship is symmetric around T_{comp}, then a temperature region with a desired width can be created based on the selection of the constant external field value. The width of this region where $H_c > H_{ext}$ determines the amount of temperature change required to switch the anomalous Hall effect state, creating essentially a hysteresis loop of AHE voltage, V_{AHE} *vs.* T. The purpose of the external field H_{ext} is to saturate the net magnetization vector in the same direction once the $H_{ext} > H_c$ at a temperature below T_{comp} or above T_{comp}. Using the $H_c vs. T$ curve in Fig. 1b for reference, if we choose a constant $H_{ext} = 10\ units$ and begin measuring the AHE with some arbitrary current density at 200 K, then the AHE will be in a positively saturated state given by the positive polarity at this temperature above T_{comp} and $H_{ext} > H_c$ @ 200 K. If the temperature is lowered to the T_{comp} where H_c diverges, $H_{ext} < H_c$ therefore having no ability to switch the direction of the Co layer 3d electrons, the V_{AHE} state is preserved from the beginning state. To then perform a switching event, or a writing of the opposite state, the temperature is lowered to 140 K. Here at this temperature, $H_{ext} > H_c$. H_{ext} is now sufficient enough to saturate the ferrimagnet so that the now dominant layer of Gd aligns parallel to this H_{ext}, leaving the Co layer antiparallel, and therefore the V_{AHE} is in it's negatively saturated state. From here, the process

can be reversed to write the opposite state. When going from 140 K back to 170 K, the V_{AHE} state that was written at 140 K is preserved due to $H_{ext} < H_c$. To write the opposite state, the temperature must be warmed to when $H_{ext} > H_c$ in this simple example using 200 K to be sure of the writing process.

This concept can be achieved through direct temperature control of the entire system. In this example, the temperature region where $H_c > 10\ units$ is technically between $153\ K < T < 185\ K$ giving rise to a region $T = 32\ K$. This is the region where the V_{AHE} state is stable and cannot be switched with the applied constant external field, and therefore can be shrunk by choosing H_{ext} to be greater than 10 $units$. The temperature for writing a positive or negative state is directly linked to the H_{ext} chosen and the $H_c\ vs.\ T$ of the ferrimagnet material being used. To further manipulate the temperature region, the properties of the bilayer system must be altered, such as changing the composition of the Co/Gd alloy, or bilayer being used to obtain a desirable T_{comp} and $H_c\ vs.\ T$. For this simple model it is a case of changing the thicknesses of the bilayer, but implementing may not be so straightforward as many other factors can determine the magnetic landscape of DC/RF sputtered materials, and have been shown to be very sensitive to growth conditions such as magnetostriction from substrate and seed layers[55], and Ar flow rate[33]. Even though the premise of this device is using pure bath temperature to write the state of the V_{AHE}, there are reports of using ion migration to shift T_{comp} itself by modifying the magnetic moments, and therefore changing which temperature T_{comp} occurs at, with differences in $T_{comp} > 100\ K$[28]. Other methods of altering T_{comp} and other parameters such as the magnetizations of the individual layers using similar techniques are currently being explored.

3.3. EXPERIMENT AND METHODS

To achieve a synthetic bilayer ferrimagnet, one Co and one Gd layer was sputtered on a SiO_2 coated Si wafer at a base pressure of 4 x $10^{-}7$ Torr to create an

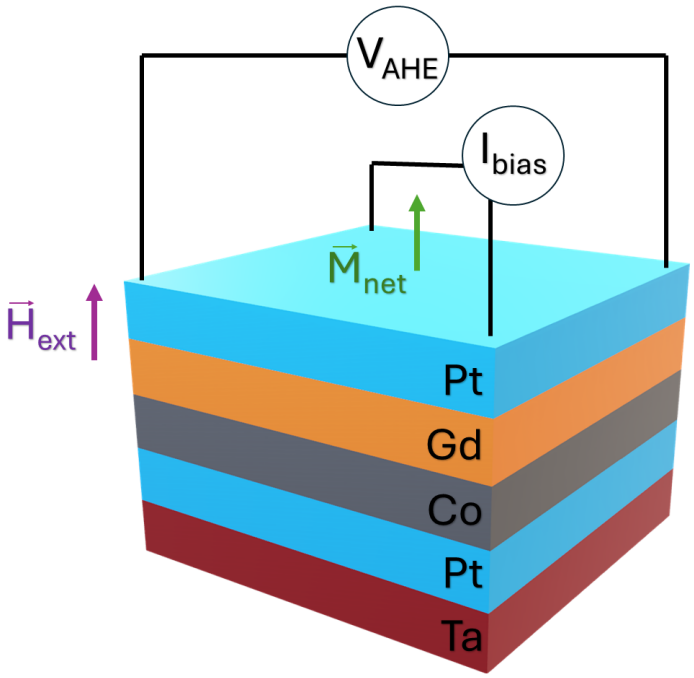

Figure 3.2: A view of the stack that is grown on the Si wafer substrate. Not to scale. The correct thicknesses are 3Ta/3Pt/(0.5 or 0.6)Co/1.8Gd/3Pt in nm. The V_{AHE} is transverse to the current density input by I_{bias}. The M_{net} and H_{ext} are perpendicular to the plane of the film.

antiferromagnetically coupled bilayer system. In one sample the thickness of each layer is $d_{Co} = 0.5$ nm, $d_{Gd} = 1.8$ nm, and in another sample $d_{Co} = 0.6$ nm, $d_{Gd} = 1.8$ nm. Using 150 W to sputter, the Co deposition rate is 0.6 /s and Gd 1.5 /s. The bilayer is sandwiched between 3 nm of Pt on the bottom to promote PMA, on top to cap and protect from oxidation, and grown on a seed layer of 3 nm Ta. A cartoon of the cross section of the stack can be seen in Fig. 2. Perpendicular anisotropy was confirmed through a measurement of the AHE showing a square hysteresis. To perform the AHE measurement, the Van Der Pauw method was employed.

Using an ultrasonic wire-bonder, current and voltage taps are bonded to the corners on the top surface of the FIM samples according to the layout in Fig. 2b. The Van Der Pauw method gives the ability to measure a voltage V_{AHE} that's transverse to the biased current I_{bias}, without having to pattern a Hall bar. The bonds connect

the external peripherals of an LN2 vacuum cryostat to the gold-coated OFHC copper sample mount. The mount is radiation shielded, and positioned so that when it is inserted into the vacuum cryostat, the sample's out of plane direction can align with the external field H_{perp} applied by an open bore split-coil electromagnet. The experiment peripherals are computer controlled current source Keithley 6221, and nanovoltmeter Keithley 2182a. The delta mode feature of the Keithley source-meter pair was used, with a $I_{bias} = 250\ \mu$A and a time delay of 2 ms.

The shape of V_{AHE} vs. $H_{\perp}$ takes on the characteristic square hysteresis when the net magnetization is along the same direction of $H_{\perp}$. The directions of H_{ext} and M_{net} are considered to be in the $+\vec{z}$, or $\perp$, direction with the $\vec{x}$ and $\vec{y}$ directions lying in the thin film plane. The square shape of the hysteresis loop confirms PMA and is a direct measurement of the direction of the 3d electrons that are undergoing the transport. The two AHE states that will be used for this device are the two states seen in the V_{AHE} vs. H_{ext} hysteresis as the positive saturated value and the negative saturated value. Above the T_{comp}, the net magnetization for both samples is assumed to be dominated by Co, therefore the hysteresis takes on the polarity which is illustrated in Fig. 3c and Fig. 3d, with the positive saturated V_{AHE} greater than the negative saturated value.

To extrapolate what T_{comp} is for our samples, V_{AHE} vs. H_{ext} was measured at various temperatures. After some preliminary tests, the temperature range selected for hysteresis loops was 110 K to 165 K in 5 K steps. The sample mount was LN2 cooled from room temperature to 110 K, then a V_{AHE} vs. H_{ext} hysteresis loop was recorded. The maximum field applied is $\pm$1500 Oe, and the sequence uses roughly a 15 Oe step. At each step point, the delta mode voltage is recorded using a 50 sample voltage measurement with the previously described settings for the source-meter. Fig. 3 (0.5 nm Co / 1.8 nm Gd) and Fig. 4 (0.6 nm Co / 1.8 nm Gd) display the V_{AHE} vs. H_{ext} for 4 chosen temperatures in both samples, with two temperatures below the

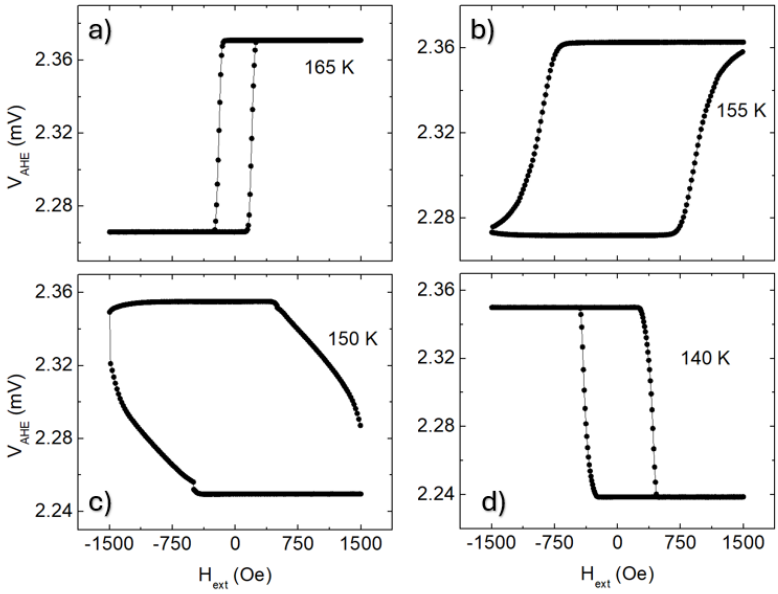

Figure 3.3: V_{AHE} vs. H_{ext} hysteresis loops at 4 different temperatures for sample with 0.6Co/1.8Gd in nm. **a)** and **b)** are below $T_{comp} \simeq 152.5 \pm 2.5$ K, and show a negative polarity in hysteresis. **c** and **d)** are above T_{comp} and show a positive polarity in hysteresis.

observed T_{comp} (a) and b) of figures 3 and 4) and two temperatures above T_{comp} (c) and d) of figures 3 and 4).

Above T_{comp} for both samples, the AHE hysteresis has a positive polarity, and a negative one below T_{comp}, in line with the expectations from the previous section. Because of the 5 K step resolution of the V_{AHE} vs. H_{ext} hysteresis loops, T_{comp} for the sample with 0.5 nm Co and 1.8 nm Gd is in between 150 K and 155 K. This is easily identified with a known polarity switch in the AHE hysteresis loops. The T_{comp} for the sample with 0.6 nm Co and 1.8 nm Gd is between 150 K and 160 K, because at 155 K, the H_c is assumed to be greater than the limits of the magnet being used: 1500 Oe. After identifying where the T_{comp} is for both samples, it was important to understand what the $H_c(T)$ of both samples were, as this would dictate what static field to apply for the temperature driven memory device. To obtain this relationship for both samples, we used the V_{AHE} vs. T hysteresis loops to record a H_c.

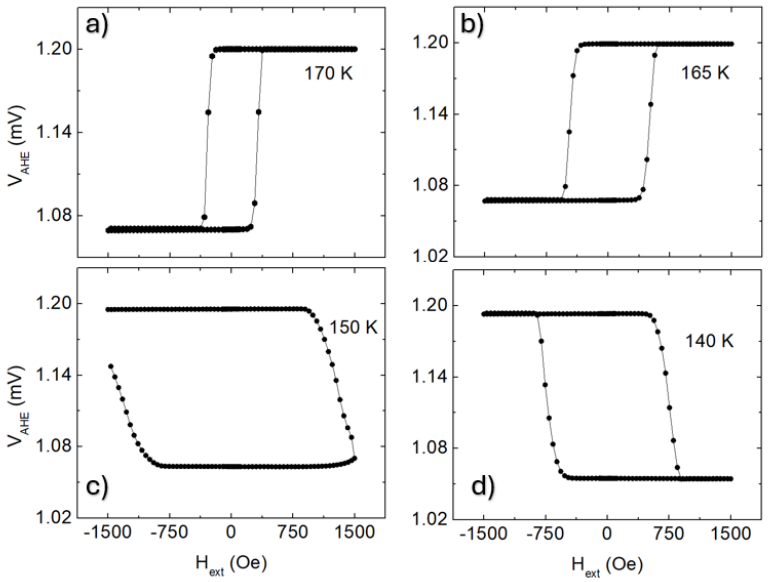

Figure 3.4: V_{AHE} vs. H_{ext} hysteresis loops at 4 different temperatures for sample with 0.6Co/1.8Gd in nm. **a)** and **b)** are below $T_{comp} \simeq 155 \pm 5$ K, and show a negative polarity in hysteresis. **c** and **d)** are above T_{comp} and show a positive polarity in hysteresis.

The H_c here is essentially the field value at the middle of the V_{AHE} switching event during hysteresis measurement. Because most of the hysteresis measurements didn't have a linear switching event from positive saturation to negative saturation, the H_c was calculated by obtaining the field value right before the switching started, and averaging it with the field value obtained for the point when switching was complete and signal was saturated. In some cases around T_{comp} there was no hysteresis recorded due to $H_c > 1500Oe$, another indicator of diverging behaviour from measurement of the AHE.

3.4. RESULTS AND DISCUSSION

By extracting the H_c from the AHE hysteresis loops, we can construct H_c vs. T for both samples. We can use these relationships to identify a H_{ext} value that would give us the desirable temperature switching range by selecting a constant H_{ext} to apply. The graphs of H_c vs. T are shown in Fig 5, and it's easy to see the

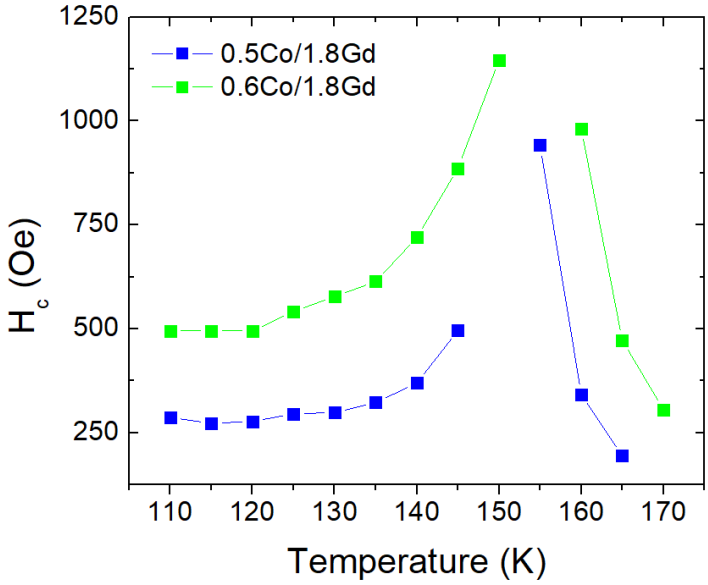

Figure 3.5: H_c vs. T for both samples calculated from V_{AHE} vs. H_{ext} showing divergence approaching T_{comp} and higher measured magnitudes of H_c for sample with slightly more Co

divergence of H_c as the samples approach T_{comp}. Another effect of the diverging H_c around T_{comp} is that some hysteresis loops do not have discernible coercivities because of setup limitations. This does not affect the ability for the sample to undergo temperature driven switching. Upon closer examination of the plots, the decay of H_c away from T_{comp} as you cool or warm is not exactly symmetric. This means that the temperature region of switching would not be symmetric about T_{comp}, but there still exists temperatures on either side of T_{comp} where H_c is equal, and would initiate the switching event once the temperature was reached. For the sample with 0.5Co/1.8Gd, 450 Oe was chosen. Based off the $H_c(T)$ curve if you apply a static $H_{ext} = 450$ Oe and cool the temperature downwards from 165 K, the V_{AHE} should switch between 145 K and 140 K. After switching occurs, if you warm the sample temperature back up, the V_{AHE} should again switch between 155 K and 160 K. For the sample with 0.6Co/1.8Gd, 750 Oe was chosen due to it's increased H_c compared to the sample with slightly less Co. At 750 Oe, the switching region should be close to that of the

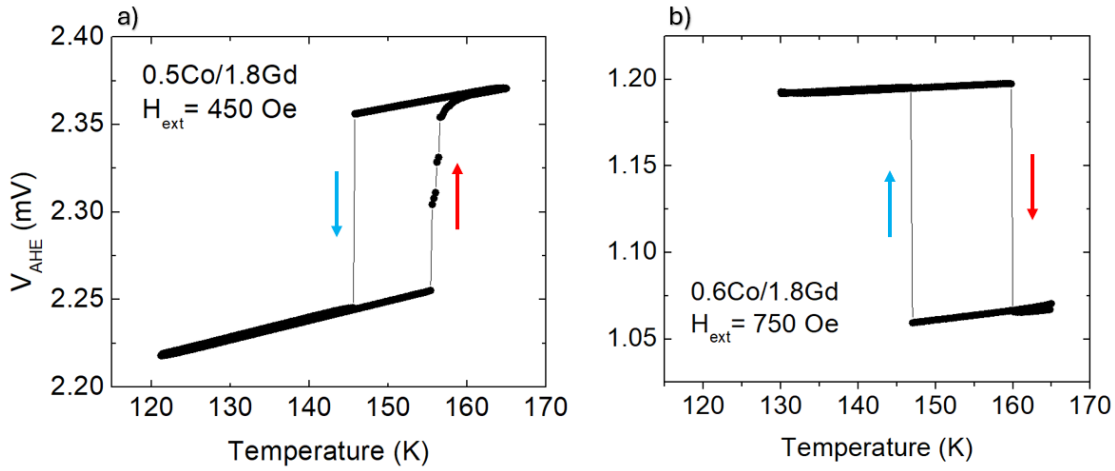

Figure 3.6: V_{AHE} vs. T of both bilayer samples. Plots show proof of concept of temperature driven switching of the AHE state when cooling first, then warming second. An applied field is labeled for both samples, and is constant throughout entire measurement period. The field is applied out of plane of the sample, along the direction of magnetization, while the AHE is measured using the Van Der Pauw method. Samples begin at the higher temperature, then are cooled while static field is applied, and while the V_{AHE} is measured. Switching occurs for **a)** 0.5Co/1.8Gd at 145 K and 159 K while **b)** 0.6Co/1.8Gd.

switching region of the sample with 0.5Co/1.8Gd. To begin the temperature driven switching measurement, the samples had to be cooled to a starting temperature of 165 K. At this temperature the chosen static H_{ext} field was applied and the measurement of the AHE was initiated using the delta mode feature just as before. In steps of 2 K, the sample was cooled to 120 K, taking a 50 sample delta mode V_{AHE} measurement at each temperature, and, to ensure an accurate measurement, the temperature was regulated at each step. The V_{AHE} vs. T plots, as shown in Fig. 6, are the results of this type of measurement. The blue arrows indicate the measurement path when cooling, and the red ones when warming. In Fig. 6a, the V_{AHE} takes on it's own hysteretic behavior as a function of temperature. When cooling the samples to 120 K, the 0.5Co/1.8Gd sample switched it's V_{AHE} state at 145 K and the 0.6Co/1.8Gd sample at 147 K. When warming, the switching events occured at $T = 159$ K for 0.5Co/1.8Gd and $T = 160$ K for 0.6Co/1.8Gd. The complete V_{AHE} vs. T hysteresis is the raw

example of a temperature driven switching of the AHE. As the field stays constant throughout, the high coercivity region around T_{comp} protects the V_{AHE} state from switching. Only when the switching temperatures are reached during the cycle will the V_{AHE} switch. In Fig 6b, it may be confusing that the AHE switching directions are opposite to that of Fig. 6a. This is easily explained by the fact that the sample was mounted with the normal of the thin film antiparallel to the positive field. Above T_{comp} the Co layer must always be the dominant contribution to the M_{net} for these samples. Since the 0.6Co/1.8Gd sample has a V_{AHE} vs. T with opposite orientation means the external field being applied in a positive saturated state is opposite to the M_{net}. Looking back on the V_{AHE} vs. H_{ext} hysteresis loops for this sample in Fig. 5, the saturated values at positive and negative H_{ext} can be confirmed to be in an opposite direction for this particular measurement. Nonetheless, the switching events in both samples were completed purely by changing the total temperature of the system, allowing for the AHE state to switch. The temperature at which the switch occurs is more accurately denoted as an anisotropic field, H_A, or the field in which the AHE reaches it's saturated state. Even though the H_c here was used to determine when the state would switch, experimentally because the AHE hysteresis loops are not exactly square, the measured H_A is a more accurate determination of when the state will switch.

Since a temperature driven switching device is a very slow process, a memory device that would be completely driven by temperature does not make much sense for applications in logic or memory processes that require switching events to take place quickly. The proof of concept here it to act as a guideline on how one can use the T_{comp} of a ferrimagnet to create a stable AHE state that can be switched with temperature. The ability to manipulate T_{comp} post growth is an avenue of approach to make a device like this more applicable. More work is being conducted into gating devices such as these, using ionic gels, or ion migration through oxides grown in the heterostructure. The ionic gels, when a voltage is applied, will populate, or depopulate

ions within the device, affecting the T_{comp}. By migrating H and O ions within the FIM, they can induce orbital reoccupations in the Gd and Co ions, capturing part of the valence electrons and therefore shifting the magnetization of the sublattices. Recent experiments have shown up to 200 K shifts in magnetic compensation temperature that more than exceeds the requirements shown in the previously displayed work[57]. The gating voltages shown for this kind of T_{comp} shift were up to 3 V, indicating that when gated correctly, the ion migration method is an effective way to make this device all electrical. Other methods of oxygen migration have also shown to affect the ferrimagnet order, leading to switching of the AHE in CoTb alloys[14]. Because an external field is required to achieve a saturated AHE state, with large T_{comp} shifts being realized, smaller fields would be required to induce the AHE saturation. In the case of the H_c vs. T curves in figure 3.5, the smallest measured H_c allowed for AHE switching was 273 Oe, even though above T_{comp} smaller coercivities were measured.

3.5. CONCLUSION

In summary, an AHE memory device controlled by temperature was observed. The proof of concept displayed in figure 3.6 showed that a switch in the AHE could be driven by a change in total temperature of the system, while a static, external magnetic field is applied. Tunability and reproducability of T_{comp} are big factors in realizing a device as such, as large fields are required to saturate the AHE states. The amorphous nature of the bilayer sample helps promote PMA, and can be easily achieved through straightforward growth procedures. Either through alloys, or through bilayers, Co/Gd ferrimagnets are ideal materials for creating PMA ferrimagnets. Besides having a temperature controllable AHE, the material's AF coupling allows for other spintronic applications through it's ultrafast dynamics and therefore having enhanced transport effects at compensation temperatures. While at T_{comp} the FIM is protected from stray fields, and even with a net magnetization of zero, the FIM still displays magnetotransport effects. The 4f electrons in the Gd, which give rise to it's spontaneous magnetization, are localized, compared to that of the 3d

electrons of Co. Therefore, the conduction electrons and their magnetization direction can be electrically measured during compensation, a useful feature for spintronic applications.

CHAPTER 4:

MAGNETOMETRY AND ANOMALOUS HALL EFFECT MEASUREMENTS OF BILAYER Co/Gd FERRIMAGNET WITH PERPENDICULAR MAGNETIC ANISOTROPY

After the demonstration of the temperature driven switching of the AHE state in a ferrimagnet, more questions came about in regards to creating ferrimagnetic memory elements with a tunable compensation temperature. The two samples measured in the previous chapter had almost identical T_{comp} with a slightly higher H_c in the sample with more Co. Efforts to produce more synthetic bilayer samples along with some alloy samples were made so that a more thorough investigation could take place. By growing more samples with varying compositions, it's possible to use magnetometry and AHE measurement methods to identify the tunable variables of the synthetic FIM, and their magnetic properties.

4.1. INTRODUCTION

Magnetic thin films with perpendicular magnetic anisotropy have sparked interest for their applicability in hard disk drives (HDD) and random access memory (RAM). With advancements in new materials and fabrication techniques, smaller and faster magnetic recording media are being realized. In magnetic storing technologies, the binary bits are stored in the magnetization directions of the nanoscale structures. Up until recently, the magnetization of the magnetic thin film regions that stored the bits often lied in the plane of the thin film. With an effort to increase storage density of recording media, materials with perpendicular magnetic anisotropy (PMA)

have shown to offer more than an order of magnitude higher in storage density than the traditional longitudinal recording[71]. First employed commercially in a Toshiba device[32], perpendicular magnetic recording PMR became widespread to address the issues that in plane recording had. Bits that lie in plane tend to give rise to a large demagnetizing field, which can erase the information of the bits if the coercivity of the material is not large enough to protect against this. When bits that have out of plane magnetization are used instead, the demagnetizing field can be lowered, allowing for a more densely packed arrangement of bits. Besides perpendicular magnetic recording, the application of PMA in STT-MRAM is also being explored, with observations of large tunneling magnetoresistance ratios and low threshold current densities showing great promise for application[30, 82, 23]. There are still hurdles with applying PMA to magnetic tunnel junctions (MTJs) as they still require significantly more power consumption to write.

It has also been shown that spin orbit torques (SOTs) have proven to be an efficient method of controlling the magnetization of FM nanoscale devices when interfaced with a heavy metal (HM). Naturally, research into the SOT manipulation of magnetization of FIMs has gained traction, with the attractive properties of a FIM due to the AF coupling. A candidate material for such applications is the transition metal (TM) rare earth metal (RE) ferrimagnet material such as CoGd. There has been evidence that ferrimagnet/heavy-metal bilayers exhibit effective SOTs that influence domain wall motion and trigger magnetization switching. This is a useful feature for integration into spintronic devices to have electrical means of manipulating magnetizations, and can have interesting features when the material displays PMA.

Since a ferrimagnetic material of CoGd consists of two magnetic sublattices, a magnetic compensation temperature exists where $M_{net} = 0$, when the magnetization of the two respective sublattices are equal and opposite. This T_{comp} has proven to be a useful tool for realizing electrical, and temperature controlled memory/logic

devices[28], through measurement of the AHE. TM-RE ferrimagnetic materials that display PMA and have a T_{comp} close to room temperature are therefore practical materials to employ in spintronic and magnetotransport devices. TM-RE FIM materials have been shown to be particularly sensitive to growth conditions, and therefore having great variability in resulting composition and magnetic properties. These materials can also have variability of their properties post growth due to dynamic processes such as oxidation, or through annealing when in proximity of other oxide materials. The migration of ions into the FIM lattice is known to affect the magnetic properties dramatically, and when done intentionally, can cause up to 200 K shifts in T_{comp}[57]. By having an electrical means to shift T_{comp}, devices that operate on the same concept as shown in the previous chapter become more readily applicable in spintronics. There still remains open questions regarding TM-RE ferrimagnets. Although there has been a recent surge in research regarding these materials, more work needs to be done to understand the magnetic properties, and how they can be effectively tuned. In this report, the AHE and magnetometry measurements of FIM bilayer samples of Co/Gd are explored due to the ease of growth. Because alloy samples have to be co-deposited, bilayer samples are an easy way to achieve synthetic ferrimagnets, and still have elusive properties in literature. Thicknesses of the Co/Gd layers are chosen based on the previous measurements that were used to show the temperature driven memory. Along the bilayer sample results, measurements of the AHE and magnetometry are presented for alloy samples as well. Methods to search for the T_{comp} of these samples are applied in order to optimize the composition, or bilayer thickness, so that these same materials can be implemented in nonlocal spin valve devices.

4.2. FERRIMAGNET BILAYER MATERIAL GROWTH AND METHODS

Bilayer samples were DC (RF) sputtered for Co (Gd) at a base pressure of 4 x 10^{-7} torr. A total of 5 bilayer samples were grown, all on SiO_2 coated Si wafer, then

cleaved to size for measurements. A 3 nm Ta seed layer is used, then the bilayer is sandwiched between 3 nm Pt. The bottom Pt layer promotes PMA as a result of SOC at the interface, and acts as a protection from oxidation on top. The samples stacks are denoted as 3Ta/3Pt/xCo/yGd/3Pt with the coefficient corresponding to the thickness of the layer in nm, and will be referred to as such in the following measurements. The thicknesses of the selected bilayer were selected using the previous chapter's results as a guide, so that PMA may be obtained through an AF coupled Co and Gd layer. Since the growths of TM-RE FIMs are sensitive to growth conditions, all conditions were kept the same. One important note is that since this is a synthetic FIM as a result of a bilayer deposition, there is going to be a region of diffusion between the Co and Gd layers, which may differ from sample to sample, along with the magnetic domains that develop. Figure 4.1a shows a cross view schematic of the total sample stack, with arrows indicating the direction of magnetization for each bilayer and how they would contribute to the M_{net}.

To search for the T_{comp} of each sample, the AHE was measured using the Van Der Pauw method to obtain H_c vs. T similar to the previous chapter so a divergence in H_c could be identified as an approach to the T_{comp}. Figure 4.1b shows a top view schematic of the Van Der Pauw connections to obtain V_{AHE} An ultrasonic wirebonder was used to attach the experiment peripherals to the sample, and then mounted on a gold coated copper mount. The sample mount is radiation shielded and placed into a vacuum cryostat that can be cooled using LN2. A Keithley 6221 and Keithley 2182 source-meter delta mode function was used with a 250 μA I_{bias} and a delay parameter of 2 ms to get a measurement of V_{AHE}. This allows computer control of measurements and temperature regulation to avoid thermal drift. Perpendicular magnetic anisotropy of the samples was confirmed through the squareness of the AHE when mounted in the perpendicular direction.

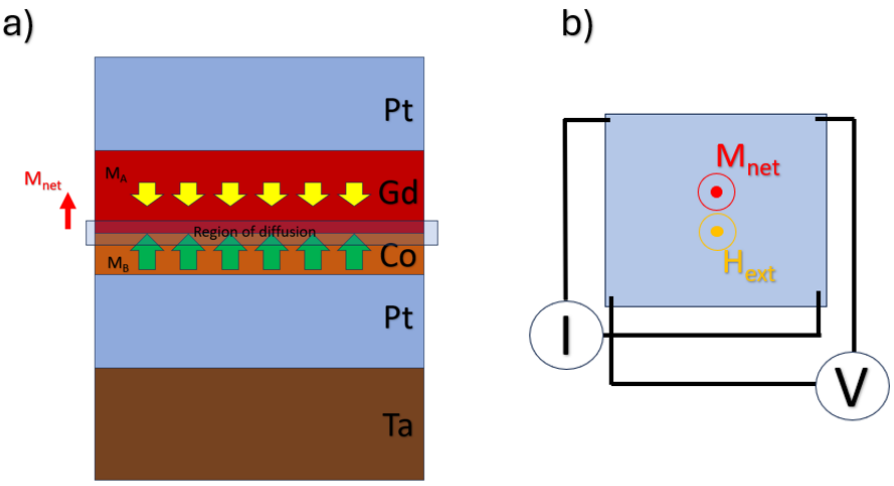

Figure 4.1: Schematic views of the heterostructure grown to aheive a synthetic bilayer FIM. **a)** shows a cross sectional view, with the Pt and Ta having thicknesses of 3 nm and the Co and Gd layers varying in thickness. The direction of M_{net} is displayed as a sum of M_A and M_B which are the depictions of the magnetization of each layer. **b** shows a top view of the same device, with current and voltage leads attached in accordance with the Van Der Pauw method so that the AHE can be measured. The M_{net} and H_{ext} are in the same direction and perpendicular to the plane of the film.

SQUID magnetometry was then performed on the samples expected to have measurable T_{comp} in the perpendicular orientation to compare with AHE measurements. Samples were mounted in an out-of-plane direction to align the external field H_{ext} to the magnetization M of the sample. If the sample indeed displays PMA, then the out-of-plane mounting method should return results associated with the FIM easy axis. Hysteresis measurements were taken with a maximum field applied of $\pm$ 2000 Oe, and taken at temperatures ranging from 10 K to 300 K. H_c and M_S were then recorded as a function of temperature to more easily identify a T_{comp}. Magnetization vs. temperature curves of these samples are not so easily interpreted to extract a T_{comp} as the paramagnetic contributions from the rest of the stack can have a temperature dependence that's not so easily subtracted, having the total magnetization of the entire stack not exactly equal to zero at the observed T_{comp}. Still, M vs. T was measured from 10 K to 310 K, after zero field cooling (ZFC) and then again from 10

K to 310 K after field cooling (FC) the sample. The ZFC/FC measurements are all taken in a warming phase, and the FC field is only applied after the ZFC measurement has taken place. Since the Curie temperature T_c of bulk Co is 1388 K, it is impossible to induce full paramagnetization in the sample by warming to this temperature. Therefore, the temperature chosen to begin the warming periods was 310 K, ensuring it was well over the Gd T_c of 292 K in bulk. In the ZFC step, the sample is cooled from 310 K to 10 K at a rate of 10 K/min, then once stabilized, a measurement of the moment was taken using the dipole fit method built into the SQUID magnetometer at steps of 2 K up to 310 K, with a measuring field H_{ext} = 100 Oe. To begin the FC process, at 310 K, the chosen FC value is applied, and in this case can take on the value of 100, 200, 400, 800, or 1600 Oe, indicated in the displayed results, and then cooled to 10 K at a rate of 10 K/min. The moment is again measured in the warming phase at 2 K steps, with an applied measuring field H_{ext} = 100 Oe. The results of the ZFC/FC magnetization curves can be useful to understanding how the magnetization of the sample as a whole is related to temperature, and how it may differ from the results of the AHE, since the AHE is a probe of the 3d electrons only.

4.3. AHE IN FERRIMAGNET BILAYER

For two samples, 0.5Co/1.8Gd and 0.6Co/1.8Gd, Figure 4.2 displays the V_{AHE} vs. H_{ext} with a maximum applied field of 1500 Oe, and the calculated coercivities H_c vs. T. Although hysteresis loops of the AHE were taken from 80 K to 300 K, Figure 4.2 displays a selected 4 temperatures to display the PMA exhibited by both samples, and the limitations of the LN2 cryostat magnet.

Since the maximum allowed applied magnetic field is 1500 Oe, when the $H_c >$ 1500 Oe, the AHE measurement will not show switching. In Figure 4.2c, the H_c increases as the temperature is lowered, but no H_c can be resolved for any temperatures below 120 K for these samples. This means that for the AHE hysteresis loops at 80, 100 and 120 K, $H_c >$ 1500 Oe and exceeds the limits of the LN2 cryostat. This curve

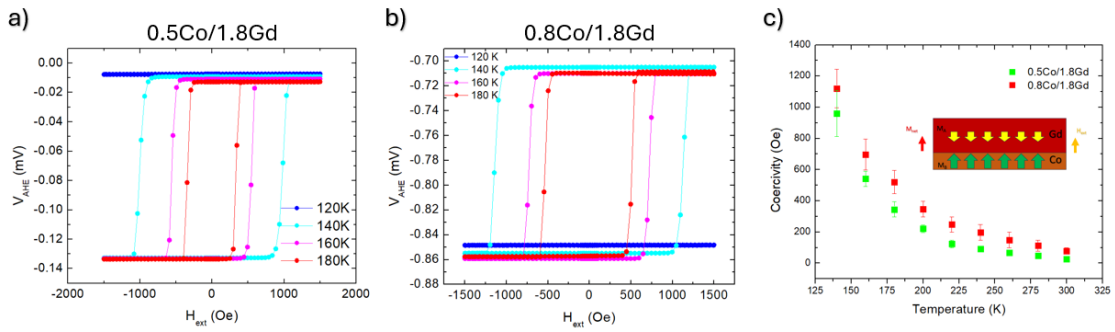

Figure 4.2: V_{AHE} vs. H_{ext} measurements for two bilayer samples that exhibit PMA as indicated by the square hystersis loops **a)** AHE measurements for 0.5Co/1.8Gd **b)** 0.8Co/1.8Gd **c)** The calculated H_c vs. T from the AHE hysteresis loops showing an increase as T is lowered, and no discernible T_{comp} is observed. *Inset:* Cross sectional view of Co/Gd bilayer stack with directions of M_{net} and H_{ext} shown.

is also a indication that the T_{comp} for these samples must be below 140 K, given that it can be assumed to have a diverging behavior as T is lowered. Figure 4.3 plots the normalized AHE hysteresis loops for more bilayer FIM samples, with an effort to confirm PMA and search for a T_{comp}. Down to 78 K, for any of the bilayer samples, no T_{comp} was observed within the constraints of the measurement setup. All H_c vs. T relationships do show an increase as temperature is lowered. This is expected for the 0.5Co FM sample as the ability for the Co moments to maintain parallel alignment is greater at lower temperatures since there is less thermal influence. The obvious non square loops in Figure 4.3d display a mixed anisotropy for the sample. In an AHE measurement along the easy axis of the FIM, the hysteresis should be square. If H_{ext} is then oriented perpendicular to the M_{net}, a linear behavior of V_{AHE} vs. H_{ext} is to be expected. The results for 2Co/1Gd is a result of the sample having a more complicated magnetic landscape, with competing directions for M in-plane and out-of-plane. This can be explained through the fact that this is the sample with the greatest thickness in Co, and it has been observed that Co can lose its uniaxial PMA above a threshold thickness of ~ 0.8 nm. Because of this known fact, it is assumed that the addition of Pt in the stack can help Co keep it's PMA even when it's above the 0.8 nm threshold. Another explanation for the PMA in the 1Co/1Gd sample is

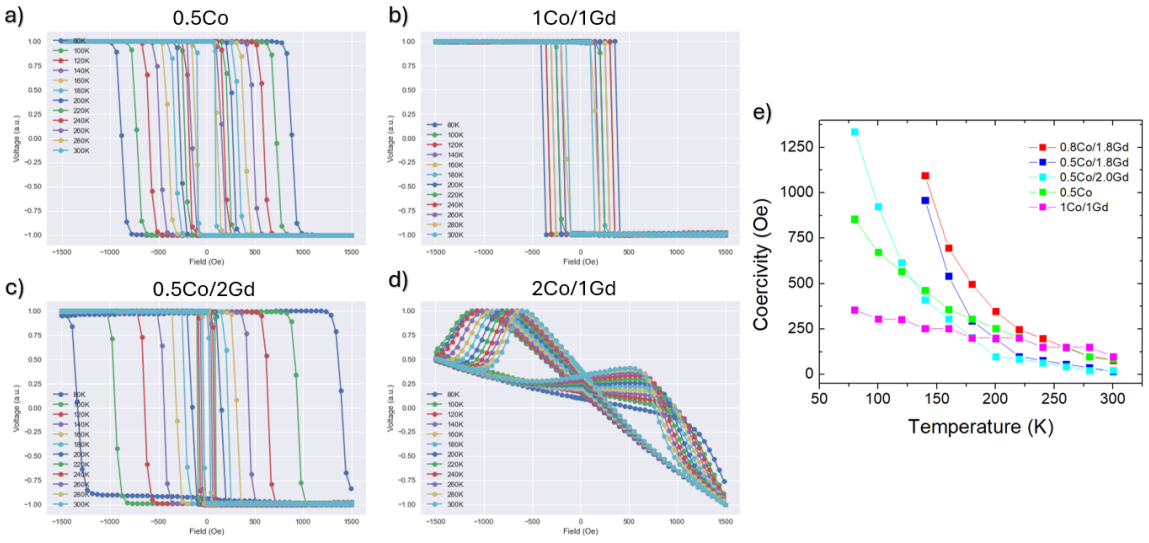

Figure 4.3: Normalized V_{AHE} vs. H_{ext} for various bilayer samples and H_c vs. T showing growing coercivity as temperature is decreased. All hysteresis loops are plotted to show which samples display PMA through a square hysteresis loop and the sample with 2Co/1Gd showing mixed anisotropy. From 80 K to 300 K, hysteresis loops narrow, which can be further visualized in the H_c plot **a)** AHE for 0.5Co **b)** 1Co1Gd **c)** 0.5Co/2Gd **d)** 2Co/1Gd. **e)** All samples H_c vs. T showing that coercivity grows as temperature decreases for every sample. No T_{comp} is observed from these measurements.

that both Co and Gd are typically HCP lattice structures, which, in the case for Gd, promotes strong uniaxial anisotropy, although in a polycrystalline film, it is not so easily explained through this mechanism. For the FIM samples, it can be assumed that divergent behavior of the H_c as the temperature is lowered is a direct sign that, if there exists a T_{comp} for any of these samples, it would be below the coldest temperature a H_c was able to be extracted, beyond the limits of the LN2 cryostat for all samples measured. It is possible for the 0.5Co/1.8Gd and 0.8Co/1.8Gd to have a T_{comp} between 78 K and 140 K, since the AHE hysteresis is not fully captured due to the maximum field allowed by the magnet. It will be shown in later AHE and SQUID magnetometry measurements that this is the case. As seen in the previous chapters, there needs to be a decay of H_c away from T_{comp}, and a flip in the polarity of the AHE hysteresis measurement to confirm a T_{comp}. It is therefore necessary to explore lower temperatures and higher magnetic fields to meet these conditions.

4.3.1. LOW TEMPERATURE AHE MEASUREMENTS USING SC MAGNET

To further explore the FIM bilayer Co/Gd samples, a superconducting (SC) magnet cryostat was employed to reach temperatures as low as 2 K and fields as high as 7 T. This was the first time the SC magnet was operated, giving rise to many non-optimal situations that reflect in some of the data. Nonetheless, confirmation of T_{comp} could still be achieved through the H_c vs. T curve. The instrument is a LHe cooled NbSn superconducting magnet with a critical temperature $T_{crit} \sim 10$ K. The SC magnet is encased in a 55 L dewar that is vacuum shielded from the room temperature, and filled with the recycled LHe from the Zink Lab. The sample mount is He vapor cooled, and connected to an SRS Sim900 through cryowire to have a 4 wire probe. The SRS Sim900 uses a voltage bias to inject a current, and returns a resistance measured by the voltage taps. The conversion to resistance is done by the Sim900 and therefore all hysteresis measurements for the SC magnet are displayed as R_{AHE} vs. H_{ext} Figure 4.4 displays R_{AHE} vs. H_{ext} for the temperatures at which AHE measurements were successful in the 0.5Co/1.8Gd bilayer, with a polarity switch

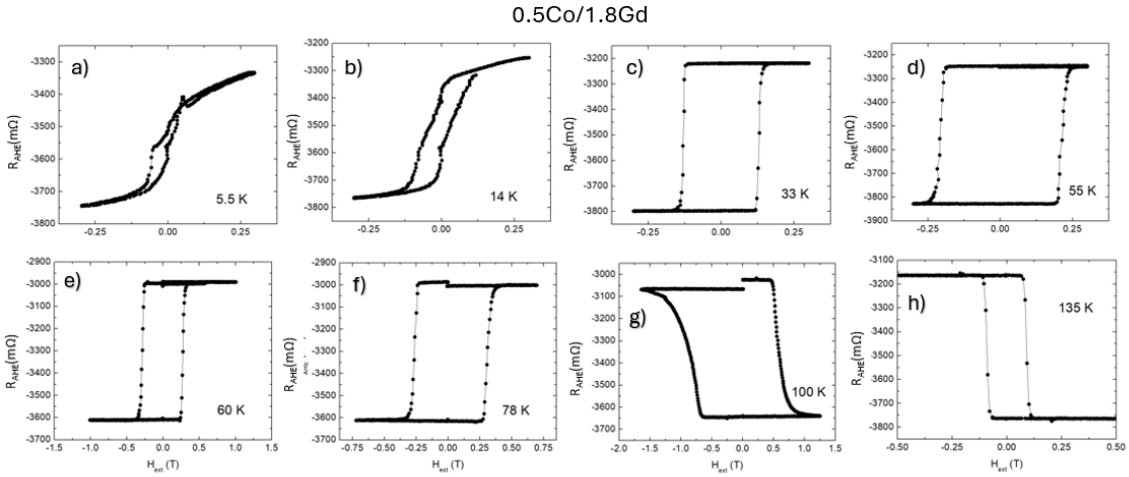

Figure 4.4: R_{AHE} vs. H_{ext} for 0.5Co/1.8Gd in the superconducting magnetic cryostat at temperatures indicated within the plots. **a) and b)** Show a loss of perpendicular magnetic anisotropy. **c)-f)** Show square loops below T_{comp} indicated by opposite polarity of AHE loops compared to **g) and h)** AHE loops above T_{comp} with the coercivity in **g)** reaching the highest value of $H_c = 8419.8$ Oe ± 2000 Oe

observed. At the 5.5 K and 14 K temperatures, the hysteresis loops lose their square characteristic. At 33 K and above, the squareness of the AHE hysteresis loop returns, with the ability to extract H_c. The loops at 5.5 K and 14 K indicate that there is shift in PMA. Because the loops are not completely square, and have a y-intercept much lower than the saturation value, it can be assumed that the direction of magnetization is not perfectly aligned out-of-plane below 33 K, a phenomena further explored in a future section. The loops at 78 K and 100 K show that a stable temperature was not reached, therefore having misaligned data, and a skewed H_c value. Nonetheless, these are the two temperatures at which the polarity switch is observed.

When examining the loops more closely to obtain coercivity values, it is seen that at 100 K, $H_c = 8419.8$ Oe ± 2000 Oe, the highest recorded H_c for the 0.5Co1.8Gd sample. This is a direct result of the diverging H_c behavior close to T_{comp}. A plot of the coercivities in the LN2 cryostat measurements as well as the SC Magnet cryostat measurements are plotted in Figure 4.5. The H_c vs. T shows a clear divergence around T_{comp}, which is in between 100 K and 78 K. Even though the temperature

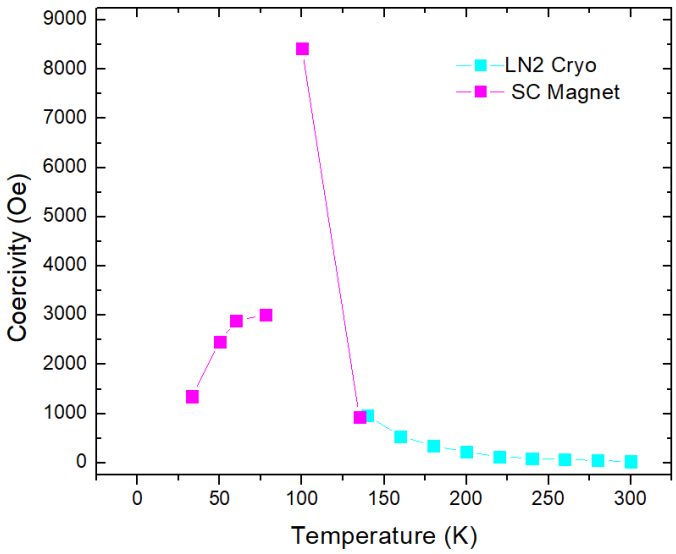

Figure 4.5: H_c vs. T for 0.5Co/1.8Gd from both, the LN2 cryostat and the SC magnet cryostat. The relationship shows a divergence as T approaches T_{comp}, which lies in between 100 K and 78 K.

regulation increased error of the coercivity values obtained, the confirmation of a T_{comp} can be sufficiently justified by the H_c divergence, and the switching of polarity in the AHE hysteresis loops.

The same approach was taken for the sample with 0.8Co/1.8Gd. Figure 4.6 displays the correspoding AHE hysteresis loops measured in the SC magnet for this sample. In this sample, more accurate temperature regulation was achieved as the kinks to stabilizing the sample temperature was sorted from the previous measurements. As a result, the AHE loops have clear saturation points and clear switching events. It is observed that below 30 K for this sample, PMA is lost, similar to the previous sample, and is deduced by the lack of squareness in the AHE loops. Above 30 K all the loops have a square characteristic to them, confirming the presence of PMA. Now that lower temperatures and higher fields can be reached, the maximum H_c measured for this 0.8Co/1.8Gd sample is $H_c = 9473$ Oe ± 1064.5 Oe. The polarity switch of the AHE loops was observed to be between 60 K and 90 K with the AHE

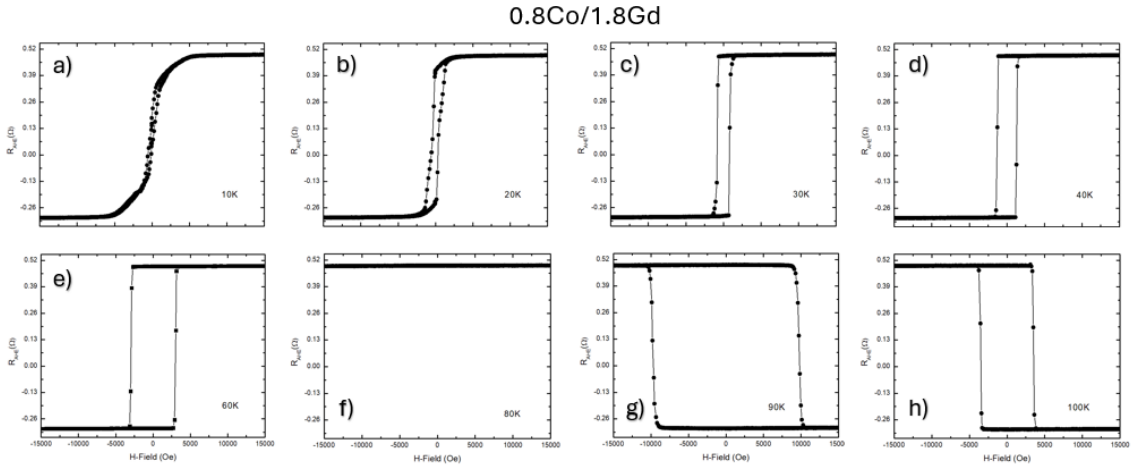

Figure 4.6: R_{AHE} vs. H_{ext} for 0.8Co/1.8Gd in the superconducting magnetic cryostat at temperatures indicated within the plots. **a) and b)** Show a loss of perpendicular magnetic anisotropy. **c)-e)** Show square loops below T_{comp} indicated by opposite polarity of AHE loops compared to **g) and h)** AHE loops above T_{comp} with the coercivity in **g)** reaching the highest value of $H_c = 9473$ Oe ± 1064.5 Oe

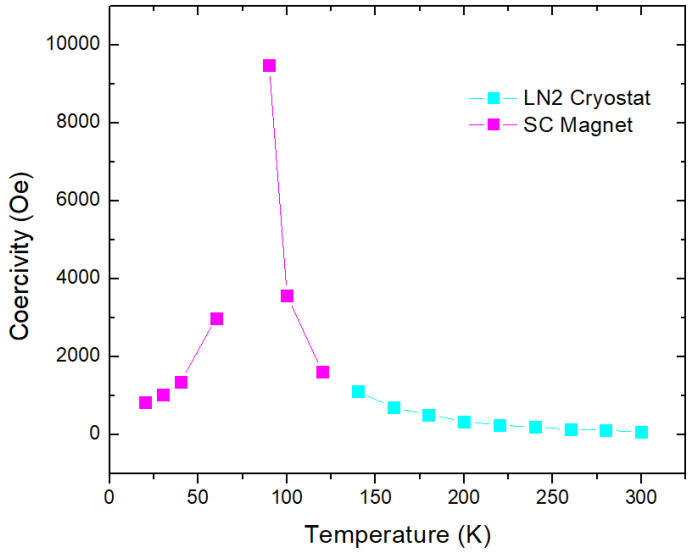

Figure 4.7: H_c vs. T for 0.8Co/1.8Gd from both, the LN2 cryostat and the SC magnet cryostat. The relationship shows a divergence as T approaches T_{comp}, which lies in between 90 K and 60 K.

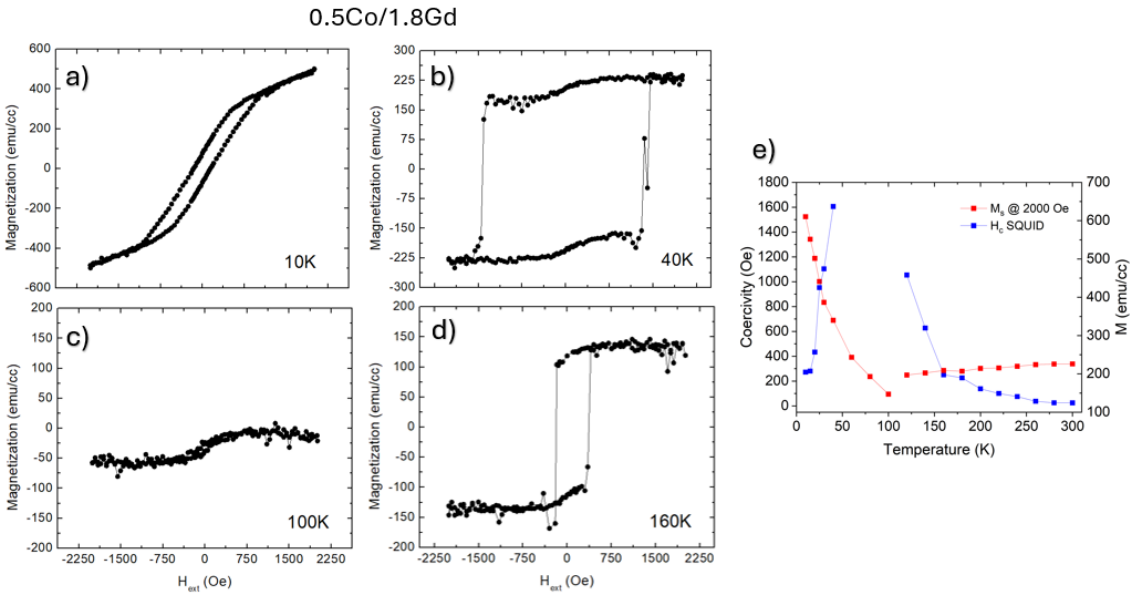

Figure 4.8: M vs. H_{ext} in out-of-plane orientation for 0.5Co/1.8Gd at temperatures **a)** 10 K, **b)** 40 K, **c)** 100 K and **d)** 160 K **e)** A plot of H_c (left axis) and M_s (right axis) vs. T. A divergence in H_c is realized in SQUID measurements and a plot of $M(T)$ shows expected outcomes of reaching a minimum before switching to opposite state.

loop at 80 K having a $H_c > 1.5$ T, the maximum applied field in the loops shown. A plot of the calculated H_c is shown in Figure 4.7 to display the divergence approaching T_{comp}. Due to LHe resource limitations and time constraints, not all bilayer samples were fortunate enough to be measured in the SC magnet cryostat. Focusing on the same two samples, SQUID magnetometry measurements will be displayed.

4.4. SQUID MAGNETOMETRY OF FERRIMAGNET BILAYER

The results for SQUID magnetometry of these two samples are presented in this section, along with the 0.5Co sample as a reference. From the previous AHE measurements, T_{comp} for 0.5Co/1.8Gd is estimated to be 85 K and 80 K for 0.8Co/1.8Gd, therefore SQUID magnetometry should display similar characteristics such as diverging H_c around T_{comp} and because T_{comp} corresponds to a $M_{net} = 0$ measurements at T_{comp} should reflect this. Again, because there are paramagnetic contributions from the heterostructure, care needs to be taken when interpreting the data, yet measure-

ments are performed along the easy axis of PMA, so that a direct comparison of the H_c can be compared to that of the AHE measurements. Mounted in the out-of-plane direction, the hysteresis loops for M vs. H can be seen in Figure 4.8a-d for 0.5Co/1.8Gd along with the calculated coercivities and saturation magnetizations from the hysteresis loops in Figure 4.8e. Two temperatures below T_{comp} and two temperatures above are plotted for visualization, but the hysteresis loops were conducted at multiple temperatures. The M vs. H curves in 0.5Co/1.8Gd depict easy axis behavior in the out-of-plane direction, yet at 10 K there is an obvious change in anisotropy. The linear, paramagnetic phase in the saturated region of the diagram along with a narrower coercivity indicate a shift from PMA to in plane magnetic anisotropy (IMA). Since the measurements begin at 10 K and then are measured after periods of warming, it can be observed that the PMA is restored, and not lost when the material is cooled to 10 K for long periods of time. The squareness of the hysteresis doesn't return until 40 K, where the easy axis PMA is easily identified. At 100 K, above T_{comp} and in a region of extremely high H_c, the 2000 Oe maximum field is not enough to flip the magnetic moments back positively. Since the previously saturated state was locked in below the T_{comp}, even though there is not enough of an H_{ext} to saturate the material, the net magnetic moment is negative, consistent with the M_{net} undergoing a flip due to warming above the T_{comp}. Upon a closer look of the M vs. H at 100 K, even though there is no switching happening because of high coercivity of 8419.8 Oe, there is a minor "S" shaped hysteresis loop that we will refer to as a "soft component" in the M vs. H. This soft component is also present in the 40 K M vs. H curve, with a change in up to 30%, and doesn't seem to be reflected in the AHE hysteresis measurements. In Figure 4.8e, the H_c vs. T (left axis) is plotted alongside M_S vs. T (right axis) to show diverging H_c around $T_{comp} \simeq 85$ K. From these measurements, the low temperature change in magnetic anisotropy is consistent for the magnetometry and for the AHE measurements, but the soft component present at higher temperatures is not.

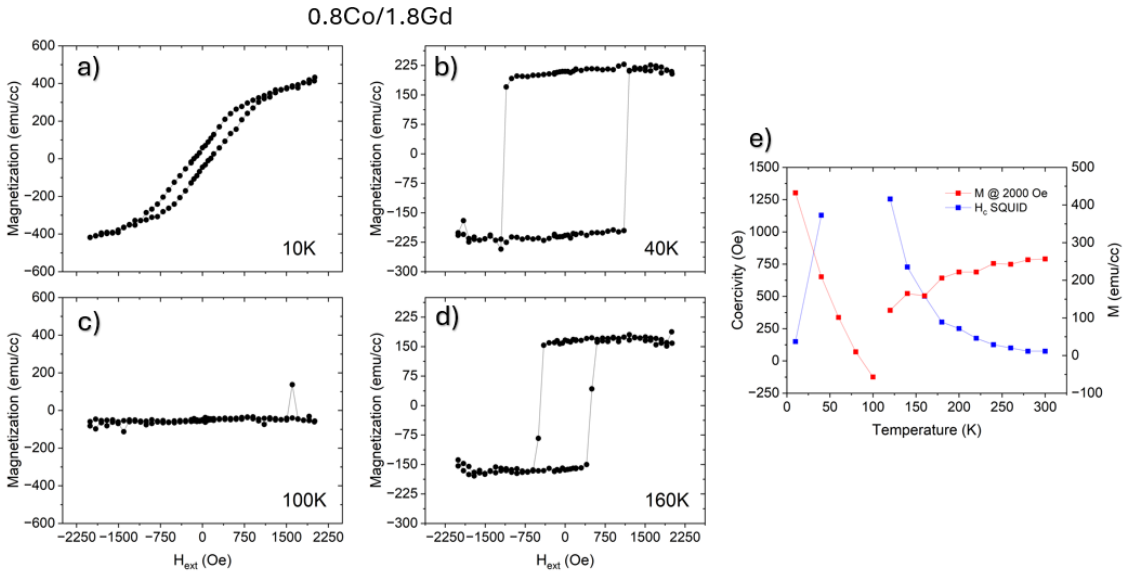

Figure 4.9: M vs. H_{ext} in out-of-plane orientation for 0.8Co/1.8Gd at temperatures **a)** 10 K, **b)** 40 K, **c)** 100 K and **d)** 160 K **e)** A plot of H_c (left axis) and M_s (right axis) vs. T. A divergence in H_c is realized in SQUID measurements and a plot of $M(T)$ shows expected outcomes of reaching a minimum before switching to opposite state.

Looking at Figure 4.9 for the 0.8Co/1.8Gd sample, a similar picture is painted. At lower temperatures the same change in PMA is observed, except there is less of a soft component contribution to the M vs. H hysteresis loops. Taking a closer look at the 100 K curve, the soft component is almost completely absent. Because the coercivity of this sample at 100 K = 9473 Oe according to the AHE measurements, the field from the M vs. H measurement is not enough to initiate switching of the state. Similar to the 0.5Co/1.8Gd sample, at 100 K the magnetic moment measured is also negative, even though it was last locked in a positively saturated state. This is confirmation that this sample has crossed it's T_{comp} and undergone change in direction of M_{net}. This is something that is not observed in the AHE measurement, since the sublattice magnetization of the 3d electrons remains in the same direction. The difference is that above T_{comp}, the Co magnetic sublattice is greater than that of Gd's, so even though the M_{net} has reversed, the magnetized 3d electrons have not.

Since the soft component is practically nonexistent in the 0.8Co/1.8Gd sample, it is easier to observe the T_{comp} as 80 K when the saturated moment crosses 0, in alignment with the AHE measurements. It is harder to realize in the M_s vs. T curve for 0.5Co/1.8Gd since the large contribution from the soft component offsets the M_{net} by some amount. This is also a prevalent feature in the M vs. T curves that were measured after a period of zero field cooling (ZFC) and field cooling (FC) which can be seen in Figure 4.10. Figure 4.10a-b show two different M vs. T measurement methods for 0.5Co/1.8Gd and Figure 4.10c-d show the same for 0.8Co/1.8Gd. The ZFC FC periods for each graph are as follows. On the left hand side, the two graphs for each sample are always measured at 800 Oe. The sample starts off at 310 K, then is cooled to 10 K. At 10 K, a field of 800 Oe is applied, and then measured as a function of T while warming back to 310 K. At 310 K, the sample is then cooled back to 10 K in the same 800 Oe field, causing it to FC, and then measured in the same manner from 10 K to 310 K. The purpose of this was to eliminate large ZFC-FC splitting as a result of the high coercivity region. On the right hand side graphs of Figure 4.10, this large ZFC-FC splitting is due to this reason. In these plots, the sample is first ZFC to 10 K, then measured from 10 K to 310 K with a field of 100 Oe applied. This gives dramatically different results, as at 10 K 100 Oe is not sufficient to completely saturate either samples. Once the sample is at 310 K, the FC field is applied, 800 Oe, and the sample is then cooled back to 10 K. At 10 K, the field is changed to 100 Oe to measure the warming period from 10 K to 310 K once more. The large splitting shown in the right hand M vs. T curves is due to the FC curve saturating the opposite state of the FIM than of the ZFC case. As the temperature is warmed, the red curves for b) and d) indicate the temperature dependence when M_{net} is oppositely oriented to that of the ZFC blue curves. The magnetic state will not switch until it's H_c above T_{comp} is < 100. Typically, ZFC FC splitting is an indication of a frustrated magnetic landscape, or a glassy magnetic state, but here, it is not to be interpreted in that sense. The left hand side a) and c) graphs of M vs. T tell a

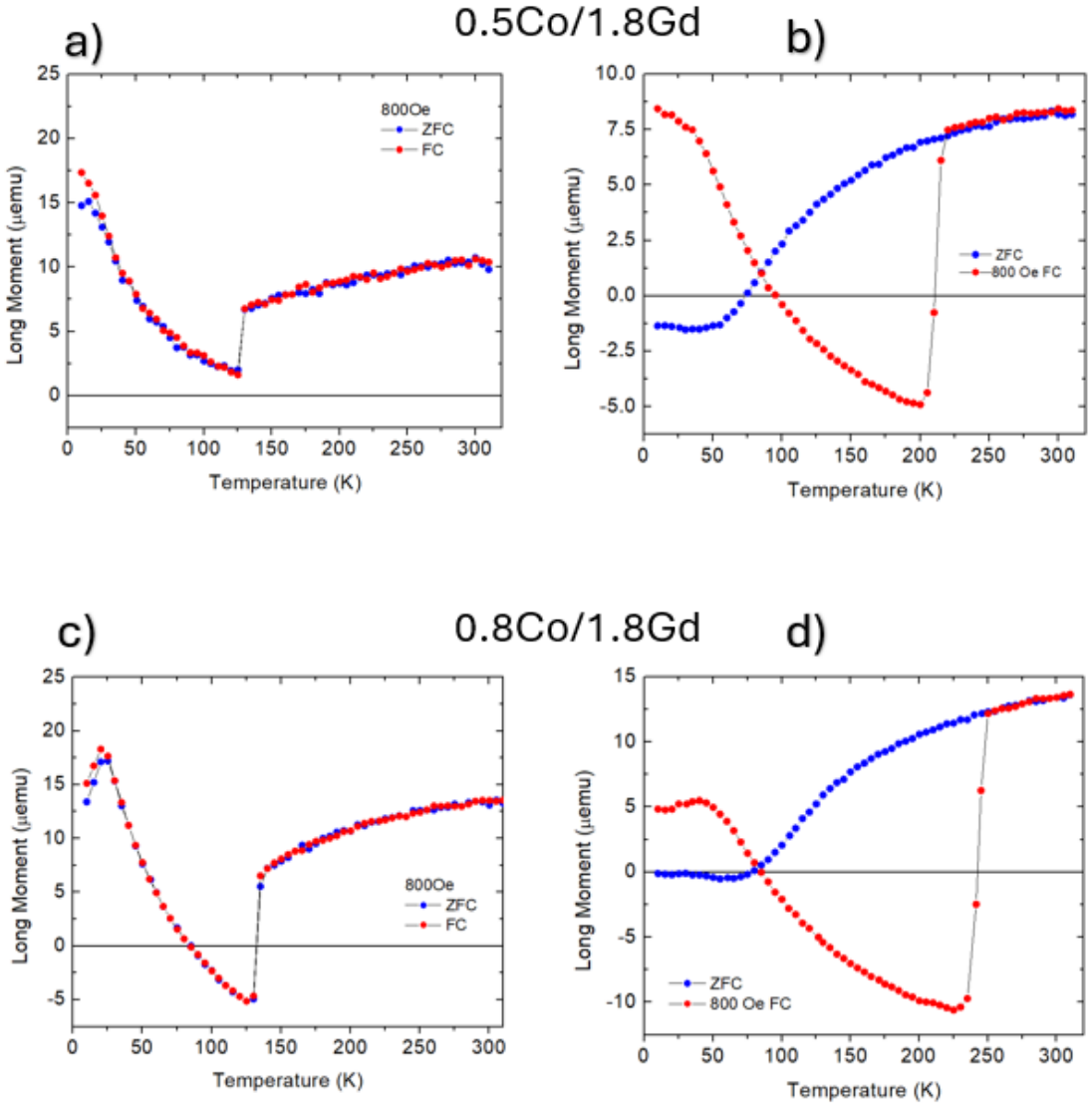

Figure 4.10: ZFC/FC M vs. T measurement curves for the two FIM samples using two different methods. **a** The M vs. T for 0.5Co/1.8Gd when measured in a 800 Oe field. **b** M vs. T for 0.5Co/1.8Gd when measured in a 100 Oe field. **c** M vs. T for 0.8Co/1.8Gd when measured in a 800 Oe field. **d** M vs. T for 0.8Co/1.8Gd when measured in a 100 Oe field. The different methods of measurement can help understand the materials' magnetic landscape by the low temperature ZFC/FC splitting in **a) and c)** and the crossing through T_{comp} in the ZFC curves when measured in 100 Oe.

slightly different story. When the FIM is measured at 800 Oe always, the ZFC FC curves show an interesting low temperature feature. The splitting of the ZFC and FC curve at these temperatures is not a result of the M_{net} switching states like in the other method, but rather as a result of the observed change in PMA in the AHE and SQUID hysteresis measurements. The ZFC curves for both samples measured at 800 Oe show a cusp in the M vs. T curve which usually corresponds to a magnetic phase transition. Below the cusp, the splitting between ZFC/FC curves is in alignment with a frustrated magnetic system. In the case for this bilayer ferrimagnet, it's a direct indication of the competing axes of magnetization, here the IMA and PMA, as confirmed from the AHE and SQUID measurements independently. Although the change in magnetic anisotropy is easily visualized in this section, the following section will show the calculations of the magnetic anisotropy energy, measured by the SQUID.

4.5. LOW TEMPERATURE CHANGE IN MAGNETIC ANISOTROPY OF FERRIMAGNET BILAYER Co/Gd

To obtain magnetic anisotropy energies of certain sample directions, we use the generalization of the relationship for M and H as

$$\mu_a = -\mu_0 M \cdot H, \tag{4.1}$$

where μ_a is the anisotropy energy density μ_0 the permeability of free space, and M and H correspond to magnetization and external applied field respectively. First, M vs. H hysteresis curves must be obtained for the in plane (IP) and out of plane (OOP) direction. For the two samples 0.5Co/1.8Gd and 0.8Co/1.8Gd, hysteresis loops up to 3 T were conducted in the SQUID to ensure full magnetic saturation along both axes of measurement. An example of these hysteresis curves is displayed in Figure 4.11 for 0.5Co/1.8Gd. Because the shift in magnetic anisotropy was observed below 40 K, M vs. H was measured at 10, 20 and 40 K as depicted by Figure 4.11a,

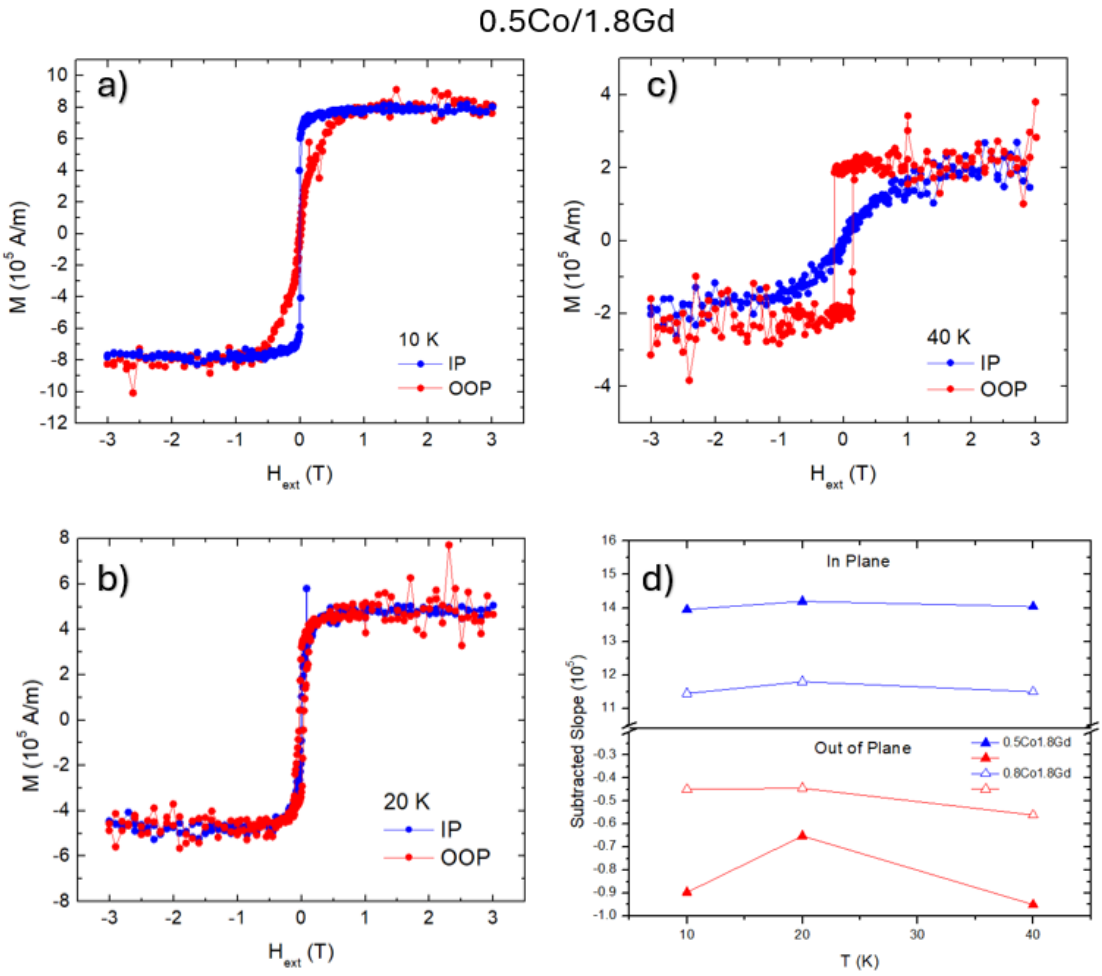

Figure 4.11: **a)-c)** M vs/ H for three different temperatures for 0.5Co/1.8Gd. Between 10 K and 40 K, the IP and OOP hysteresis curves can be shown to switch easy axis directions from OOP at 40 K to IP at 10 K. at 20 K, the curves are almost on top of each other showing the sample's mixed anisotropy, since an easy axis cannot be easily identified. **d)** The subtracted background values from the hysteresis curves before plotting. Paramagnetic contributions persist for the IP direction while diamagnetic contributions for OOP

4.11b and 4.11c respectively. The curves in 4.11 had paramagnetic (diamagnetic) contributions that needed to be subtracted from the IP (OOP) directions to obtain a flat M_s region, and the subtracted values can be seen in Figure 4.11d. For the IP direction, a paramagnetic background was subtracted for each temperature that was larger in the 0.5Co/1.8Gd sample than the 0.8Co/1.8Gd sample. For the OOP direction, a diamagnetic background background was subtracted for each temperature that was also larger in the 0.5Co/1.8Gd sample than the 0.8Co/1.8Gd sample, as indicated in Figure 4.11d. Once a subtracted hysteresis curve is obtained, using the relation from equation 4.1, magnetic anisotropy energies can be calculated for each M vs. H. By altering Equation 4.1 we can obtain expressions for the anistropy energy in the IP and OOP directions labeled as K_{IP} and K_{OOP} and are written as follows.

$$K_{IP} = \int_0^{M_S} H(M)\, dM \tag{4.2}$$

$$K_{OOP} = \int_0^{M_S} H(M)\, dM \tag{4.3}$$

From these two expressions we can obtain an effective uniaxial anisotropy energy of the material written as

$$K_u^{eff} = K_{IP} - K_{OOP}, \tag{4.4}$$

which will tell us that the OOP direction is preferred when $K_u^{eff} > 0$ and visa versa. To perform this calculation, additional analysis of the hysteresis curves in Figure 4.11 is required. Using Python, and described in more detail in Appendix, an anisotropic field H_A must be extracted from the M vs. H curve in the hard axis direction. The H_A field is the field required to fully saturate the material in the hard axis direction. To obtain this value, after subtraction of the background in the M vs. H in the hard axis direction, the magnetization values are iterated through to find when the magnetization is within 1% of the saturation value. Not an orthodox way

of calculating H_A, but this should give an accurate value as to when the material has reached saturation within 1%. The H_A calculated is then used to trim the hysteresis curves so that an area under the curve calculation can be obtained from 0 M to M_S for the respective direction. After the area under the curve is calculated for each M vs. H and in all directions, then equation 4.4 can be used to calculate the effective uniaxial anisotropy K_u^{eff}. The results of such calculations are plotted as a function of temperature in Figure 4.12. In Figure 4.12a, the saturation magnetization values are plotted in SI units vs. T, showing an increase as T is lowered, consistent with the M vs. T measurements previously displayed. In Figure 4.12c, the K_u^{eff} calculated values are plotted vs. T. The shift from PMA to IMA is identified in this plot as the $K_u^{eff} < 0$, below 20 K. At 20 K, the anisotropy energies for the OOP and IP direction are almost equal, showing that both directions are as easily magnetized and there is no easy axis. This is the case for both samples. Above 20 K, the $K_u^{eff} > 0$, consistent with results for a sample with OOP easy axis, or PMA. Furthermore, the squareness values, M_R/M_S are plotted in Figure 4.12b as a qualitative depiction of the shift in anisotropy as a result of the proportion of how much magnetization remains in the material when the field is returned to zero, with the calculated M_R values plotted in Figure 4.12d.

Through these calculations, the qualitative understanding of a shift in PMA to IMA at low temperatures from the AHE and original SQUID measurements is quantitatively confirmed. By describing this FIM bilayer system with the mean field approach from chapter 3, the temperature dependence of the anisotropy is not accounted for. Since the easy axis transitions do not contribute to the model, experimentally they can play a big role if PMA is desired at all temperatures. Although there is a shift in PMA, the M_S still increases in this regime of IMA. Ironically, it is shown that high temperature annealing of TM-RE alloys can cause a shift from PMA to IMA, also showing an increase in M_S[72]. Explanations for this are rooted in structural changes of the regularly amorphous TM-RE FIMs to an ordered state, or a

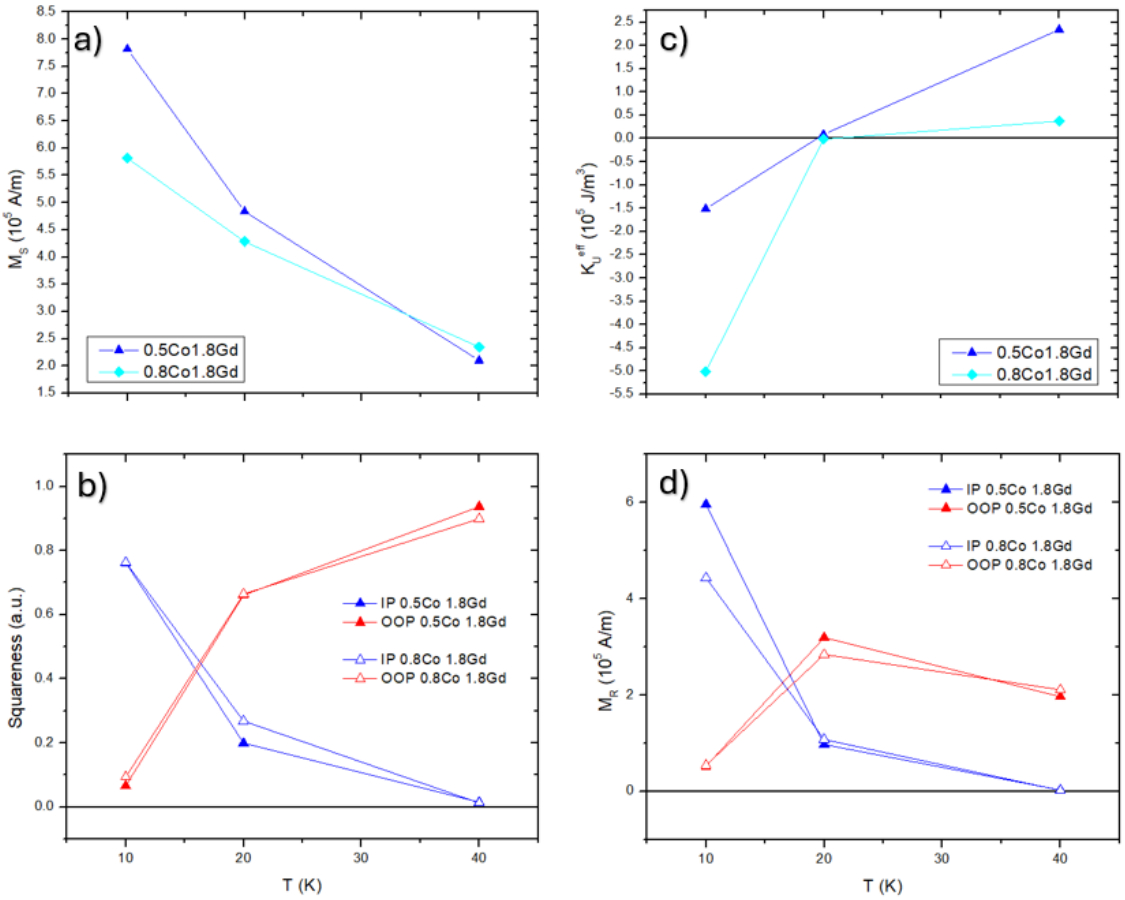

Figure 4.12: **a)** M_S vs. T showing increase during loss of PMA **b)** Squareness calculated as M_R/M_S a simple representation of the material's magnetic retention as a function of T, showing the shift in easy axis from OOP to IP at 10 K. **c)** Calculated K_u^{eff} from Equation 4.4 showing the change in PMA below 20 K as it becomes negative **d)** M_R vs. T to show shift in easy axis through M_R increasing for IP case and decreasing for OOP.

disruption in the local anisotropy pair ordering. The bilayer samples measured would have to undergo a structural phase transition below T_{comp} for the latter to be true, which could only be quantified through XRD measurements. For the disruption of the anisotropic pair-pair correlations to cause this shift in PMA, ion migration must be present within the lattice. Both mechanisms are plausible, but unless more information is obtained from more experiments, the exact reason is not realized through the experiments.

4.6. CONCLUSION

In conclusion, the FIM bilayer samples 0.5Co/1.8Gd and 0.8Co/1.8Gd are shown to have a shift in PMA at low temperatures. The shift in PMA is apparent in all electrical measurements of AHE, as well as magnetometry measurements using a SQUID magnetometer. Through qualitative and quantitative methods, experimental evidence of this switch below 30 K is confirmed as shown in Figure 4.12. With a T_{comp} around 80 K for both samples, this region of anisotropy change happens 50 K below T_{comp}. A significant distance below T_{comp}, the shift in anisotropy should not interfere with any measurements or processes done around T_{comp}. Even then, the PMA is recovered when the sample is warmed above 30 K, indicating that a slight structural change, or a shift in atomic arrangement in the amorphous TM-RE is the likely candidate for the change in PMA. Further characterization of these FIM systems through XRD could offer more insight into this proposed mechanism.

CHAPTER 5:

SPIN TRANSPORT SIGNAL IN Fe/Al NONLOCAL SPIN VALVES

5.1. INTRODUCTION

The non-local spin valve (NLSV) plays an important role in spintronics, because of the ability to separate charge current from pure spin current. Fabricating the devices can be tedious, since they can require 2 or more steps of electron beam lithography (EBL), and are highly sensitive to static discharge. When grown correctly, they are a vital device to the field of spintronics, as spin sensors, logic and memory elements are being developed more rapidly. A NLSV consists of two parallel FM wires, connected transversely by a normal metal channel. The distance between the wires is chosen based on the normal metal's spin diffusion length. For Cu and Al, the spin diffusion length $\lambda_{sf} \simeq 1$ μm and are often chosen as NM channels. With many reports and characterization of FM/NLSV, ferrimagnetic materials are attractive for application in NLSVs, due to the AF coupling between the magnetic sublattices. The AF coupling is known to have higher resonant frequencies than that of FMs, therefore increased spin diffusion dynamics has been observed.

In a NLSV device, a couple different methods of spin injection can be utilized. The first is electrical injection, where a bias current I_{bias} can be passed down the FM_{inj} then shunted away by the channel. This steers the current, out of the device, as seen in Fig 5.1a, and causes a spin population to develop at the FM/NM interface as a polarized current is generated in the FM. This spin population will diffuse into the NM, across the channel and then detected in the second FM_{det}. The second method is to thermally inject a spin current in the NM, as shown in Fig 5.1b, where

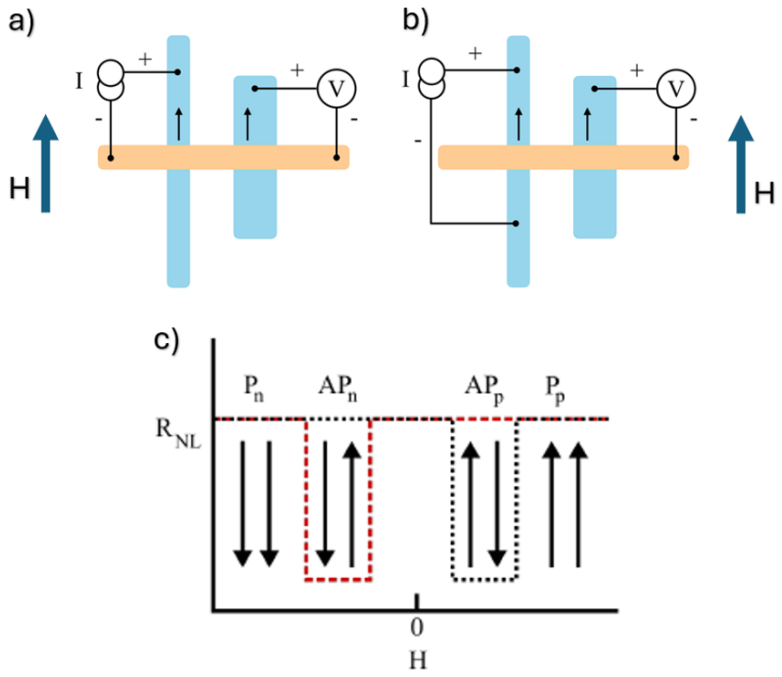

Figure 5.1: Cartoon depiction of NLSV schematic for measuring a nonlocal resistance R_{NL} **a)** shows the NLSV for the case of injecting a spin current electrically. A charge current passes through part of the NM channel but is shunted away, injecting spin through the NM channel electrically **b)** shows the NLSV for when injecting thermally. Current is never passed through NM channel, so that spin diffusion is injected thermally as the junction is heated, creating a thermal gradient in the NM channel and **c)** is an expected R_{NL} vs. H curve for a NLSV when the external field is swept along the axis of the FM wires magnetizations. The depiction of the 4 states for the NLSV measurement shows what happens to the spin signal when the FM wires have opposite magnetizations.

I_{bias} is only passed through the FM, generating a spin population thermally, since no charge is passed through the NM. Similarly, the thermally injected spin current will diffuse into the NM, which can then be detected at F_{det}. To measure a spin signal, the distance between the leads should be less, or on the order of, the spin diffusion length of the NM. The regime at which the device is operating in must be known as well. There is the transparent regime: the contact resistance between the FM/NM is less than the spin resistance, $\mathcal{R}_{FM}$, of the FM. And the tunneling regime: the FM/NM contact resistance is much greater than the spin resistance of the NM channel, $\mathcal{R}_{NM}$, such as an insulating barrier. There are intermediate regimes, that will not be discussed here, but can be referenced in [66]. It's important to note the the spin signal measured in the tunneling regime is expected to be higher than that of the transparent regime. This is because in the transparent regime, the signal has a squared dependence on the ratio of the spin resistance of the FM and NM.

$$\Delta R_{nl} = \frac{4\rho_{FM}^2}{(1-\rho_{FM}^2)^2}\mathcal{R}_{NM}(\frac{\mathcal{R}_{FM}}{\mathcal{R}_{NM}})^2\frac{e^{-L/\lambda_{NM}}}{1-e^{-2L/\lambda_{NM}}}, \tag{5.1}$$

In the tunneling regime the spin signal becomes

$$\Delta R_{nl} = P_J^2\mathcal{R}_{NM}e^{-L\lambda NM}, \tag{5.2}$$

which does not have that same dependence as the transparent regime. Because of this, signals are often much higher in the tunneling regime[66]. The intentional deposition of a tunneling barrier is preferred, with MnO and AlO_x just to name a couple, but sometimes, the ease of fabrication of a transparent contact could be more feasible through etching and/or ion milling techniques before depositing the second layer.

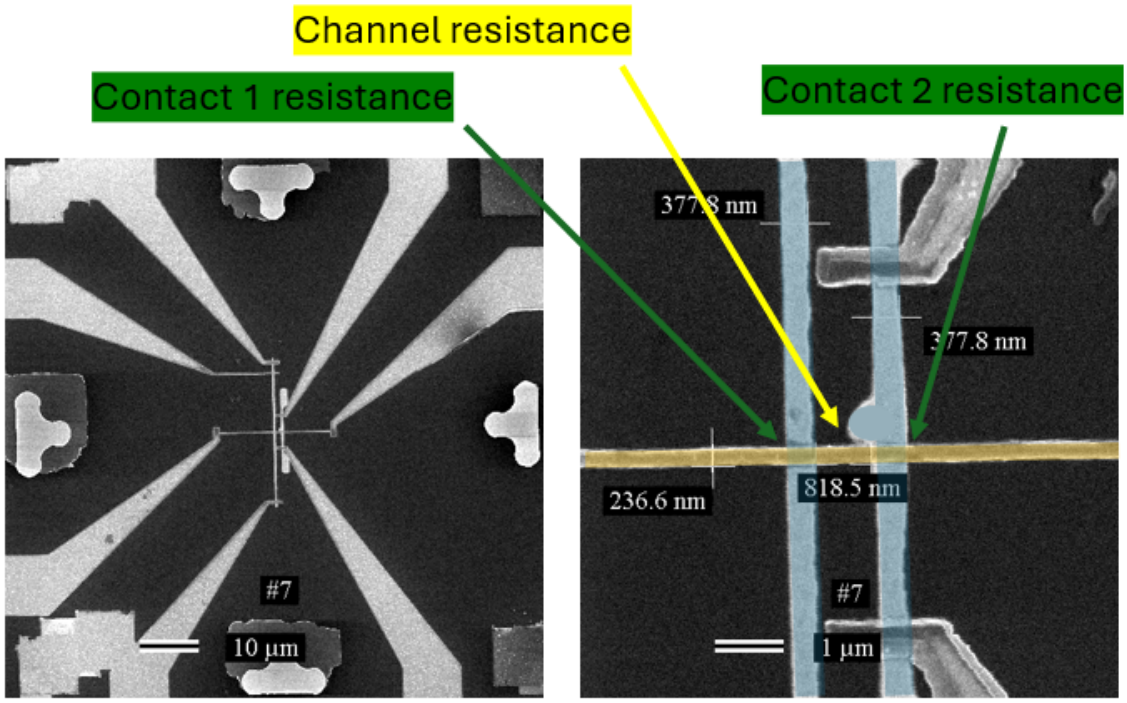

Figure 5.2: SEM images of a NLSV device fabricated in the Zink Lab. The two FM wires are oriented vertically and the NM channel horizontally. The right side FM wire has is designed to have "flags" to ensure a different coercivity, while keeping the width the same at the contact with the NM channel. **a)** Zoomed out view of device showing the leads that connect to the FM wires and the NM channel. **b)** Zoomed in view of the NLSV device with the FM wires colored blue and the NM channel colored yellow. The resistances referred to are the contact resistances, which are resistances measured for the square junctions of the FM/NM contacts, and the channel resistance, which spans the length of the channel between the two FM wires.

5.2. FABRICATION

To grow the NLSVs, a pre fabricated "blank" Si-N chip is prepared at CINT (Center for Integrated Nanotechnologies) located at Los Alamos National Laboratory, which has pre patterned Au leads for a total of 9 possible NLSV devices to be grown. They are pre patterned with alignment markers that are built into the CAD file for the first layer lithography, and have a protective resist on them that should be removed with acetone before proceeding. The first layer lithography aligns to these markers, and exposes the design for the 2 FM wires, along with markers for the second layer to align to. There are three possible separations to create the FM wires: 500 nm, 800 nm and 1100 nm. The chip is first spin coated with PMMA at 2000 rpm for 45 sec, to obtain a single layer electron beam resist, then baked at 180 °C. The first layer lithography program is processed by the nanopattern generation system (NPGS), that controls the FEI Scanning Electron Microscope (SEM). Once the first layer lithography is written, the PMMA must be developed with 3:1 IPA:MIBK for 60 s to remove the exposed pattern. The FM materials are then deposited using an UHV electron beam evaporation deposition chamber. The device here was made with Fe and grown at a base pressure of $\simeq$ 9 x 10^{-9} Torr, grown at a rate of 1 /s for a total of 20 nm. Immediately after, 1 nm of Al is deposited at 0.5 /s to protect the Fe from oxidation, by creating a self limiting oxide of about 1 nm. After growth, the sample is cleaned in acetone to remove the PMMA, then prepped for a second layer lithography. The sample must be spin coated with a 2 layer resist, first CO-MMA, then PMMA using the same 45 s, 2000 rpm program as before. The second layer lithography program is written in the same manner as before, using the same steps to develop. The second layer lithography exposes the pattern that contains the NM channel and the leads that connect the device to the pre patterned Au tracks.

The second layer deposition was done in the Xin Fan's research group AJA sputtering chamber. At a base pressure of $\sim$ 4 x 10^{-7} Torr, the sample is first ion

milled for 30 s. This is to remove the AlO_x layer that formed, but also removing a little bit of the Fe. Immediately after the ion mill, the Al target is ramped up to full power and 100 nm is deposited at 0.8 /s. After deposition, the sample is ready for the resist to be lifted off with acetone and ready for a measurement. Inspection of the liftoff quality with an optical microscope is important to check for shorts, and any breaks in connections.

To connect the experiment peripherals to one of the 9 devices grown, an ultrasonic wirebonder is used to bond 6 connections to the bond pads. First, all leads that will be used are grounded to the copper mount the sample will be mounted to to mitigate failure of the device by static discharge. Once all leads are grounded, the leads can be bonded to the bond pads that the corresponding device will use. The bond pads are made of Au, with an area large enough to bond to, and are then tracked to connect to the leads that the second layer deposition creates. There are connections to each end of each wire. 2 for the FM_{inj}, 2 for the FM_{det} and 2 for the NM channel. With the bonds made, and connection established, the sample mount is connected to the crysotat, with the 6 connections from the NLSV device routed to the 14 pin milspec connection at the top of the cryostat through cryowire. The cryostat is fixed with a grounding box made to keep every connection grounded while installing the sample mount into vacuum mount that houses the cryostat. When the sample is securely in place, the grounding box is then switched to the float option to allow control from the SRS SIM 900 multiplexer. The multiplexer has a total of 7 channels to change the circuit configuration of the 6 connections. The configurations are: Channel 1 Electrical Injection; Channel 2 Thermal injection; Channel 3 Contact resistance FM_{inj}; Channel 4 NM Channel resistance; Channel 5 Electrical injection reversed; Channel 6 Thermal injection reversed; Channel 7 Contact resistance FM_{det}. The contact resistances are for measurements of the resistance of each FM/NM junction, while the channel resistance is a measurement of the Al, NM channel. Each of the configurations can be measured using the LabView VI DifferentialConductance

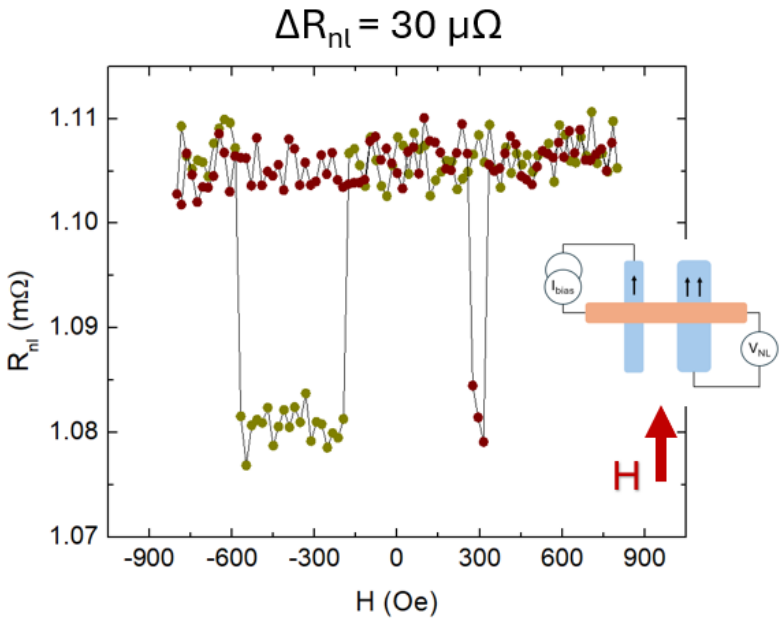

Figure 5.3: Nonlocal resistance plotted versus external field for electrical injection configuration. Field is applied along same axis as FM wires, and is swept from 800 Oe to -800 Oe and back. Resistance plotted shows switching of R_{nl} associated with the different FM wire coercivities and a $\Delta R_{nl} = 30\ \mu\Omega$.

_IVCurve.vi to confirm it is connected, with the result of the program displaying an IV curve for the circuit configuration, up to the current value selected. The following measurements used the DifferentialConductance_IVCurve.vi, that are then polynomial fitted using OriginLab to obtain a first and second order resistance values. The programs NLSVBoxAMR_PseudoDeltaModeV2.vi and NLSVBoxPseudoDeltaModeAMRMultiChannel.vi were used to measure the resistance of the configurations vs. external field.

5.3. MEASUREMENTS

At a separation distance of 500 nm, the R_{nl} from the electrical injection method was measured as a function of H. Here the H is oriented along the long axis of the FM wires, to align with the magnetization. As the field is swept from 800 Oe to -800 Oe, a switching event occurs around -200 Oe when the wires are antiparallel to each other because of there mismatching volumes therefore magnetic coercivities. The R_{nl}

returns to saturation once both wires are along the same direction and negatively saturated. As the field is swept back upwards, another switching event is observed, yet has a smaller region associated with it. A very peculiar feature, it is unknown the exact reason of the asymmetry, but the R_{nl} displayed the 4 regions expected for such a measurement of injected spin transport. It has the positive and negative saturated regions P_P and P_N as well as the positive and negative antiparallel signal AP_P and AP_N. When subtracting the P_P by the AP_P, a $\Delta R_{nl} = 30\ \mu\Omega$, the value of the nonlocal resistance is recorded. To understand which regime the device is operating in, Figure 5.4 shows the result of measuring the resistances of the contacts and of the channel. To perform these measurements, and switch lead configuration, an SRS Multiplexer is used, allowing for 7 different channels of orientations. The orientations were switched accordingly and an IV curve was taken, the results plotted in Figure 5.4. The results show that the device contact resistances are lower than the channel resistance. While these resistances are smaller than the channel resistance, more information is needed to confirm which regime the device is operating in. Since the spin resistance $\mathcal{R}_{NM} = \rho_{NM}\lambda_{NM}/A_{NM}$ and $\mathcal{R}_{FM} = \rho_{FM}\lambda_{FM}/A_J$ requires a resistivity ρ and spin diffusion length λ, only an estimate can be made.

In Figure 5.4, all the lead orientations that were used are displayed. The contact resistances and the channel resistance all show a linear behavior, as expected, but the when calculating the resistivity for the Al channel, it is 10x higher than that of bulk Al at 20.5 $\mu\Omega$ cm. The increased resistivity can hinder the signal measured, as the ΔR_{nl} is proportional to $\mathcal{R}_{NM}$ but considering the other factors in the transparent limit, it is likely the weakening of the signal is dominated by the squared ratio of resistivities. The ΔR_{nl} value of 30 $\mu\Omega$ is very small when compare to other reports of $> 100\ \mu\Omega$, so it is not surprising that a measurement of the thermal injection shows no switching, as thermal injected nonlocal resistance values can be smaller than that of electrically injected ones, as shown in [26]. The estimated spin resistances are $\mathcal{R}_{NM} = 8.2\ \Omega$ and $\mathcal{R}_{FM} = 3.107\ \mu\Omega$, concluding that the device is neither in the

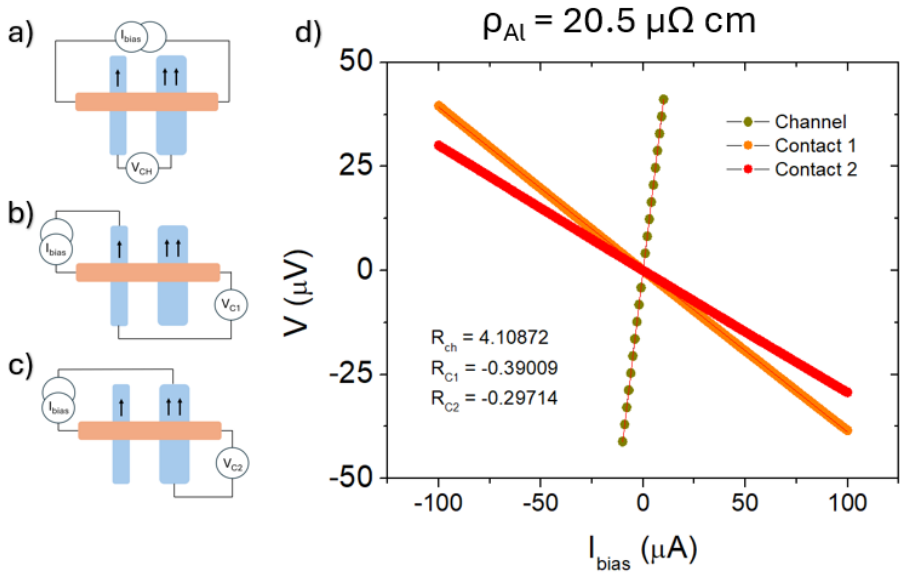

Figure 5.4: Display of circuit configurations and resulting resistances taken from slope of IV curve as all are linear as expected. **a)** shows circuit configuration for measuring channel resistance. **b)** configuration for contact resistance of FM_{inj} **c)** configuration for contact resistance of FM_{det} **d)** IV curves for each configuration displayed up to 100 μA and resulting slopes that correspond to the resistance of each configuration measured. Estimated resistivity of the Al channel ρ is calculated to be 20.5 $\mu\Omega$ cm, which is around 10x of bulk Al, a non-ideal value that is possibly hindering signal of spin transport.

transparent nor tunneling regime. The estimated $\mathcal{R}_F M$ is incredibly small since the geometry of the FM wires is large, with the widths of the wires at the junction on the order of 250 nm, increasing the area of the junction A_J which $\mathcal{R}_{FM}$ is inversely proportional to.

5.4. CONCLUSION

The limited results of the Fe/Al NLSV device measured shows that spin transport can be measured with current fabrication techniques. A two step EBL method and depositing the FM and NM wires in house is realized, with further optimization requirements necessary. This chapter hopes to guide future Zink Lab students to create NLSV devices and measure all 7 circuit configurations using the SRS Multiplexer. The process of ion milling immediately before depositing the second layer Al can lead to transparent contacts between the Fe/Al if the devices can be fabricated at smaller geometries. It is also possible to create a device that operates in the tunneling regime if an intentional insulating layer is deposited above the Fe, as discussed previously. The higher than normal resistivity for Al and the non ideal $\mathcal{R}_{FM}$ led to a calculated spin transport signal of ΔR_{nl} of 30 $\mu\Omega$.

CHAPTER 6:

CONCLUSIONS

In this dissertation, I presented nonlocal measurements of amorphous Yttrium Iron Oxide in attempt to probe for spin transport. Through the use of the spin Hall effect and the inverse spin Hall effect, the hypothesized spin transport through a-Y-Fe-O could not be realized when using lock-in measurement techniques. The signal that was dominated by the reactive, out-of-phase component confirmed that the negative resistance measured was due to capacitive effects, rather than a pure spin transport signal measured from the inverse spin Hall effect. Results also concluded that a-Y-Fe-O is better classified as a speromagnet, with semiconducting behavior rather than insulating, giving rise to charge transport through Mott's variable range hopping.

In the metallic, synthetic, bilayer ferrimagnet Co/Gd, it was shown that a temperature controlled memory device could be realized when measuring the anomalous Hall effect. By utilizing the fact that a ferrimagnet reverses it's magnetization direction when crossing the compensation temperature, a switching of the AHE can be observed that is driven by a change in temperature. Although the process of changing the sample's temperature is slow, fast acting electrical methods to exploit this temperature driven device are discussed. Methods to confirm the compensation temperature of such ferrimagnets, and how to create the memory device were discussed in detail, with the Van Der Pauw method and employed to realize the proof of concept in this dissertation. The identification of perpendicular magnetic anisotropy through the measurement of the anomalous Hall effect in these ferrimagnets was also

detailed. By the observation of square hysteresis loops in the anomalous Hall effect versus a field applied out of plane, a sample with PMA could be confirmed. The results of lower temperature anomalous Hall effect measurements, along with SQUID measurements displayed a shift in PMA for these bilayer Co/Gd samples. A quantitative approach to calculating the anisotropy energies for the in plane and out of plane orientation were outlined, concluding that there is a shift from PMA to IMA at low temperatures. Motivated by the AHE hysteresis loops changing their squareness, SQUID magnetometry hysteresis measurements in the out of plane and in plane directions were used to acurately calculate the anisotropy energies of the respective directions. Results showed a clear switch from PMA to IMA in the Co/Gd samples that was recovered when warming the samples back up.

Finally, a spin transport signal in Fe/Al was displayed, with discussion of which regime the possible fabrication methods can lead to. It is assumed through estimation of the spin resistances of the device measured that the geometry of the FM wires are too wide for more efficient spin injection into the NM channel. Future work should be focused on optimizing the geometry so that the spin resistance of the FM wires are much larger than the contact resistances so that the transparent regime can be realized. An intentional insulating layer above the FM wires could also result in the tunneling regime, where the contact resistances would be much greater than the spin resistance of the NM channel. Once steps are taken for optimization of the signal in the Fe/Al NLSV, implementation of metallic ferrimagnets as the FM wires in the NLSV shows promise for strong spin transport signals, with increased spin diffusion lengths being measured in such materials at compensation temperatures. It is important to note that the measured resistivity of the Al channel in the currently fabricated devices are 10x larger than bulk values, ultimately hindering the spin transport signal measured.

BIBLIOGRAPHY

[1] Althammer, M. (2021). All-electrical magnon transport experiments in magnetically ordered insulators. *Physica status solidi (RRL)–Rapid Research Letters*, *15*(8), 2100130.

[2] Avery, A., Mason, S., Bassett, D., Wesenberg, D., & Zink, B. (2015). Thermal and electrical conductivity of approximately 100-nm permalloy, Ni, Co, Al, and Cu films and examination of the wiedemann-franz law. *Physical Review B*, *92*(21), 214410.

[3] Barker, J., & Atxitia, U. (2021). A review of modelling in ferrimagnetic spintronics. *Journal of the Physical Society of Japan*, *90*(8), 081001.

[4] Blackburn, J. L., Kang, S. D., Roos, M. J., Norton-Baker, B., Miller, E. M., & Ferguson, A. J. (2019). Intrinsic and extrinsically limited thermoelectric transport within semiconducting single-walled carbon nanotube networks. *Advanced Electronic Materials*, *5*(11), 1800910.
URL https://onlinelibrary.wiley.com/doi/abs/10.1002/aelm.201800910

[5] Cai, K., Zhu, Z., Lee, J. M., Mishra, R., Ren, L., Pollard, S. D., He, P., Liang, G., Teo, K. L., & Yang, H. (2020). Ultrafast and energy-efficient spin–orbit torque switching in compensated ferrimagnets. *Nature Electronics*, *3*(1), 37–42.

[6] Campbell, I. (1972). Indirect exchange for rare earths in metals. *Journal of Physics F: Metal Physics*, *2*(3), L47.

[7] Chukalkin, Y. G., Shtirz, V. R., & Goshchitskii, B. N. (1989). The structure and magnetism of amorphous $Y_3Fe_5O_{12}$. *physica status solidi (a)*, *112*(1), 161–174. URL https://onlinelibrary.wiley.com/doi/abs/10.1002/pssa.2211120118

[8] Clark, A., Cohen, M. M., Campi, M., & Lanyon, H. (1974). Magnetoresistance in amorphous germanium. *Journal of Non-Crystalline Solids*, *16*(1), 117–127. URL https://www.sciencedirect.com/science/article/pii/002230937490074X

[9] Coey, J., & Ryan, D. (1984). Current trends in amorphous magnetism. *IEEE Transactions on Magnetics*, *20*(5), 1278–1283.

[10] Coey, J. M. D. (1987). Noncollinear spin structures. *Canadian Journal of Physics*, *65*(10), 1210–1232.

[11] Coey, J. M. D. (2009). *Magnetism and Magnetic Materials*. Cambridge University Press, Cambridge.

[12] Cornelissen, L., Liu, J., Duine, R., Youssef, J. B., & Van Wees, B. (2015). Long-distance transport of magnon spin information in a magnetic insulator at room temperature. *Nature Physics*, *11*(12), 1022–1026.

[13] Cornelissen, L. J., Liu, J., van Wees, B. J., & Duine, R. A. (2018). Spin-current-controlled modulation of the magnon spin conductance in a three-terminal magnon transistor. *Phys. Rev. Lett.*, *120*, 097702. URL https://link.aps.org/doi/10.1103/PhysRevLett.120.097702

[14] Feng, X., Zheng, Z., Zhang, Y., Zhang, Z., Shao, Y., He, Y., Sun, X., Chen, L., Zhang, K., Khalili Amiri, P., et al. (2023). Magneto-ionic control of ferrimagnetic order by oxygen gating. *Nano letters*, *23*(11), 4778–4784.

[15] Finley, J., & Liu, L. (2020). Spintronics with compensated ferrimagnets. *Applied Physics Letters*, *116*(11).

[16] Giles, B. L., Yang, Z., Jamison, J. S., & Myers, R. C. (2015). Long-range pure magnon spin diffusion observed in a nonlocal spin-seebeck geometry. *Phys. Rev. B*, *92*, 224415.
URL https://link.aps.org/doi/10.1103/PhysRevB.92.224415

[17] Goennenwein, S. T., Schlitz, R., Pernpeintner, M., Ganzhorn, K., Althammer, M., Gross, R., & Huebl, H. (2015). Non-local magnetoresistance in YIG/Pt nanostructures. *Applied Physics Letters*, *107*(17).

[18] Gomez-Perez, J. M., Oyanagi, K., Yahiro, R., Ramos, R., Hueso, L. E., Saitoh, E., & Casanova, F. (2020). Absence of evidence of spin transport through amorphous $Y_3Fe_5O_{12}$. *Applied Physics Letters*, *116*(3).

[19] Gückelhorn, J., Wimmer, T., Geprägs, S., Huebl, H., Gross, R., & Althammer, M. (2020). Quantitative comparison of magnon transport experiments in three-terminal YIG/Pt nanostructures acquired via dc and ac detection techniques. *Applied Physics Letters*, *117*(18).

[20] Gyorgy, E. M., Nassau, K., Nassau, K., Eibschutz, M., Waszczak, J. V., Wang, C. A., & Shelton, J. C. (1979). The magnetic properties of amorphous Y3Fe5O12. *Journal of Applied Physics*, *50*(4), 2883–2886.
URL https://doi.org/10.1063/1.326205

[21] Hahn, C., de Loubens, G., Naletov, V. V., Youssef, J. B., Klein, O., & Viret, M. (2014). Conduction of spin currents through insulating antiferromagnetic oxides. *Europhysics Letters*, *108*(5), 57005.
URL https://dx.doi.org/10.1209/0295-5075/108/57005

[22] Han, J., Zhang, P., Bi, Z., Fan, Y., Safi, T. S., Xiang, J., Finley, J., Fu, L., Cheng, R., & Liu, L. (2020). Birefringence-like spin transport via linearly polarized antiferromagnetic magnons. *Nature nanotechnology*, *15*(7), 563–568.

[23] Heinonen, O., & Dimitrov, D. (2010). Switching-current reduction in perpendicular-anisotropy spin torque magnetic tunnel junctions. *Journal of Applied Physics*, *108*(1).

[24] Hirohata, A., & Takanashi, K. (2014). Future perspectives for spintronic devices. *Journal of Physics D: Applied Physics*, *47*(19), 193001.

[25] Hirohata, A., Yamada, K., Nakatani, Y., Prejbeanu, I.-L., Diény, B., Pirro, P., & Hillebrands, B. (2020). Review on spintronics: Principles and device applications. *Journal of Magnetism and Magnetic Materials*, *509*, 166711.

[26] Hojem, A., Wesenberg, D., & Zink, B. L. (2016). Thermal spin injection and interface insensitivity in permalloy/aluminum metallic nonlocal spin valves. *Physical Review B*, *94*(2), 024426.

[27] Hoogeboom, G. R., Nicolaas, G.-J. N. S., Alexander, A., Kuschel, O., Wollschläger, J., Ennen, I., van Wees, B. J., & Kuschel, T. (2021). Role of NiO in the nonlocal spin transport through thin nio films on $Y_3Fe_5O_{12}$. *Phys. Rev. B*, *103*, 144406.
URL https://link.aps.org/doi/10.1103/PhysRevB.103.144406

[28] Huang, M., Hasan, M. U., Klyukin, K., Zhang, D., Lyu, D., Gargiani, P., Valvidares, M., Sheffels, S., Churikova, A., Büttner, F., et al. (2021). Voltage control of ferrimagnetic order and voltage-assisted writing of ferrimagnetic spin textures. *Nature Nanotechnology*, *16*(9), 981–988.

[29] Iacocca, E., & Hoefer, M. A. (2019). Hydrodynamic description of long-distance spin transport through noncollinear magnetization states: Role of dispersion, nonlinearity, and damping. *Phys. Rev. B*, *99*, 184402.
URL https://link.aps.org/doi/10.1103/PhysRevB.99.184402

[30] Ikeda, S., Miura, K., Yamamoto, H., Mizunuma, K., Gan, H., Endo, M., Kanai, S., Hayakawa, J., Matsukura, F., & Ohno, H. (2010). A perpendicular-anisotropy CoFeB–MgO magnetic tunnel junction. *Nature materials*, *9*(9), 721–724.

[31] Ivanov, B. (2020). Spin dynamics for antiferromagnets and ultrafast spintronics. *Journal of Experimental and Theoretical Physics*, *131*, 95–112.

[32] Iwasaki, S.-i. (2012). Perpendicular magnetic recording—its development and realization. *Journal of magnetism and magnetic materials*, *324*(3), 244–247.

[33] Jiang, H., Zhang, W., Zhang, W., & Peng, B. (2010). Effects of argon pressure on magnetic properties and low-field magnetostriction of amorphous TbFe films. *Physica B: Condensed Matter*, *405*(3), 834–838.

[34] Kajiwara, Y., Harii, K., Takahashi, S., Ohe, J.-i., Uchida, K., Mizuguchi, M., Umezawa, H., Kawai, H., Ando, K., Takanashi, K., et al. (2010). Transmission of electrical signals by spin-wave interconversion in a magnetic insulator. *Nature*, *464*(7286), 262–266.

[35] Kameda, M., Bauer, G. E., & Barker, J. (2022). Magnon spectrum of the amorphous ferromagnet Co_4P from atomistic spin dynamics. *Physical Review B*, *106*(6), L060403.

[36] Keffer, F., & Kittel, C. (1952). Theory of antiferromagnetic resonance. *Physical Review*, *85*(2), 329.

[37] Kent, A. D., & Worledge, D. C. (2015). A new spin on magnetic memories. *Nature nanotechnology*, *10*(3), 187–191.

[38] Kim, S. K., Beach, G. S., Lee, K.-J., Ono, T., Rasing, T., & Yang, H. (2022). Ferrimagnetic spintronics. *Nature materials*, *21*(1), 24–34.

[39] Kirby, B. J., Kienzle, P. A., Maranville, B. B., Berk, N. F., Krycka, J., Heinrich, F., & Majkrzak, C. (2012). Phase-sensitive specular neutron reflectometry for imaging the nanometer scale composition depth profile of thin-film materials. *Current Opinion in Colloid & Interface Science*, *17*(1), 44–53.

[40] Knotek, M. L., Pollak, M., Donovan, T. M., & Kurtzman, H. (1973). Thickness dependence of hopping transport in Amorphous-Ge films. *Phys. Rev. Lett.*, *30*, 853–856.
URL https://link.aps.org/doi/10.1103/PhysRevLett.30.853

[41] Lebrun, R., Ross, A., Bender, S., Qaiumzadeh, A., Baldrati, L., Cramer, J., Brataas, A., Duine, R., & Kläui, M. (2018). Tunable long-distance spin transport in a crystalline antiferromagnetic iron oxide. *Nature*, *561*(7722), 222–225.

[42] Lee, P. A., & Ramakrishnan, T. V. (1985). Disordered electronic systems. *Rev. Mod. Phys.*, *57*, 287–337.
URL https://link.aps.org/doi/10.1103/RevModPhys.57.287

[43] Lim, Y., Khodadadi, B., Li, J.-F., Viehland, D., Manchon, A., & Emori, S. (2021). Dephasing of transverse spin current in ferrimagnetic alloys. *Physical Review B*, *103*(2), 024443.

[44] Lin, W., Chen, K., Zhang, S., & Chien, C. L. (2016). Enhancement of thermally injected spin current through an antiferromagnetic insulator. *Phys. Rev. Lett.*, *116*, 186601.
URL https://link.aps.org/doi/10.1103/PhysRevLett.116.186601

[45] Liu, J., Cornelissen, L. J., Shan, J., van Wees, B. J., & Kuschel, T. (2018). Nonlocal magnon spin transport in yttrium iron garnet with tantalum and platinum spin injection/detection electrodes. *Journal of Physics D: Applied Physics*, *51*(22), 224005.

[46] Liu, L., Buhrman, R., & Ralph, D. (2011). Review and analysis of measurements of the spin hall effect in platinum. *arXiv preprint arXiv:1111.3702*.

[47] Maranville, B., Ratcliff II, W., & Kienzle, P. (2018). *reductus*: a stateless Python data reduction service with a browser front end. *Journal of Applied Crystallography*, *51*(5), 1500–1506.
URL https://doi.org/10.1107/S1600576718011974

[48] Markov, I. L. (2014). Limits on fundamental limits to computation. *Nature*, *512*(7513), 147–154.

[49] Medvedeva, J. E., Buchholz, D. B., & Chang, R. P. (2017). Recent advances in understanding the structure and properties of amorphous oxide semiconductors. *Advanced Electronic Materials*, *3*(9), 1700082.

[50] Mott, N. F., & Davis, E. A. (1971). *Electronic processes in non-crystalline materials*, vol. 14. Oxford University Press Oxford.

[51] Nagaosa, N., Sinova, J., Onoda, S., MacDonald, A. H., & Ong, N. P. (2010). Anomalous hall effect. *Reviews of modern physics*, *82*(2), 1539.

[52] Nozaki, T., Yamamoto, T., Tamaru, S., Kubota, H., Fukushima, A., Suzuki, Y., & Yuasa, S. (2018). Enhancement in the interfacial perpendicular magnetic anisotropy and the voltage-controlled magnetic anisotropy by heavy metal doping at the Fe/MgO interface. *APL Materials*, *6*(2).

[53] Ochoa, H., Zarzuela, R., & Tserkovnyak, Y. (2018). Spin hydrodynamics in amorphous magnets. *Phys. Rev. B*, *98*, 054424.
URL https://link.aps.org/doi/10.1103/PhysRevB.98.054424

[54] O'Handley, R. (1999). *Modern Magnetic Materials: Principles and Applications*. Wiley.
URL https://books.google.com/books?id=RKV1QgAACAAJ

[55] Ohta, M., Yamada, K., Satake, Y., Fujita, A., & Fukamichi, K. (2003). Origin of perpendicular magnetic anisotropy in tb-fe amorphous alloy. *Materials Transactions*, *44*(12), 2605–2610.

[56] QD (2019). Quantum design north america.
URL http://https://www.qdusa.com/

[57] Ren, X., Liu, L., Cui, B., Cheng, B., Liu, W., An, T., Chu, R., Zhang, M., Miao, T., Zhao, X., et al. (2023). Control of compensation temperature in CoGd films through hydrogen and oxygen migration under gate voltage. *Nano Letters*, *23*(13), 5927–5933.

[58] Shan, J., Cornelissen, L. J., Vlietstra, N., Ben Youssef, J., Kuschel, T., Duine, R. A., & van Wees, B. J. (2016). Influence of yttrium iron garnet thickness and heater opacity on the nonlocal transport of electrically and thermally excited magnons. *Phys. Rev. B*, *94*, 174437.
URL https://link.aps.org/doi/10.1103/PhysRevB.94.174437

[59] Shan, J., Singh, A., Liang, L., Cornelissen, L., Galazka, Z., Gupta, A., Van Wees, B., & Kuschel, T. (2018). Enhanced magnon spin transport in $NiFe_2O_4$ thin films on a lattice-matched substrate. *Applied Physics Letters*, *113*(16).

[60] Sinova, J., Valenzuela, S. O., Wunderlich, J., Back, C., & Jungwirth, T. (2015). Spin hall effects. *Reviews of modern physics*, *87*(4), 1213.

[61] Smart, J. S. (1955). The néel theory of ferrimagnetism. *American Journal of Physics*, *23*(6), 356–370.

[62] Srinivasan, K., Chen, Y., Cestarollo, L., Dare, D. K., Wright, J. G., & El-Ghazaly, A. (2023). Engineering large perpendicular magnetic anisotropy in amorphous ferrimagnetic gadolinium cobalt alloys. *Journal of Materials Chemistry C*, *11*(14), 4820–4829.

[63] Stern, O. (1921). A way to experimentally test directional quantization in the magnetic field. *journal for physics*, *7*(1), 249–253.

[64] Sultan, R., Avery, A., Stiehl, G., & Zink, B. (2009). Thermal conductivity of micromachined low-stress silicon-nitride beams from 77 to 325 k. *Journal of Applied Physics*, *105*(4).

[65] Sultan, R., Avery, A., Underwood, J., Mason, S., Bassett, D., & Zink, B. (2013). Heat transport by long mean free path vibrations in amorphous silicon nitride near room temperature. *Physical review B*, *87*(21), 214305.

[66] Takahashi, S., & Maekawa, S. (2003). Spin injection and detection in magnetic nanostructures. *Physical Review B*, *67*(5), 052409.

[67] Taylor, R., & Gangulee, A. (1976). Magnetization and magnetic anisotropy in evaporated gdco amorphous films. *Journal of Applied Physics*, *47*(10), 4666–4668.

[68] Thiery, N., Draveny, A., Naletov, V. V., Vila, L., Attané, J. P., Beigné, C., de Loubens, G., Viret, M., Beaulieu, N., Ben Youssef, J., Demidov, V. E., Demokritov, S. O., Slavin, A. N., Tiberkevich, V. S., Anane, A., Bortolotti, P., Cros, V., & Klein, O. (2018). Nonlinear spin conductance of yttrium iron garnet thin films driven by large spin-orbit torque. *Phys. Rev. B*, *97*, 060409. URL https://link.aps.org/doi/10.1103/PhysRevB.97.060409

[69] Thiery, N., Naletov, V. V., Vila, L., Marty, A., Brenac, A., Jacquot, J.-F., de Loubens, G., Viret, M., Anane, A., Cros, V., Ben Youssef, J., Beaulieu, N.,

Demidov, V. E., Divinskiy, B., Demokritov, S. O., & Klein, O. (2018). Electrical properties of epitaxial yttrium iron garnet ultrathin films at high temperatures. *Phys. Rev. B*, *97*, 064422.
URL https://link.aps.org/doi/10.1103/PhysRevB.97.064422

[70] Tserkovnyak, Y., & Ochoa, H. (2017). Generalized boundary conditions for spin transfer. *Phys. Rev. B*, *96*, 100402.
URL https://link.aps.org/doi/10.1103/PhysRevB.96.100402

[71] Tudu, B., & Tiwari, A. (2017). Recent developments in perpendicular magnetic anisotropy thin films for data storage applications. *Vacuum*, *146*, 329–341.

[72] Ueda, K., Tan, A. J., & Beach, G. S. (2018). Effect of annealing on magnetic properties in ferrimagnetic GdCo alloy films with bulk perpendicular magnetic anisotropy. *AIP Advances*, *8*(12).

[73] Wadley, P., Howells, B., Železnỳ, J., Andrews, C., Hills, V., Campion, R. P., Novák, V., Olejník, K., Maccherozzi, F., Dhesi, S., et al. (2016). Electrical switching of an antiferromagnet. *Science*, *351*(6273), 587–590.

[74] Walowski, J., & Münzenberg, M. (2016). Perspective: Ultrafast magnetism and THz spintronics. *Journal of Applied Physics*, *120*(14).

[75] Wang, H., Du, C., Hammel, P. C., & Yang, F. (2014). Antiferromagnonic Spin Transport from $Y_3Fe_5O_{12}$ into NiO. *Phys. Rev. Lett.*, *113*, 097202.
URL https://link.aps.org/doi/10.1103/PhysRevLett.113.097202

[76] Wang, H., Du, C., Hammel, P. C., & Yang, F. (2015). Spin transport in antiferromagnetic insulators mediated by magnetic correlations. *Phys. Rev. B*, *91*, 220410.
URL https://link.aps.org/doi/10.1103/PhysRevB.91.220410

[77] Wesenberg, D., Liu, T., Balzar, D., Wu, M., & Zink, B. L. (2017). Long-distance spin transport in a disordered magnetic insulator. *Nature Physics*, *13*(10), 987–993.

[78] Wesenberg, D. J., Roos, M. J., Avery, A. D., Blackburn, J. L., Ferguson, A. J., & Zink, B. L. (2020). Size- and temperature-dependent suppression of phonon thermal conductivity in carbon nanotube thermoelectric films. *Advanced Electronic Materials*, *6*(11), 2000746.
URL https://onlinelibrary.wiley.com/doi/abs/10.1002/aelm.202000746

[79] Williams, R. S. (2017). What's next?[the end of moore's law]. *Computing in Science & Engineering*, *19*(2), 7–13.

[80] Wong, H.-S. P., & Salahuddin, S. (2015). Memory leads the way to better computing. *Nature nanotechnology*, *10*(3), 191–194.

[81] Wu, H., Huang, L., Fang, C., Yang, B. S., Wan, C. H., Yu, G. Q., Feng, J. F., Wei, H. X., & Han, X. F. (2018). Magnon valve effect between two magnetic insulators. *Phys. Rev. Lett.*, *120*, 097205.
URL https://link.aps.org/doi/10.1103/PhysRevLett.120.097205

[82] Yakushiji, K., Saruya, T., Kubota, H., Fukushima, A., Nagahama, T., Yuasa, S., & Ando, K. (2010). Ultrathin Co/Pt and Co/Pd superlattice films for MgO-based perpendicular magnetic tunnel junctions. *Applied Physics Letters*, *97*(23).

[83] Yang, L., Gu, Y., Chen, L., Zhou, K., Fu, Q., Wang, W., Li, L., Yan, C., Li, H., Liang, L., Li, Z., Pu, Y., Du, Y., & Liu, R. (2021). Absence of spin transport in amorphous YIG evidenced by nonlocal spin transport experiments. *Phys. Rev. B*, *104*, 144415.
URL https://link.aps.org/doi/10.1103/PhysRevB.104.144415

[84] Yang, S.-H., Ryu, K.-S., & Parkin, S. (2015). Domain-wall velocities of up to 750 m s- 1 driven by exchange-coupling torque in synthetic antiferromagnets. *Nature nanotechnology*, *10*(3), 221–226.

[85] Yuan, W., Zhu, Q., Su, T., Yao, Y., Xing, W., Chen, Y., Ma, Y., Lin, X., Shi, J., Shindou, R., et al. (2018). Experimental signatures of spin superfluid ground state in canted antiferromagnet Cr_2O_3 via nonlocal spin transport. *Science advances*, *4*(4), eaat1098.

[86] Zhao, R., Ren, Z., Cao, J., Yuan, Y., Zhao, G., Xu, X., Meng, K., Miao, J., & Jiang, Y. (2021). Influence of heavy-metal capping layers on perpendicular magnetic anisotropy and spin-orbit torques of Pt/Co/HM stacks structures. *Solid State Communications*, *332*, 114340.

[87] Zheng, Z., Zhang, Y., Feng, X., Zhang, K., Nan, J., Zhang, Z., Wang, G., Wang, J., Lei, N., Liu, D., et al. (2019). Enhanced spin-orbit torque and multilevel current-induced switching in W/Co-Tb/Pt heterostructure. *Physical Review Applied*, *12*(4), 044032.

[88] Zink, B. L., Manno, M., O'Brien, L., Lotze, J., Weiler, M., Bassett, D., Mason, S. J., Goennenwein, S. T. B., Johnson, M., & Leighton, C. (2016). Efficient spin transport through native oxides of nickel and permalloy with platinum and gold overlayers. *Phys. Rev. B*, *93*, 184401.
URL https://link.aps.org/doi/10.1103/PhysRevB.93.184401

APPENDIX A

LABVIEW PROGRAMS

The following programs were used for electrical measurements displayed in this dissertation. Because programs are constantly being updated and optimized, there may be newer versions when referencing this appendix. The programs use a variety of GPIB and RS232 connections to communicate with the Lakeshore Gaussmeter, the Keithley 6221/2182, the SRS Sim 900, and the Lakeshore Temperature Controller.

A.1. FieldSetBZv3.vi

This program sets the field of the electromagnet in the magnet crysotat. The desired field, along with a tolerance is set, so that a PID type algorithm efficiently applies the desired field. Many programs use this as a sub vi to apply a static field, and instead have different methods for stepping the field when doing hysteresis measurements. The National Instruments IO connected through USB outputs an analog signal to the Kepco power supply that converts this analog signal into the desired field.

A.2. DeltaModeVsTwithRegulationAndFieldv2.vi

This program measures the delta mode voltage of the sample using the Keithley 6221/2182 source-meter pair, with a selected applied external field value, and plots the voltage versus temperature. The temperature range can be changed, along with the temperature step size, and is regulated with the following program at each step. This is the program that was used to perform the proof of concept measurements for the temperature driven memory device. The user can start the measurement at low T and measure to high T, and visa versa.

A.3. Temp_Regulation Slope2DUWithRangeScalingv4useDeltaMeasv2 _WritesTempFile.vi

This program uses the delta mode feature of the Keithley 6221/2182 source-meter pair to regulate a target temperature. At the time of writing this, the delta mode function must be triggered before the program is started. Once a selected bias current and delay time is set for the delta mode, pressing trigger will turn on the bias current and a voltage measured by the delta mode is displayed. This measurement is plotted against time in this program and has certain parameters needed in order to achieve regulation. The values used for regulating temperature for the delta mode measurements of this dissertation are as follows. Slope const = 75. Delay const = 25. Max Slope = 5E-8 and Res samples per step = 10. The slope constant is how many times a measurement will be made before calculating a slope. The delay constant is used to disregard the first 25 measurements before starting to measure a slope. The max slope value is the threshold used to confirm regulation, and the resistance samples per step is how many delta mode samples are taken before a measurement is outputted.

A.4. Master_AMR_Delta_Hysteresis_vsT.vi

This uses the Keithley 6221/2182 Delta Mode feature to take hysteresis measurements of the delta mode voltage versus external field at various temperatures. An array of selected temperatures is selected so that the hysteresis measurement is taken at the temperature once regulation has been achieved. The regulation program is built in as a sub vi for this, so it's not required to use separately. Once the array of the temperatures is chosen, the program will run until all temperatures measurements have been conducted. This was used to perform the anomalous Hall effect measurements of the metallic ferrimagnet samples using the Van Der Pauw method, or the Hall bar method.

The sub vi in this program named Master_AMR_Delta_HysteresisV2.vi is the program that conducts the hysteresis loop at one temperature. This can be used as a single temperature measurement before an array of temperatures is desired. Most delta mode hysteresis measurements at room temperature were done with this temperature, or when one specific temperature's delta mode vs. field is desired.

A.5. DifferentialConductance_IVCurve.vi

This program uses the Keithley 6221/2182 differential conductance feature to measure an IV curve. The user provides the program with the desired I min, I max to perform an IV curve starting from the I min and stepping with the selected step size to I max. A delta current parameter is provided by the user so at each step, the current is offset by this delta to determine the change in voltage for each step. Other settings include a delay time, and number of averages. The delay time is a parameter that dictates the delay between each current step, and the number of averages determines how many IV curves are averaged before the final IV curve is outputted. The program uses an integration feature to construct an accurate IV curve, and fits a polynomial to this curve to output up to the third order resistance value. The zeroth order value corresponds to Ohm's Law and the first order to Joule heating. Higher orders are not used for interpretation of any of the data performed. The text file that is outputted is data for the current, dV, R and the integrated V.

A.6. NLSVBoxAMR_PseudoDeltaModeB2.vi

This program uses the Keithley 6221/2182 DC option perform a pseudo delta mode measurement versus external field. It applies a 0 current, I high, and I low (1 cycle) to determine the same resistance values as the DifferentialConductance_IVCurve would output, but using a "more" DC method rather than the effective AC nature of the differential conductance. This program was developed in hopes to reduce noise in the measurements of the NLSV device when measuring versus field. The delta mode and differential conductance methods versus external field had particularly noisy data,

and this program allowed for a more stable measurement versus field. The number of samples is the value that dictates how many samples are measured at each current value before a pseudo delta mode value is calculated from that one cycle. The number of cycles dictates how many times each 0 current, I high and I low is performed before an resistance value is recorded for each field step. The user inputs the max and min field values as well as the step size of the field depending on the information and resolution of data desired. Increasing the number of samples and cycles can increase the signal to noise ratio, at cost of time.

A.7. NLSVBoxPseudoDeltaModeAMRMultiChannel

This program takes the previous LabView program as a sub vi in order to perform a resistance versus field run for the selected channels of the SRS Multiplexer. For the NLSV measurements, there are 7 channels, so this VI could perform a pseudo delta mode measurement vs. field for all user selected channels. The same parameters from the previous program are inputted here, along with which channels the measurements should be taken for. This program comminucates with the SRS SIM 900 multiplexer in order to change which channel is measured.

APPENDIX B

PYTHON CODE

B.1. MvsH_analysis_.py

This code processes SQUID M vs. H raw data and outputs a text file with all variables obtained from code in SI units. The user must convert the .dat file the SQUID outputs into an excel worksheet, and the end_row variables can be adjusted depending on the amount of data points the raw data has. The temperature variable is used to correspond to the naming convention I chose for the data files, and is used in selecting the correct data from the working directory. The volume variable is sample dependent and is required to obtain accurate results in SI units. The lr variable determines how many data points are used in the linear regression used for background subtraction, as well as the M_s calculation. Basic plots are displayed for reference, and can be saved, but the text file was then used in OriginLab to further analyze and plot data.

```
1
2  import pandas as pd
3  import numpy as np
4  import matplotlib.pyplot as plt
5
6  # Define the base part of the Excel file name
7  base_file_name = 'FBL001_cleaved_IP_11092023_MvsH_3T_RSO_'
8
9  #set style for plots
10 plt.style.use('seaborn')
11
12 #set temperature
```

```
temperature = 300

# Define the volume variable
volume = 5.57865E-8

#Define how many points to take for a linear regression
lr = 14

# Initialize lists to store average x-intercepts and temperatures
average_x_intercepts = []
temperatures = []

# Create a new figure for all plots
plt.figure()

# Construct the complete file name by concatenating the base name
↪  and temperature
excel_file_name = f'{base_file_name}{temperature}K.xlsx'

# Load the Excel file into a Pandas DataFrame
df = pd.read_excel(excel_file_name)

# Extract the desired columns and rows
start_row = 31
end_row = 264

#Extracts field temperature and long moment collumns, can add std
↪  dev and other collumns if necessary
```

```
field_oe = pd.to_numeric(df.iloc[start_row-1:end_row-1, 2], errors='coerce').to_numpy() #Column C
temperature_k = pd.to_numeric(df.iloc[start_row-1:end_row-1, 3], errors='coerce').to_numpy()  # Column D
long_moment_emu = pd.to_numeric(df.iloc[start_row-1:end_row-1, 4], errors='coerce').to_numpy()  # Column E

# Perform element-wise division to create the 'magnetization' array in emu/cc
magnetization = long_moment_emu / volume

#Convert magnetization to A/m and field to T
magnetization_SI = magnetization * 1E3
field_SI = field_oe / 10E3

# Take elements for use in linear regression, this is the lr variable for linear regression
magnetization_SI_lr = np.array(magnetization_SI[:lr])
field_SI_lr = np.array(field_SI[:lr])

# Perform linear regression
slope, intercept = np.polyfit(field_SI_lr, magnetization_SI_lr, 1)

#Subtract slope from magnetization data
#If linear regression does not get accurate slope use this next variable
slope_user = -131850.5

```

```
subtraction = slope * field_SI
magnetization_adjusted_SI = magnetization_SI - subtraction

#Calculate average of Ms
saturation_magnetization_SI =
    ↪ np.mean(magnetization_adjusted_SI[:lr])

print(f'Slope: {slope} J/m\N{SUPERSCRIPT THREE}')
print(f'Ms: {saturation_magnetization_SI} A/m')

# Compute the derivative of magnetization_adjusted_SI with respect
    ↪ to field_SI
d_magnetization_adjusted_SI =
    ↪ np.gradient(magnetization_adjusted_SI, field_SI)

# Calculate x-intercepts for coercivity
x_intercepts_indices =
    ↪ np.where(np.diff(np.sign(magnetization_adjusted_SI)))[0]
x_intercepts_values = field_SI[x_intercepts_indices]

# Calculate y-intercepts for Mr
y_intercepts_indices = np.where(np.diff(np.sign(field_SI)))[0]
y_intercepts_values =
    ↪ magnetization_adjusted_SI[y_intercepts_indices]

# Print x-intercepts
print("X-intercepts:")
for x_intercept in x_intercepts_values:
```

```
84      print(f'Field at x-intercept: {x_intercept} T')
85
86  # Calculate the average of the absolute values of the x-intercepts
87  if len(x_intercepts_values) >= 2:
88      x_intercept_avg = np.mean(np.abs(x_intercepts_values))
89      print(f'Hc: {x_intercept_avg} T')
90  else:
91      print('Error calculating Hc')
92
93  # Print y-intercepts
94  print("Y-intercepts:")
95  for y_intercept in y_intercepts_values:
96      print(f'Mr: {y_intercept} T')
97
98  # Calculate the average of the absolute values of the y-intercepts
99  if len(y_intercepts_values) >= 2:
100     y_intercept_avg = np.mean(np.abs(y_intercepts_values))
101     print(f'Mr: {y_intercept_avg} A/m')
102 else:
103     print('Error calculating Mr')
104
105 # Calculate Mr/Ms
106 squareness = y_intercept_avg / saturation_magnetization_SI
107 print(f'Squareness: {squareness}')
108
109 # Iterate through the field_SI array to find the field value at
    ↪ which magnetization_adjusted_SI is equal to
    ↪ saturation_magnetization_SI
```

```
rtol = 0.01
atol = 0.01 * np.max(np.abs(magnetization_adjusted_SI))

# Find the indices where the magnetization_adjusted_SI crosses zero
zero_crossing_indices = np.where(np.diff(np.sign(magnetization_adjusted_SI)))[0]

# Initialize the starting index to the first zero crossing index or the beginning of the array
start_index = zero_crossing_indices[0] if zero_crossing_indices.size > 0 else 0

# Iterate through the field_SI array starting from the specified index

found_index = None
for i in range(start_index, len(magnetization_adjusted_SI)):
    mag_adjusted = magnetization_adjusted_SI[i]
    if np.isclose(mag_adjusted, saturation_magnetization_SI, rtol=rtol, atol=atol):
        found_index = i
        break

# Check if a matching index was found
if found_index is not None:
    field_at_saturation = field_SI[found_index]
    print(f'Hs: {field_at_saturation} T')
```

```
else:
    print('Error calculating Hs')

# Create a DataFrame with the data
data = pd.DataFrame({
    'H (T)': field_SI,
    'M (A/m)': magnetization_SI,
    'M subtracted (A/m)': magnetization_adjusted_SI,
    'dM/dH (J/m^3)': d_magnetization_adjusted_SI,
    'slope (J/m^3)': slope,
    'Ms (A/m)': saturation_magnetization_SI,
    'Mr (A/m)': y_intercept_avg,
    'squareness': squareness,
    'Hc (T)': x_intercept_avg,
    'Hs (T)': field_at_saturation
})

# Save the DataFrame to a text file
text_file_name = f'{base_file_name}{temperature}K_SIadjusted.txt'
# Save the data to the text file
data.to_csv(text_file_name, sep='\t', index=False)

#Clear Plot
#plt.figure()

#2D Plot Magnetization vs Field
plt.plot(field_SI, magnetization_adjusted_SI,
 ↪  label=f'{temperature}K', marker='o', color='black')
```

```
159
160 # Add a vertical line at the field_at_saturation value
161 if found_index is not None:
162     plt.axvline(x=field_at_saturation, color='red',
      ↪  linestyle='--', label='Saturation Field')
163
164 # Add a horizontal line at the saturation_magnetization_SI value
165 plt.axhline(y=saturation_magnetization_SI, color='blue',
    ↪  linestyle='--', label='Saturation Magnetization')
166
167 # Add labels and title
168 plt.xlabel('Field (T)')
169 plt.ylabel('Magnetization (A/m)')
170 plt.legend(loc='upper left')
171
172 # Set the limits for the x and y axes to zoom into a specific
    ↪  section
173 plt.xlim([-1, 1])  # Replace xmin and xmax with your desired
    ↪  x-axis limits
174 plt.ylim([-20000, 20000])  # Replace ymin and ymax with your
    ↪  desired y-axis limits
175
176 # Plot the derivative separately
177 plt.figure()
178 plt.plot(field_SI, d_magnetization_adjusted_SI,
    ↪  label=f'{temperature}K', marker='o', color='red')
179
180 # Add labels and title for the derivative plot
```

```
plt.xlabel('Field (A/m)')
plt.ylabel('dM/dH')
plt.legend(loc='upper left')

#Save plot as png
plt.savefig(f'{base_file_name}{temperature}K.png', format='png')
```

B.2. MvsH_coercivityvsT.py

This code was used to iterate through all M vs. H data taken at various temperatures to obtain coercivity values and plot vs temperature. Like the previous code, the .dat file the SQUID outputs must be converted to an excel worksheet, and adjustment of end_row variable will vary depending on how many data points of the data. The magnetization axis is normalized to obtain coercivities from the x-intercepts of the hysteresis curve. The coercivity vs. temperature is then plotted and a figure could be saved if desired, but a text file is outputted to be further analyzed in OriginLab.

```
import pandas as pd
import numpy as np
import matplotlib.pyplot as plt

# Define the base part of the Excel file name
base_file_name = 'FAL001_OOP_10032023_MvsH_2000Oe_RSO_'

# Define the interval for iterating temperatures
temperature_interval = 20

#Set temperature
temperature = 20

```

```
#set style for plots
plt.style.use('seaborn')

# Initialize lists to store average x-intercepts and temperatures
average_x_intercepts = []
temperatures = []

# Loop through temperatures 20K to 300K in 20K steps
for temperature in range(20, 301, temperature_interval):

    # Construct the complete file name by concatenating the base
    ↪ name and temperature
    excel_file_name = f'{base_file_name}{temperature}K.xlsx'

    # Load the Excel file into a Pandas DataFrame
    df = pd.read_excel(excel_file_name)

    # Extract the desired columns and rows
    start_row = 31
    end_row = 213

    field_oe = df.iloc[start_row-1:end_row-1, 2].to_numpy()
    ↪ #Column C
    temperature_k = df.iloc[start_row-1:end_row-1, 3].to_numpy()
    ↪ # Column D
    long_moment_emu = df.iloc[start_row-1:end_row-1, 4].to_numpy()
    ↪ # Column E

```

```
    # Define the volume variable
    volume = 1

    # Perform element-wise division to create the 'magnetization' array
    magnetization = long_moment_emu / volume

    # Normalize the voltage array
    normalized_moment = 2 * (long_moment_emu - np.min(long_moment_emu)) / (np.max(long_moment_emu) - np.min(long_moment_emu)) - 1

    # Calculate x-intercepts for coercivity
    x_intercepts_indices = np.where(np.diff(np.sign(long_moment_emu)))[0]
    x_intercepts_values = field_oe[x_intercepts_indices]

    # Calculate the average of the absolute values of the x-intercepts
    if len(x_intercepts_values) >= 2:
        x_intercept_avg = np.mean(np.abs(x_intercepts_values))
        print(f'Average of absolute values of x-intercepts: {x_intercept_avg} Oe')

        # Append the average x-intercept and temperature to the lists
        average_x_intercepts.append(x_intercept_avg)
        temperatures.append(temperature)
```

```
59
60      else:
61          print('Insufficient x-intercepts to calculate an
            ↪  average.')
62
63
64      # Create a 3D text file with field, long_moment_emu, and
        ↪  magnetization columns
65      text_file_name = f'{base_file_name}{temperature}K.txt'
66      data = np.column_stack((field_oe, long_moment_emu,
        ↪  magnetization))
67      np.savetxt(text_file_name, data, header='Field (Oe) Long
        ↪  Moment (emu) Magnetization', delimiter='\t', comments='')
68
69      # Create a new figure for each plot
70      plt.figure()
71
72      #2D Plot Magnetization vs Field
73      plt.plot(field_oe, long_moment_emu, label=f'{temperature}K',
        ↪  marker='o', color='black')
74
75      # Add labels and title
76      plt.xlabel('Field (Oe)')
77      plt.ylabel('Magnetization (emu/cc)')
78      plt.legend(loc='upper left')
79
80      #Save plot as png
```

```
81      plt.savefig(f'{base_file_name}{temperature}K.png',
        ↪  format='png')
82
83
84
85  # Convert lists to NumPy arrays if needed
86  average_x_intercepts = np.array(average_x_intercepts)
87  temperatures = np.array(temperatures)
88
89  # Combine the arrays into a single 2D array
90  data_to_save = np.column_stack((temperatures,
    ↪  average_x_intercepts))
91
92  # Define the file path where you want to save the text file
93  output_file_path = 'coercivityvstemperature_80K_200K.txt'
94
95  # Save the data to a text file
96  np.savetxt(output_file_path, data_to_save, header='Temperature
    ↪  (K)\tCoercivity (Oe)', fmt='%.2f', delimiter='\t')
97
98  plt.figure()
99
100 # Create a plot of average x-intercepts vs temperature
101 plt.plot(temperatures, average_x_intercepts, marker='o',
    ↪  color='blue')
102 plt.title('Coercivity vs Temperature FAL001')
103 plt.xlabel('Temperature (K)')
104 plt.ylabel('Coercivity (Oe)')
```

```
plt.grid(True)

#Save plot as png
plt.savefig('coercivityvstemperature_80K_200K.png', format='png')
plt.show()
```

B.3. MvsH_alltemps.py

This code is used to quickly plot M vs. H for a sample at all temperatures measured for an orientation by iterating through the temperatures data was taken at (here at an interval of 20 K from 20 K to 300 K. Like the previous codes, the .dat file from the SQUID needs to be converted to an excel worksheet and the bounds adjusted with the end_row variable. The code outputs images that can be saved if desired, but also a text file that contains the magnetization in units of emu/cc. The volume variable must be accurately adjusted depending on sample to obtain precise magnetization values. This text file is then used in OriginLab for further analysis.

```
import pandas as pd
import numpy as np
import matplotlib.pyplot as plt

# Define the base part of the Excel file name
base_file_name = 'FAL001_OOP_10032023_MvsH_2000Oe_RSO_'

# Define the interval for iterating temperatures
temperature_interval = 20

#set style for plots
plt.style.use('seaborn')

```

```
# Loop through temperatures 20K to 300K in 20K steps
for temperature in range(20, 301, temperature_interval):

    # Construct the complete file name by concatenating the base
    ↪ name and temperature
    excel_file_name = f'{base_file_name}{temperature}K.xlsx'

    # Load the Excel file into a Pandas DataFrame
    df = pd.read_excel(excel_file_name)

    # Extract the desired columns and rows
    start_row = 31
    end_row = 213

    field_oe = df.iloc[start_row-1:end_row-1, 2].to_numpy()
    ↪ #Column C
    temperature_k = df.iloc[start_row-1:end_row-1, 3].to_numpy()
    ↪ # Column D
    long_moment_emu = df.iloc[start_row-1:end_row-1, 4].to_numpy()
    ↪ # Column E

    # Define the volume variable
    volume = 1

    # Perform element-wise division to create the 'magnetization'
    ↪ array
    magnetization = long_moment_emu / volume

```

```
    # Create a 3D text file with field, long_moment_emu, and magnetization columns
    text_file_name = f'{base_file_name}{temperature}K.txt'
    data = np.column_stack((field_oe, long_moment_emu, magnetization))
    np.savetxt(text_file_name, data, header='Field (Oe) Long Moment (emu) Magnetization', delimiter='\t', comments='')

    # Create a new figure for each plot
    plt.figure()

    #2D Plot Magnetization vs Field
    plt.plot(field_oe, magnetization, label=f'{temperature}K', marker='o', color='black')

    # Add labels and title
    plt.xlabel('Field (Oe)')
    plt.ylabel('Magnetization (emu/cc)')
    plt.legend(loc='upper left')

    #Save plot as png
    plt.savefig(f'{base_file_name}{temperature}K.png', format='png')
```

B.4. VvsH_alltemps.py

This is a code used to take the text file generated from the LabView code Master_AMR_Delta_Hysteresis_vsT.vi in order to obtain a coercivity vs. temperature from the AHE data. The code iterates through all temperatures measured, in

a interval defined as temperature_interval, and plots the normalized loops all in one plot, as well as the coercivity vs temperature. The data plotted is saved as a text file so that further analysis can be obtained.

```
import pandas as pd
import numpy as np
import matplotlib.pyplot as plt

# Define the base part of the Excel file name
base_file_name = '05042022_250uA_2msDelay_1500Oe_'


#set style for plots
plt.style.use('seaborn')

# Define the interval for iterating temperatures
temperature_interval = 20

#set temperature
temperature = 80

# Initialize lists to store average x-intercepts and temperatures
average_x_intercepts = []
temperatures = []

# Create a new figure for all plots
plt.figure()

# Loop through temperatures 80K to 300K in 20K steps
```

```
for temperature in range(80, 301, temperature_interval):

    #Name the file path
    file_path = f'{base_file_name}{temperature}.txt'

    # Use numpy's loadtxt function to load the data
    data = np.loadtxt(file_path)

    # Assuming your file has two columns, you can assign them to
    ↪ separate arrays
    field_oe = data[:, 0]
    voltage = data[:, 1]

    # Normalize the voltage array
    normalized_voltage = 2 * (voltage - np.min(voltage)) /
    ↪ (np.max(voltage) - np.min(voltage)) - 1

    # Calculate x-intercepts for coercivity
    x_intercepts_indices =
    ↪ np.where(np.diff(np.sign(normalized_voltage)))[0]
    x_intercepts_values = field_oe[x_intercepts_indices]

    # Calculate the average of the absolute values of the
    ↪ x-intercepts
    if len(x_intercepts_values) >= 2:
        x_intercept_avg = np.mean(np.abs(x_intercepts_values))
        print(f'Average of absolute values of x-intercepts:
        ↪ {x_intercept_avg} Oe')
```

```
49
50          # Append the average x-intercept and temperature to the
            ↪ lists
51          average_x_intercepts.append(x_intercept_avg)
52          temperatures.append(temperature)
53
54      else:
55          print('Insufficient x-intercepts to calculate an
            ↪ average.')
56
57      #2D Plot Magnetization vs Field
58      plt.plot(field_oe, normalized_voltage,
        ↪ label=f'{temperature}K', marker='o')
59
60      # Highlight x-intercepts on the plot
61      plt.scatter(x_intercepts_values,
        ↪ np.zeros_like(x_intercepts_values), color='red',
        ↪ label='X-intercepts')
62
63      #Save plot as png
64      plt.savefig(f'{base_file_name}{temperature}K.png',
        ↪ format='png')
65
66
67  # Add labels and title
68  plt.title('Voltage vs Field FBL004')
69  plt.xlabel('Field (Oe)')
70  plt.ylabel('Voltage (a.u.)')
```

```
plt.legend(loc='lower left')

# Save the entire plot as png
plt.savefig('combined_plots.png', format='png')
plt.show()

# Convert lists to NumPy arrays if needed
average_x_intercepts = np.array(average_x_intercepts)
temperatures = np.array(temperatures)

# Combine the arrays into a single 2D array
data_to_save = np.column_stack((temperatures,
    average_x_intercepts))

# Define the file path where you want to save the text file
output_file_path = 'coercivityvstemperature_80K_200K.txt'

# Save the data to a text file
np.savetxt(output_file_path, data_to_save, header='Temperature
    (K)\tCoercivity (Oe)', fmt='%.2f', delimiter='\t')

plt.figure()

# Create a plot of average x-intercepts vs temperature
plt.plot(temperatures, average_x_intercepts, marker='o',
    color='blue')
plt.title('Coercivity vs Temperature FBL004')
plt.xlabel('Temperature (K)')
```

```
plt.ylabel('Coercivity (Oe)')
plt.grid(True)

#Save plot as png
plt.savefig('coercivityvstemperature_80K_200K.png', format='png')
plt.show()
```

B.5. MvsT.py

This code takes the raw M vs. T data from the SQUID, and converts the magnetization to emu/cc. It then plots the M vs. T data after separating the ZFC and FC branches of the measurement. This can only work when the rows in the excel file are known for when the ZFC and FC measurements are done. Usually, the M vs. T sequences in the SQUID perform the ZFC branch first, from a low T to high T, then the FC branch second, also from low T to high T. This code separates the two branches, and uses the volume variable to accurately calculate the magnetization in emu/cc, then plots and saves the plot figure. This was used to quickly display M vs. T data.

```
import pandas as pd
import numpy as np
import matplotlib.pyplot as plt

# Define the base part of the Excel file name
base_file_name =
↪  'FAL001_OOP_10052023_MvsT_10-310K_ZFC_FC_100oE_RSO'
excel_file_name = f'{base_file_name}.xlsx'

# Load the Excel file into a Pandas DataFrame
df = pd.read_excel(excel_file_name)
```

```
11
12 # Extract the desired columns and rows
13 start_row = 31
14 end_row_zfc = 92
15 end_row_fc = 153
16
17 temperature_k_zfc = df.iloc[start_row-1:end_row_zfc-1,
   ↪ 3].to_numpy()  # Column D
18 long_moment_emu_zfc = df.iloc[start_row-1:end_row_zfc-1,
   ↪ 4].to_numpy()  # Column E
19
20 temperature_k_fc = df.iloc[end_row_zfc-1:end_row_fc, 3].to_numpy()
   ↪ # Column D
21 long_moment_emu_fc = df.iloc[end_row_zfc-1:end_row_fc,
   ↪ 4].to_numpy()  # Column E
22
23 # Define the volume variable
24 volume = 5.57865E-8
25
26 # Perform element-wise division to create the 'magnetization'
   ↪ array
27 magnetization_zfc = long_moment_emu_zfc / volume
28 magnetization_fc = long_moment_emu_fc / volume
29
30 #2D Plot Magnetization vs Temperature
31 # Create the plot
32 plt.plot(temperature_k_zfc, magnetization_zfc, label='ZFC',
   ↪ marker='o', color='blue')
```

```
plt.plot(temperature_k_fc, magnetization_fc, label='FC',
    marker='o', color='red')

# Add labels and title
plt.xlabel('Temperature (K)')
plt.ylabel('Magnetization (emu/cc)')
plt.title('ZFC 100Oe FC')
plt.legend(loc='upper left')

#Save plot as png
plt.savefig(f'{base_file_name}.png', format='png')

#Show plot
plt.show()
```

B.6. MvsT_allfiles.py

This code performs the same actions as the previous python file MvsT.py, except it does it for every ZFC/FC measurement done on the sample chosen. This requires the SQUID sequence to do ZFC/FC M vs. T measurements for 100 Oe, 200 Oe, 400 Oe, 800 Oe and 1600 Oe FC values, and iterates through each file. The python code requires the user to convert the .dat file into an excel worksheet, then to identify which rows the ZFC and FC measurements are done at. The volume variable is used to calculate magnetization in emu/cc. After the calculations, the ZFC and FC branches are saved as a text file so that further analysis of M vs. T data can be done. The user has the option to save a figure for each FC value as well.

```
import pandas as pd
import numpy as np
import matplotlib.pyplot as plt
```

```
4
5  # Define the base part of the Excel file name
6  base_file_name = 'FAL001_OOP_10052023_MvsT_10-310K_ZFC_FC_'
7
8  # Define the interval for iterating temperatures
9  field_interval = 100
10
11 #set style for plots
12 plt.style.use('seaborn')
13
14 # Loop through fields from 1000e to 16000e in intervals of 1000e
15 for i in range(5):
16     field = 100 * 2 ** i  # Calculate the field value based on the
       ↪ exponent
17     # Construct the complete file name by concatenating the base
       ↪ name and temperature
18     excel_file_name = f'{base_file_name}{field}oE_RSO.xlsx'
19
20     # Load the Excel file into a Pandas DataFrame
21     df = pd.read_excel(excel_file_name)
22
23     # Extract the desired columns and rows
24     start_row = 31
25     end_row_zfc = 92
26     end_row_fc = 153
27
28     temperature_k_zfc = df.iloc[start_row-1:end_row_zfc-1,
       ↪ 3].to_numpy()  # Column D
```

```
29      long_moment_emu_zfc = df.iloc[start_row-1:end_row_zfc-1,
        ↪  4].to_numpy()  # Column E
30
31      temperature_k_fc = df.iloc[end_row_zfc-1:end_row_fc,
        ↪  3].to_numpy()  # Column D
32      long_moment_emu_fc = df.iloc[end_row_zfc-1:end_row_fc,
        ↪  4].to_numpy()  # Column E
33
34      # Define the volume variable
35      volume = 5.57865E-8
36
37      # Perform element-wise division to create the 'magnetization'
        ↪  array
38      magnetization_zfc = long_moment_emu_zfc / volume
39      magnetization_fc = long_moment_emu_fc / volume
40
41      #Perform subtraction of FC - ZFC
42      magnetetization_fc_minus_zfc = magnetization_fc -
        ↪  magnetization_zfc
43
44      # Create a 3D text file with temperature, long_moment_emu, and
        ↪  magnetization columns
45      text_file_name = f'{base_file_name}{field}oE_RSO_ZFC.txt'
46      data = np.column_stack((temperature_k_zfc,
        ↪  long_moment_emu_zfc, magnetization_zfc))
47      np.savetxt(text_file_name, data, header='Temperature (K) Long
        ↪  Moment (emu) Magnetization', delimiter='\t', comments='')
48
```

```
    text_file_name = f'{base_file_name}{field}oE_RSO_FC.txt'
    data = np.column_stack((temperature_k_fc, long_moment_emu_fc,
    ↪  magnetization_fc))
    np.savetxt(text_file_name, data, header='Temperature (K) Long
    ↪  Moment (emu) Magnetization', delimiter='\t', comments='')

    # Create a new figure for each plot
    plt.figure()

    #2D Plot Magnetization vs Field
    plt.plot(temperature_k_zfc, magnetization_zfc, label='ZFC',
    ↪  marker='o', color='blue')
    plt.plot(temperature_k_fc, magnetization_fc, label='FC',
    ↪  marker='o', color='red')

    # Add labels and title
    plt.xlabel('Temperature (K)')
    plt.ylabel('Magnetization (emu/cc)')
    plt.title(f'ZFC {field}Oe FC')
    plt.legend(loc='upper left')

    #Save plot as png
    plt.savefig(f'{base_file_name}{field}oE_RSO.png',
    ↪  format='png')
```

B.7. MvsT_FCminusZFC.py

This code performs the same functions as the previous python code MvsT_allfiles.py, except it calculates the difference of the FC and ZFC curves

to plot and save FC minus ZFC data. The user has the option to save a figure of the plot, but the text file that is outputted contains temperature and FC minus ZFC data to further analyze in OriginLab or any other software. Like in previous codes, the user must specify the volume of the sample, as well as the rows for the ZFC and FC measurement branches.

```
import pandas as pd
import numpy as np
import matplotlib.pyplot as plt

# Define the base part of the Excel file name
base_file_name = 'FAL001_OOP_10052023_MvsT_10-310K_ZFC_FC_'

# Define the interval for iterating temperatures
field_interval = 100

#create list for colors
colors = ['blue', 'red', 'green', 'purple', 'orange']

#set style for plots
plt.style.use('seaborn')

# Loop through fields from 1000e to 16000e in intervals of 1000e
for i in range(5):
    field = 100 * 2 ** i  # Calculate the field value based on the
    ↪ exponent
    color = colors[i]  # Get the color for this iteration

```

```
    # Construct the complete file name by concatenating the base
    ↪ name and temperature
    excel_file_name = f'{base_file_name}{field}oE_RSO.xlsx'

    # Load the Excel file into a Pandas DataFrame
    df = pd.read_excel(excel_file_name)

    # Extract the desired columns and rows
    start_row = 31
    end_row_zfc = 92
    end_row_fc = 153

    temperature_k_zfc = df.iloc[start_row-1:end_row_zfc-1,
    ↪ 3].to_numpy()  # Column D
    long_moment_emu_zfc = df.iloc[start_row-1:end_row_zfc-1,
    ↪ 4].to_numpy()  # Column E

    temperature_k_fc = df.iloc[end_row_zfc-1:end_row_fc,
    ↪ 3].to_numpy()  # Column D
    long_moment_emu_fc = df.iloc[end_row_zfc-1:end_row_fc,
    ↪ 4].to_numpy()  # Column E

    # Define the volume variable
    volume = 5.57865E-8

    # Perform element-wise division to create the 'magnetization'
    ↪ array
    magnetization_zfc = long_moment_emu_zfc / volume
```

```
    magnetization_fc = long_moment_emu_fc / volume

    #Perform subtraction of FC - ZFC
    magnetetization_fc_minus_zfc = magnetization_fc -
    ↪ magnetization_zfc

    # Create a 2D text file with temperature and magnetization
    ↪ columns
    text_file_name =
    ↪ f'{base_file_name}{field}oE_RSO_FCminusZFC.txt'
    data = np.column_stack((temperature_k_fc, magnetization_fc))
    np.savetxt(text_file_name, data, header='Temperature (K)
    ↪ Magnetization', delimiter='\t', comments='')

    # 2D Plot FC - ZFC Magnetization vs Temperature
    plt.plot(temperature_k_zfc, magnetetization_fc_minus_zfc,
    ↪ label=f'{field}Oe', marker='o', color=color)

    # Add labels and title
    plt.xlabel('Temperature (K)')
    plt.ylabel('FC - ZFC (emu/cc)')
    plt.title('FC - ZFC')
    plt.legend(loc='lower left')

#Save plot as png
plt.savefig(f'{base_file_name}{field}oE_RSO_FCminusZFC.png',
↪ format='png')
plt.show()
```